

Multi-wavelength Studies of  
Active Galactic Nuclei: The Link between  
Black Hole Accretion and Galaxy Evolution

INAUGURAL-DISSERTATION

zur

Erlangung des Doktorgrades  
der Mathematisch-Naturwissenschaftlichen Fakultät  
der Universität zu Köln



vorgelegt von

**Mariangela Vitale**  
aus Taranto, Italien

Köln 2014

Berichterstatter:

Prof. Dr. Andreas Eckart

Prof. Dr. J. Anton Zensus

Tag der mündlichen Prüfung: 9 April 2014

To Tina and Giorgio



## Zusammenfassung

Die Entdeckung, daß die Eigenschaften von Schwarzen Löchern mit denen der sie beherbergenden Galaxien (sogenannte Host-Galaxien) korrelieren, führte zur Hypothese einer gemeinsamen Evolution beider. Die Koevolution des schwarzen Loches mit der Host-Galaxie kann durch Akkretion des Schwarzen Loches und durch den Aufbau stellarer Maße erklärt werden. Beide Mechanismen werden durch das selbe Gas vorangetrieben. Das Gas wird für beides verfügbar nachdem die Galaxie entstanden ist oder nach Wechselwirkungen mit anderen Galaxien.

Die Schwarzloch-Host Koevolution ist eines der meistdiskutierten Themen der modernen Astrophysik, dennoch wurden noch keine eindeutigen Hinweise dafür beobachtet. Insbesondere scheinen aktive Galaxienkerne (AGN) - die hellen und akkretierenden schwarzen Löcher im Zentrum maßiver Galaxien - einen groSSen Einfluß auf die physikalischen Eigenschaften der sie beherbergenden Galaxien zu haben. Die meisten Galaxien sind entweder aktiv (sie produzieren neue Sterne) und blau sowie spiralförmig, oder paßiv, rot und elliptisch. Galaxien mit Eigenschaften zwischen diesen Extremen haben häufig einen aktiven Galaxienkern in ihrem Zentrum. Es wird angenommen, daß dies in Verbindung zu AGN steht, die Jets und Gasausflüße haben, welche mit dem interstellaren Medium der Galaxien interagieren und so die Bedingungen für die Entstehung von Sternen schaffen oder zerstören.

Eine mehrere Wellenlängen umfassende Studie von AGN und Host Galaxien bei mittleren Rotverschiebungen kann uns dabei helfen den Grad der Koevolution und die Art und Weise, wie das sogenannte AGN feedback die Sternentstehung reguliert, zu untersuchen. Das Feedback würde dann zur morphologischen und farblichen Veränderung der Host Galaxie führen. Um

dieses Ziel zu erreichen habe ich eine große Anzahl normaler Galaxien und Host Galaxien in optischen und Radiowellenlängen untersucht, da optische Spektren die Eigenschaften der Galaxien beinhalten, während die AGN Aktivität im Radiobereich sichtbar ist. Darüberhinaus erlaubt es auch die Untersuchung der Verbindung zwischen optischer und Radioemission und deren möglicher gemeinsamer Ursprung.

Diese Doktorarbeit erforscht die Möglichkeit des Bestehens einer evolutionären Sequenz für Galaxien einer bestimmten Maße. Diese Sequenz würde mit plötzlichen, durch Galaxieninteraktion/-verschmelzung ausgelösten Sternentstehung beginnen, gefolgt durch den Aufbau von stellarer Masse und der Akkretion auf das schwarze Loch. Ist das schwarze Loch im Zentrum der Galaxie einmal aktiv, könnte es einmalig oder mehrmalig ein AGN feedback induzieren, das letztendlich den Sternentstehungsprozess in der Host Galaxie beendet. Von diesem Zeitpunkt an entwickelt sich die Galaxie passiv. Die aufeinander folgenden Stadien der Galaxienevolution werden durch optische Emissionslinien definierte Spektralklassen repräsentiert; die Emissionslinien basieren auf niederenergetischen Ionisierungen des Gases. Die Klassen sind: im Sternentstehungsprozess, gemischt (Galaxien mit Beiträgen zu den Emissionslinien sowohl durch Sternentstehung als auch durch AGN Aktivität), Seyfert und LINER Galaxien.

## Abstract

The discovery of general correlations between black hole and properties of the host galaxy has led to the hypothesis of a co-evolution between the two. The black hole-host co-evolution might be explained by black hole accretion and stellar mass build-up of the galaxy being fueled by the same gas. Gas is made available once a galaxy is created, or is gained in successive interactions with neighboring galaxies.

The black hole-host co-evolution is one of the most debated topics of modern extragalactic astrophysics. However, strong observational evidence of it is still missing. Active Galactic Nuclei (AGN) - the bright, accreting black holes at the center of massive galaxies - can play an important role in shaping the physical properties of the galaxies they occupy. Most of galaxies are found to be either active (they form new stars) and blue spirals, or passive and red ellipticals. Galaxies having intermediate properties are often found to harbor an AGN at their centers. This fact has been related to some AGN showing jets and gas outflows, which might interact with the interstellar medium of the galaxies, creating or destroying the conditions for star formation.

A combined multi-wavelength study of AGN and hosting galaxies at intermediate redshifts can help us probing the degree of co-evolution, and the way the so-called AGN feedback may regulate star formation in galaxies. Feedback might lead to the morphological and color transformation of the host. To observe the transformation, I have studied large samples of normal galaxies and AGN hosts in the optical and radio domains. This approach is particularly useful, since optical spectral information can trace host galaxy properties, while AGN activity is visible in the radio. Moreover, this study

allows investigating the connection between optical and radio emission from galaxies, and their possible common origin.

This PhD work explores the chance of an evolutionary sequence for galaxies of a given mass. The sequence would start with merger/interaction triggered bursts of star formation, followed by stellar mass build-up and accretion onto black hole. Once the black hole at the center of the galaxy is active, it might induce once-in-a-time or recurrent AGN feedback, eventually stopping the star-formation process in the hosting galaxy. From this point on, galaxies evolve passively. The stages of galaxy evolution can be represented by spectral classes as defined by optical emission-line diagnostic diagrams. The latter are based on the strength of low-ionization optical lines. The classes are: star-forming, composites (galaxies with mixed contribution to line emission, coming from both star formation and AGN activity), Seyfert, and LINER galaxies.

# Contents

<b>List of Figures</b>	<b>xiii</b>
<b>List of Tables</b>	<b>xv</b>
<b>Glossary</b>	<b>xvii</b>
<b>1 Introduction</b>	<b>1</b>
1.1 Galaxies . . . . .	2
1.2 Active Galactic Nuclei and Active Galaxies . . . . .	6
1.3 Line emission in galaxies and AGN . . . . .	11
1.4 Current understanding of galaxy evolution . . . . .	15
1.4.1 Galaxy bimodality . . . . .	16
<b>2 Thesis aims</b>	<b>21</b>
2.1 Open questions . . . . .	21
2.2 Aims and Methods . . . . .	24
<b>3 Data</b>	<b>27</b>
3.1 COSMOS and zCOSMOS surveys . . . . .	27
3.1.1 Analyzed galaxy sample . . . . .	28
3.1.2 Spectral analysis . . . . .	30
3.2 SDSS . . . . .	32
3.3 FIRST . . . . .	34
3.4 Cross-matched SDSS-FIRST sample . . . . .	34
3.4.1 Selection of SDSS galaxies from the DR7 . . . . .	35
3.4.2 Optical-radio cross-matching . . . . .	37
3.4.3 Completeness of the sample . . . . .	38

## CONTENTS

---

3.5	Effelsberg survey . . . . .	38
3.5.1	Observations . . . . .	40
3.5.2	Selection and completeness of the Effelsberg sample . . . . .	42
3.6	Aperture effect . . . . .	42
<b>4</b>	<b>Stellar mass-AGN relation in intermediate redshift galaxies</b> . . . . .	<b>45</b>
4.1	Introduction . . . . .	45
4.2	Emission-line diagnostic diagrams . . . . .	48
4.2.1	Low-redshift diagnostic diagrams . . . . .	48
4.2.2	High-redshift diagnostic diagram . . . . .	50
4.2.3	Mass-Excitation diagnostic diagram . . . . .	52
4.3	Mass evolution . . . . .	54
4.4	Quenching of the star formation . . . . .	55
4.4.1	AGN identification . . . . .	56
4.5	Conclusions . . . . .	57
<b>5</b>	<b>Radio emitters and their optical counterparts</b> . . . . .	<b>59</b>
5.1	Introduction . . . . .	59
5.2	Analysis . . . . .	61
5.2.1	Diagnostics of the SDSS and the cross-matched samples . . . . .	61
5.2.2	Trend with $L_{20\text{cm}}/L_{\text{H}\alpha}$ . . . . .	64
5.2.3	Trend with redshift . . . . .	70
5.2.4	The WHAN diagram . . . . .	70
5.2.5	Comparison with models . . . . .	77
5.3	Discussion . . . . .	79
5.3.1	Classical diagnostic diagrams . . . . .	79
5.3.1.1	General trend of the full optical and optical-radio samples . . . . .	79
5.3.1.2	Explaining the trend with $L_{20\text{cm}}/L_{\text{H}\alpha}$ . . . . .	79
5.3.1.3	Explaining the trend with redshift . . . . .	82
5.3.2	Recent diagnostics . . . . .	82
5.3.3	Photoionization and shock models for the $[\text{SII}]/\text{H}\alpha$ vs. $[\text{NII}]/\text{H}\alpha$ and $[\text{OI}]/\text{H}\alpha$ vs. $[\text{NII}]/\text{H}\alpha$ diagrams . . . . .	83
5.4	Conclusions . . . . .	84

<b>6 Galaxy evolution across optical emission-line diagnostic diagrams</b>	<b>87</b>
6.1 Introduction . . . . .	87
6.2 Low-ionization emission-line diagnostic diagrams of the Effelsberg sample	92
6.3 Results . . . . .	93
6.3.1 Radio loudness . . . . .	93
6.3.2 Radio spectra . . . . .	97
6.3.3 Spectral index and spectral curvature . . . . .	97
6.3.4 Black hole mass . . . . .	109
6.3.5 Optical and radio morphologies . . . . .	112
6.4 Discussion . . . . .	116
6.4.1 Optical and radio emission in galaxies . . . . .	116
6.4.2 $M_{BH} - M_{bulge}$ correlation . . . . .	117
6.4.3 An evolutionary sequence in the BPT diagram? . . . . .	118
6.4.4 Evolutionary scenarios . . . . .	120
6.5 Conclusions . . . . .	122
<b>7 Final discussion and conclusions</b>	<b>125</b>
7.1 Advantages of combined multi-wavelength studies . . . . .	125
7.2 Optical and radio emission in intermediate-redshift galaxies . . . . .	126
7.3 AGN feedback . . . . .	128
7.4 A unified galaxy-evolutionary sequence . . . . .	129
7.5 Outlook . . . . .	130
<b>References</b>	<b>133</b>
<b>8 Appendix</b>	<b>145</b>
8.1 Reddening correction . . . . .	145
8.2 Stellar templates and extinction . . . . .	146

## CONTENTS

---

# List of Figures

1.1	Optical image of the starburst galaxy NGC 1313. . . . .	2
1.2	Hubble fork composed of optical SDSS images. . . . .	3
1.3	SED of the starburst galaxy NGC 7714. . . . .	5
1.4	Multicolor image of Centaurus A. . . . .	8
1.5	Artist's view of an Active Galactic Nucleus. . . . .	9
1.6	Example of optical emission-line diagnostic diagram. . . . .	12
1.7	Emission-line galaxy classes. . . . .	14
1.8	Galaxy color bimodality. . . . .	16
1.9	Color-stellar mass relation for early-type galaxies. . . . .	19
2.1	Cygnus A active galaxy. . . . .	22
3.1	zCOSMOS 20k sample. . . . .	29
3.2	Examples of stellar continuum subtraction. . . . .	31
3.3	Example of SDSS galaxy spectrum. . . . .	33
3.4	Radio galaxies observed with VLA. . . . .	35
3.5	Effelsberg 100m radio telescope. . . . .	39
3.6	Receivers at the secondary focus of the Effelsberg telescope. . . . .	40
3.7	Cross-scans observing mode at Effelsberg. . . . .	41
4.1	Emission-line diagnostic diagrams of SDSS galaxies. . . . .	46
4.2	Classical low-redshift (or BPT) diagnostic diagram of zCOSMOS galaxies. . . . .	49
4.3	High-redshift or OII-based diagnostic diagram of zCOSMOS galaxies. . . . .	51
4.4	MEx diagnostic diagram. . . . .	53

## LIST OF FIGURES

---

5.1	Radio emitters classified according to optical emission-line diagnostic diagrams. . . . .	62
5.2	Luminosity trend in diagnostic diagrams. . . . .	65
5.3	Redshift trend in diagnostic diagrams. . . . .	68
5.4	Histograms of the luminosity and redshift distributions. . . . .	71
5.5	WHAN diagnostic diagrams. . . . .	72
5.6	WHAN diagnostic diagrams: AGN distribution. . . . .	74
5.7	Data comparison with models. . . . .	76
5.8	Histograms of radio luminosity and luminosity of H $\alpha$ line. . . . .	80
6.1	Effelsberg sample classified according to emission-line diagnostic diagrams. . . . .	91
6.2	Radio-loudness of the Effelsberg sample. . . . .	93
6.3	Radio spectra. . . . .	96
6.4	Spectral index distribution per galaxy spectral class. . . . .	98
6.5	Cumulative histograms of spectral indexes and spectral curvatures. . . . .	99
6.6	Spectral index distribution represented in the diagnostic diagram. . . . .	100
6.7	Radio quiet and radio loud galaxies. . . . .	101
6.8	Spectral curvature distribution represented in the diagnostic diagram. . . . .	103
6.9	Spectral indexes compared with spectral curvature. . . . .	104
6.10	Additional emission-line diagnostic diagrams. . . . .	109
6.11	Black hole masses as a function of spectral classes. . . . .	110
6.12	Black hole mass-radio loudness plane. . . . .	111
6.13	Optical SDSS images of the star-forming galaxies. . . . .	112
6.14	Optical SDSS images of the composite galaxies. . . . .	113
6.15	Optical SDSS images of some Seyfert galaxies. . . . .	114
6.16	Optical SDSS images of some LINER galaxies. . . . .	115
6.17	Stellar-black hole mass relation. . . . .	117
6.18	Sketch of galaxy evolution in the emission-line diagnostic diagram. . . . .	118
7.1	Galaxy stellar mass distribution of the complete optical-radio sample. . . . .	127
7.2	Sketch on galaxy evolution. . . . .	130

# List of Tables

3.1	Datasets summary. . . . .	27
3.2	Line EW statistics on the SDSS DR7. . . . .	37
5.1	Statistics on SDSS DR7 and optical-radio samples . . . . .	63
5.2	Statistics on the $L_{20\text{cm}}/L_{\text{H}\alpha}$ bins. . . . .	67
5.3	Statistics on the redshift bins. . . . .	69
6.1	Statistics on the radio loudness. . . . .	93
6.2	List of sources observed with the Effelsberg telescope at 10.45 and 4.85 GHz. . . . .	106
8.1	Information on the stacked galaxies of the zCOSMOS mass-redshift bins.	147

## GLOSSARY

---

# Glossary

**ADAF** Advection-Dominated Accretion Flows; flows which are characterized by very low radiative efficiency. They might happen during the last stages of gas accretion in massive and passive galaxies.

**ADIOS** Adiabatic Inflow-Outflow Solutions; outflows at the galaxy polar region due to energy liberated by the accretion onto the black hole.

**AGB** Asymptotic-Giant-Branch; sequence of stellar evolution identified in the H-R diagram. Massive stars reach the AGB while their most outer layers expand. AGB stars show red colors and luminosities thousands of times the solar one.

**AGN** Active Galactic Nucleus; accreting and bright black hole located at the center of massive galaxies

**BPT** Baldwin-Phillipps-Terlevich; it refers to the first and still most used optical emission-line diagnostic diagram. The diagram is used to classified galaxies in star-forming galaxies, Seyferts, LINERs and composites, basing on the relative strength of their emission lines.

**ETG** Early-Type Galaxies; elliptical and lenticular galaxies.

**FR I** Fanaroff-Riley Class I; radio sources which have their low brightness re-

gions further from the nucleus than their high brightness regions.

**FR II** Fanaroff-Riley Class II; luminous radio sources with hotspots in their lobes at great distances from the centre.

**IMF** Initial Mass Function; empirical function that describes the distribution of initial masses for a population of stars.

**ISM** InterStellar Medium; matter that exists in the space between the star systems in a galaxy.

**LINERs** Low Ionization Narrow Emission-Line Regions; class of extragalactic sources mostly addressed as AGN. They might be partly excited by shocks.

**LLF** Local Luminosity Function; local space density of sources as a function of luminosity.

**LTG** Late-Type Galaxies; spiral galaxies.

**QSO** Quasi Stellar Object; powerful AGN, mostly found at high redshifts. Due to the extremely bright nucleus, the optical spectrum of the galaxy is stellar-like.

**SED** Spectral Energy Distribution; brightness or flux density versus frequency or wavelength of light. It is used to characterize astronomical sources.

**Seyfert I** Type I Seyferts galaxies; they are very bright sources of optical-UV light and X-rays. They have two sets of emission lines on their spectra: narrow lines with widths (measured in velocity units) of several hundred km/s, and broad lines with widths up to  $10^4$  km/s.

## GLOSSARY

---

- Seyfert II** Type II Seyfert galaxies; they appear bright when viewed at infrared wavelengths. Their spectra contain narrow lines associated with forbidden transitions. Spectroscopy of polarized light component reveals obscured type I regions.
- SFGs** Star-Forming Galaxies; class of galaxies that are actively forming stars and are therefore rather blue and luminous at optical-UV wavelengths. They occupy a well-defined branch in the optical emission-line diagnostic diagrams.
- SMBH** Super Massive Black Hole; black hole whose mass exceeds  $10^6 M_{\odot}$ .
- SN** Super Nova; massive star in the last stage of stellar evolution. It explodes releasing metals in the interstellar medium, and provoking shocks in the latter. The explosion is source of synchrotron radiation.

# 1

## Introduction

Astronomy is one of the oldest and still most fascinating among natural sciences. Originally meant as the study of positions and motions of celestial objects, and based on naked-eye observations, astronomy has then become a brand new science, called astrophysics. Astrophysics began when the first spectra of celestial objects were taken, as this was established to be an accurate method to investigate chemical composition and physical properties of celestial sources.

Galaxies are among the most studied objects. Galaxy emission is examined across the entire electromagnetic spectrum to seek for information on properties such as mass, luminosity, gas density, morphology, temperature, and chemical composition. Since the first galaxies were observed with rudimentary telescopes, much about these complex astronomical objects has been discovered. However, galaxy formation, evolution, and properties, still need to be investigated and fully understood. Our knowledge of galaxies has been increasing in the last decades thanks to the development of modern and more sensitive observing instruments, which allow deep sky investigations. Data have been collected, analyzed, and interpreted, allowing us to add pieces to the big puzzle of the story of galaxies. The estimated number of galaxies in our universe is extremely high, about  $10^{11}$ . A galaxy contains an average amount of  $10^{11}$  stars and, in most cases, it hosts a super-massive black hole in its center. When studied in detail, each galaxy appears to have a unique set of features. However, an extensive study of each object is hardly possible. A good way to study global galaxy properties is to divide galaxies into sub-classes which have similar physical properties.

## 1. INTRODUCTION

---

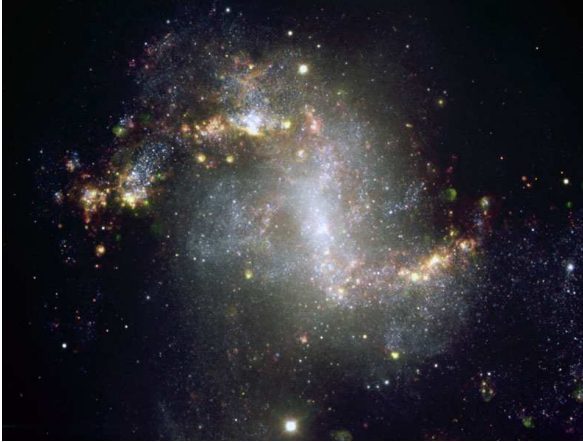


**Figure 1.1:** Optical image of the starburst galaxy NGC 1313. Bright regions in the spiral arms correspond to sites of intense star-formation. Credit: Henri Boffin (ESO), FORS1, 8.2-meter VLT, ESO.

### 1.1 Galaxies

Galaxies contain mainly stars, gas and dust. Galaxies can be found isolated, or can be gravitationally bound in groups (a few galaxies) or clusters (hundreds to thousands of galaxies). These conditions determine the so-called *environment*, which has been proven to have an influence on galaxy properties as mass, morphology, and color. The influence of environment on galaxy morphology was first noted by Edwin Hubble and Milton Humason in 1931 (see 1, for a review). In groups and clusters, galaxy interactions like mergers, fly-by, or gas stripping, are more frequent and can lead to exchange of gas and dust. Fig. 1.1 shows a spectacular *starburst* galaxy, a luminous blue galaxy containing a large amount of ionized gas, where the star formation rate (SFR, the stellar mass produced per year in the star-formation process) is particularly high (more than  $100 M_{\odot} \text{ yr}^{-1}$ ). A starburst is therefore a galaxy that is “very active”, in the sense that it undergoes large burst(s) of star-formation. This is probably due to the above-mentioned galaxy-galaxy interactions, which have brought new gas that becomes available for fueling star-formation.

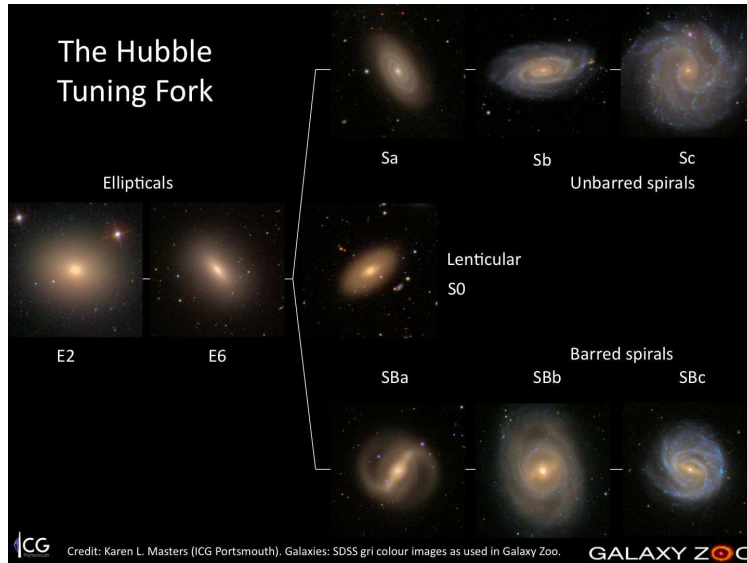


**Figure 1.2:** Hubble fork composed of optical Sloan Digital Sky Survey (SDSS) images. Galaxies come in two main flavors: Ellipticals (E) and Spirals (S). Spiral galaxies can be divided in barred (B) and unbarred, depending on the presence of an elongated narrow structure in their center (called bar). Numbers 0-7 represent the increasing ellipticity of the galaxy. The ellipticity is the ratio between major and minor axis. Letters a-c indicate how tight around the bulge the spiral arms are (“a” meaning loose and “c” very tight). Lenticular galaxies (S0) have intermediate properties between E and S.

## 1. INTRODUCTION

---

Galaxies can be classified and studied according to different physical properties, like mass, size, morphology, color, age of the stellar populations, nuclear activity. According to the classification proposed by Hubble in the 30's and still in use nowadays<sup>1</sup> (Fig. 1.2), galaxies can be classified as spirals (also called spiral galaxies or late-type galaxies) and ellipticals (elliptical galaxies or early-type galaxies). Lenticular morphology is intermediate between ellipticals and spirals. Objects that cannot be classified as one of these three kinds are regarded as irregular galaxies. Galaxies with spiral morphology usually contain large amounts of gas in their arms. Gas is fundamental for the formation of new stars. Spiral galaxies have blue colors, due to optical-ultraviolet emission coming from the newly formed, hot, and bright stars. On the contrary, elliptical galaxies contain less gas and mostly show older stellar populations. The color of elliptical galaxies is typically redder than the color of late-type galaxies, due to the contribution of old stars to the global emission. Ellipticals do not show arms in their morphology, whereas the bulge (the central region of the galaxy, where most of the stars are located) is prominent. Most galaxies can be designated unambiguously to a certain morphological class. Only a few galaxies display intermediate properties, e.g. interacting or irregular galaxies. Spirals are among the largest galaxies in the sky, with disk diameters of 5 to 100 kpc<sup>2</sup>, and a mass range of  $10^9 - 10^{12} M_{\odot}$ <sup>3</sup>. Ellipticals can be more massive, with masses up to  $10^{13} M_{\odot}$ , and reach a size of hundreds of kpc in case of giant ellipticals. Irregular galaxies cover a wide range of characteristics, though they are on average smaller (1 – 10 kpc) and less massive than spirals and ellipticals ( $10^8 - 10^{10} M_{\odot}$ ) (2).

The observed local galaxy bimodality (3, 4, 5, 6, 7), i.e. the presence of two prominent galaxy classes, one blue and young, and the other red and old, might indicate that galaxies which are born with comparable global masses undergo a similar color and morphological transformation. Ideally they move along an evolutionary sequence, starting as spirals and ending as elliptical galaxies. In this case, the transition from blue and active to red and passive galaxy type would be very fast, so that only a few objects are “caught” in the act of evolving from one class to the other.

Spectra contain large amount of information and represent one of the best tools for

---

<sup>1</sup>After minor modifications. Also, the Hubble sequence does not represent an evolutionary sequence, as previously stated.

<sup>2</sup>One kpc corresponds to  $10^3$  parsecs, where a parsec is  $\sim 3 \times 10^{16}$  m.

<sup>3</sup>In solar mass units. A solar mass is  $\sim 2 \times 10^{30}$  kg.

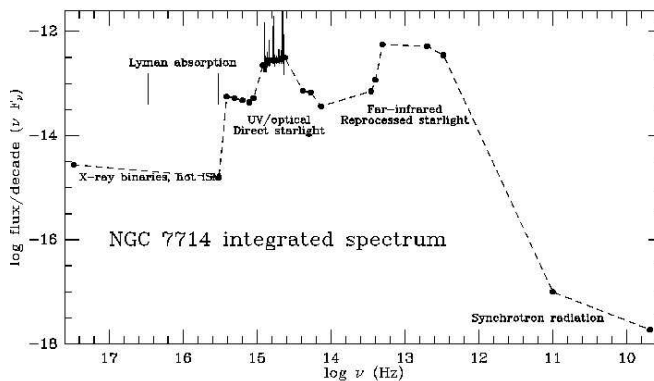


**Figure 1.3:** SED of the starburst galaxy NGC 7714. The plot shows the contribution of each galaxy component to the continuum emission. Stellar components can dominate in UV, visible, or far-IR (through dust emission) depending on the galaxy’s history and structure. X-ray dominance and significant radio emission are produced by active nuclei. Credits: B. Keel, NED, Kennicutt atlas, FUSE data.

the study of galaxies and other celestial objects. On one hand, the analysis of emission and absorption lines provides an insight into chemical composition and physical conditions of the galaxy components - stars, gas, and dust. On the other hand, the shape of the continuum emission at specific wavelengths gives us hints on the contribution of each component to the overall emission. For example, thermal emission in infrared is mainly due to stars and dust, while synchrotron radio emission originates from Super Novae (SNe) explosions, or nuclear activity. Fig. 1.3 shows the spectral energy distribution (SED) of the starburst galaxy NGC 7714. The plot indicates the contribution of X-ray emitting binaries, hot interstellar medium (ISM), stars, dust (reprocessed starlight), SNe and other sources of synchrotron radiation. The latter is produced by high-velocity electrons in a magnetic field. The amplitude of the far-infrared “bump”, or peak, is proportional to both the abundance of dust which is present in the galaxy and the star-formation rate. It is more prominent for starburst galaxies than for normal spirals. Direct starlight and the external regions of the accretion disk produce a bump in the UV-optical, also called “blue bump”.

The engine that causes the gas ionization and line transitions which are detectable in

## 1. INTRODUCTION

---

galaxy spectra can either be star formation, nuclear activity, or a combination of both. For a fixed temperature and density of the gas, the observed strength of a line depends on the total number of ions that are responsible for that line transition. HII regions - rich-in-hydrogen areas where most of the star formation takes place - are mainly located in the outskirts of spiral and irregular galaxies. These contain large amount of interstellar gas and young O and B stars as powerful sources of photoionization. In the central region of galaxies, the origin of emission is often a combination of nuclear activity and stellar ionization. By measuring the relative intensity of emission lines, it is possible to disentangle the nature of the ionizing engine. Stars and nucleus will produce ionizing fields with different strengths, and thus induce different sets of transitions. Knowing the cause of line emission in galaxies, and whether it is dominated by star formation or nuclear activity, will help us understanding the evolution of galaxies.

### 1.2 Active Galactic Nuclei and Active Galaxies

There are few galaxies whose nuclear ionized gas is not associated with hot bright stars. Examples are Seyfert galaxies and quasars. Seyfert galaxies are very luminous active galaxies, and distant and bright sources of electromagnetic radiation, whose spectra reveal strong, high-ionisation emission lines. Quasars (also called quasi-stellar objects) are extremely luminous and were first identified as being high redshift sources of electromagnetic energy, including radio waves and visible light, that were point-like, similar to stars. Unlike quasars, Seyfert host galaxies are clearly detectable. These two kinds of galaxy nuclei have luminosities of the order of  $10^{12}L_{\odot}$ <sup>1</sup>, far too much for the energy source to be of stellar origin (the most massive stars have luminosities of the order of  $10^5L_{\odot}$ ). For a spherically symmetric object in hydrostatic equilibrium, the Eddington condition for the minimum radiation pressure to contrast gravitational force must be satisfied:

$$L \leq L_E = \frac{4\pi Gcm_H M}{\sigma_T} = 1.26 \times 10^{38} \frac{M}{M_{\odot}}$$

where  $G$  is the gravitational constant equal to  $6.67384 \times 10^{-11}m^3kg^{-1}s^{-2}$ ,  $c$  the light speed,  $m_H$  the proton mass,  $M$  the mass of the object and  $\sigma_T$  the Thomson cross-

---

<sup>1</sup>In solar luminosity units. The luminosity of the Sun is  $\sim 4 \times 10^{33}$  erg  $s^{-1}$ .

section<sup>1</sup>. The equation can also be written in the form:

$$\frac{L}{L_{\odot}} \leq \frac{L_E}{L_{\odot}} = 3.22 \times 10^4 \frac{M}{M_{\odot}}$$

from which one can infer that a source of  $L = 10^{12}L_{\odot}$  in hydrostatic equilibrium must have  $M \geq 3 \times 10^7 M_{\odot}$ , which is the typical mass of a black hole. Furthermore, fast continuum variations observed in Active Galactic Nuclei (AGN), or accreting black holes, suggest that the energy source must have a size in the order of 1 light-week or -day (0.005 – 0.001 pc). Therefore, the best candidate as energetic source in AGN is the accretion disk around a super-massive black hole, namely the release of gravitational (or rest-mass) energy of matter converted into radiation due to friction. Super-massive black holes can have masses ranging from  $10^6$  to  $\sim 10^9 M_{\odot}$ . Fig. 1.4 shows one of the most studied AGN. The galaxy orientation is edge-on, which means the observer's line of sight meets the dust lane that surrounds the galaxy, thus we are not looking directly towards the nucleus. The prominent jets, possibly originating in the nuclear region and collimated by a strong magnetic field, propagate in the medium perpendicularly to the galaxy plane. Galaxies hosting AGN can be classified according to their luminosities, the strength of the emission lines, or their physical properties. A common way to identify AGN is to look for them in the X-ray or radio domain. X-ray emission is a very energetic radiation probably produced in a compact region close to the super-massive black hole. Also powerful radio galaxies frequently host an active nucleus at their center. In radio galaxies, synchrotron emission typically arises from the nucleus, and from two large, diametrically opposite lobes that extend up to kiloparsec scales. It is believed that lobes originate from magnetized plasma, collimated into two powerful jets ejected by the accreting black hole. However, observability of jets is highly dependent on the inclination angle of the source. When the AGN is face-on (we look directly at the nucleus, and the galaxy disk is perpendicular to the observer's line of sight), the jets might be aligned with the observer's line of sight. We then measure an intensity that is magnified by relativistic factors, the so-called *doppler boosting*. Moreover, there are AGN that might not show jets for some reasons, e.g. sensitivity limits of the current instruments. Once again, spectral information is essential for a deep understanding of

---

<sup>1</sup>Section of elastic scattering of electromagnetic radiation by a free charged particle, as described by classical electromagnetism.

## 1. INTRODUCTION

---

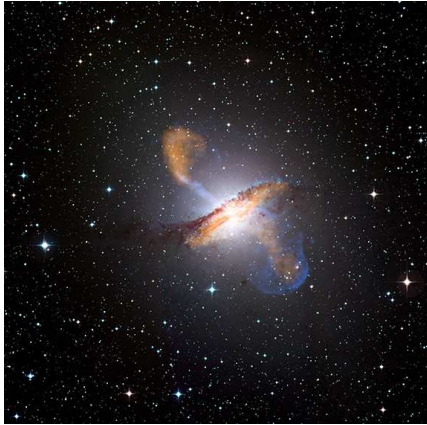


**Figure 1.4:** Multicolor image of Centaurus A, a dusty elliptical galaxy harboring an AGN. In the image, we see the dust ring encircling the giant galaxy, and the fast-moving radio jets ejected from the galaxy centre, signatures of the supermassive black hole at the heart of Centaurus A. Credits: ESO press release 2009-01-28.

AGN properties. All AGNs have a continuous spectrum in the optical region, in addition to their emission lines. Their hosting galaxies have the typical integrated stellar continuum plus absorption-line spectrum<sup>1</sup>. Emission lines observed in AGNs are similar to the emission lines observed in HII regions of normal (without AGN) galaxies, except that AGNs have a higher range of ionization. Highly ionized elements, such as [NeV], [FeVII], and [FeX], are observed in AGN. [SII] $\lambda\lambda 6717,31$ , [OII] $\lambda\lambda 3726,29$ , [NII] $\lambda 6584$ , and [OIII] $\lambda\lambda 4959,5007$  (hereafter [SII], [OII], [NII], and [OIII], respectively), which are a relatively low stage of ionization, are usually stronger in AGN than in star-forming galaxies

There are several excitation mechanisms that give important contributions to galaxy emission, though photoionization is the most likely source of excitation for the emission line gas in AGNs. Dissipative processes in the accretion disc transport matter inwards and angular momentum outwards, while causing the accretion disc to heat up. The

---

<sup>1</sup>In this work we consider AGN to be the host galaxy + active nucleus, more than the accreting black hole only. Definitions are often interchangeable in literature, though I try to use the term “host” while speaking of surrounding galaxy.

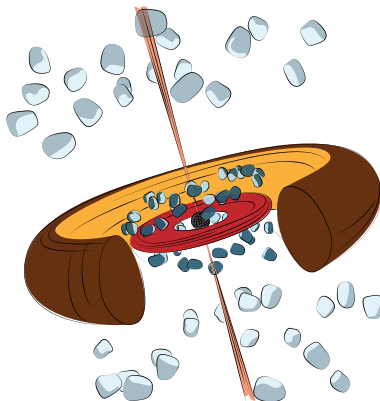


**Figure 1.5:** Artist's view of an Active Galactic Nucleus (AGN). The black core represents the accreting black hole, and the red ring the accretion disk. The jets are colored in salmon. Grey clouds close to the accretion disk represent the Broad Line Region (BLR), while the most outer clouds are the Narrow Line Region (NLR). The dusty torus is represented in brown/yellow. Courtesy of Sebastian Kiehlmann.

radiation from the accretion disc excites cold atomic material close to the black hole and this, in turn, radiates at particular emission line frequencies. Another mechanisms of ionization could be the “auto-ionizing shocks”, e.g. jets in radio galaxies. These heat the local medium sufficiently that it re-radiates in UV and X-ray (8). Often, a combination of these processes is needed to explain the observed emission-line ratios (9).

Unified models of AGN propose that different observational classes of AGN are a single type of physical object observed under different conditions. The currently favored unified model is a “orientation-based unified model”, where the apparent differences amongst AGNs arise because of their different orientations to the observer (10, 11). Fig. 1.5 shows the AGN components according to the picture offered by the unification model. The *Narrow Line Region* (NLR) of an AGN is a region of clouds embedded in ionized and neutral gas generally characterized by strong [NII] and [OIII] emission. In contrast to the more compact (less than 1 pc, or several light days) *Broad Line Region* (BLR), the NLR is in the order of  $10^3$  pc in size and contains relatively low-density

## 1. INTRODUCTION

---

gas, with electron densities  $N_e \sim 10^4 \text{ cm}^{-3}$ . In some cases, the BLR is hidden by the dusty *torus*, which is large enough to obscure the BLR but not the NLR. Seyfert I are galaxies where both the NLR and BLR are observable. Seyfert II are objects where, due to inclination effects, the BLR is not directly visible. The presence of the BLR in Seyfert II can then be verified by complementary studies of the polarized AGN light, since emission from the inner parts is scattered on the material around the torus and reaches the observer from a different angle. Narrow lines have typical widths of up to  $\sim 500 \text{ km s}^{-1}$ . The BLR has  $T \sim 10^4 \text{ K}$ , such that photoionization is the main process responsible for line emission. The lines are much broader compared with the NLR ones, and range between  $\sim 1000$  and  $25000 \text{ km s}^{-1}$ . The broadening of the lines in the BLR, which is located closer to the nucleus, is caused by supersonic bulk motion of the emitting gas. The gas density can be estimated by using the line ratios of forbidden transitions, e.g. [OIII] lines, since these transitions only take place if the density is lower than a critical value. The critical density for an atomic level is defined as the density at which the collisional de-excitation rate balances the radiative transition rate. The critical density depends on the element, and on the specific transition. For example, in case of [O III] the value is  $7 \times 10^5 \text{ cm}^{-3}$  (12).

According to the intensity of their narrow lines, most of the local AGN population can be divided in Seyfert galaxies and Low Ionization Narrow Emission Line Regions (LINERs, 13). At high radio powers, the classification is analogous. However, the population of radio galaxies is completely dominated by low-luminosity, low-excitation objects. These do not show strong emission lines from the nucleus. Seyferts are rather powerful AGN and present a high [OIII]/ $H\beta$  ratio. Their hosting galaxies have lower stellar masses compared to LINERs hosts, and the stellar populations show a wider range of ages and metallicities (14). At radio wavelengths, LINERs show the highest fraction of AGN peculiar morphologies, like jets and lobes.

Galaxies are considered as radio-loud if they have ratios of radio flux at 5 GHz to optical flux in B band greater than ten (15). According to Fanaroff (16), radio-loud galaxies (generally AGN) can be divided into two major classes. In Fanaroff-Riley Class I (FR I) sources, the radio emission peaks near the galaxy nucleus and the emission from the jets fades with distance from the center. In contrast, FR II sources present bright radio lobes, which can reach kpc-scale distances from the nucleus. FR I sources dominate the population of radio emitters at low radio power ( $< 10^{25} \text{ W Hz}^{-1}$  at 1.4 GHz) and

low redshifts, while more powerful radio galaxies (with 178-MHz radio power greater than  $10^{27}$  W Hz<sup>-1</sup>) are almost exclusively FR II systems. These can also be detected at higher redshifts compared to FR I. It is possible to observe the jets interacting with the surrounding medium and forming a bow-shock. This is called “sharp-edge feature”. Such FR II features are present when the central engine releases a large amount of energy, or when the source is young enough for the aging of the radiation not to play a role. In the oldest sources, nowadays more associated to LINERs and FR I, the radiation that originates from the nucleus and propagates through the jets loses power as it interacts with the medium, therefore lobes are not a prominent feature any longer. Here the environment, especially the position of the galaxy in a group or cluster, and the density of the intergalactic medium, play an important role in shaping the galaxy’s morphology.

Radio galaxies can be further classified according to the strength of high-excitation narrow-line emission. The majority of FR I radio galaxies show either no or very weak emission lines. Those are referred to as low-excitation systems (17), and are mostly found in elliptical galaxies with little ongoing star formation (18, 19). If optical spectroscopic information is available, these galaxies are generally classified as weak AGNs or LINERs. Conversely, the most powerful and high-redshift FR II radio galaxies have, in most cases, strong emission lines. They are classified as strong AGNs (20) and have peculiar optical morphologies, e.g. tails, bridges, and shells (21), and bluer colors compared to giant ellipticals. It has also been established that powerful FR IIs show a strong correlation between their radio luminosity and their optical emission-line luminosity (22), suggesting that both optical and radio emission originate from the same physical process.

Observations at various wavelengths have contributed to increase our knowledge of AGN hosts. Every spectral band, from the far IR through the optical-UV, and to the X-ray regime, has provided information that helped understanding these objects.

### 1.3 Line emission in galaxies and AGN

The temperature of the ionized gas in galaxies hosting AGN is of order of  $2 \times 10^4$  K<sup>1</sup>. This indicates that the main source of energy input is by photoionization. Analysis of

---

<sup>1</sup>Value computed for NLRGs and Seyfert 2 galaxies.

## 1. INTRODUCTION

---

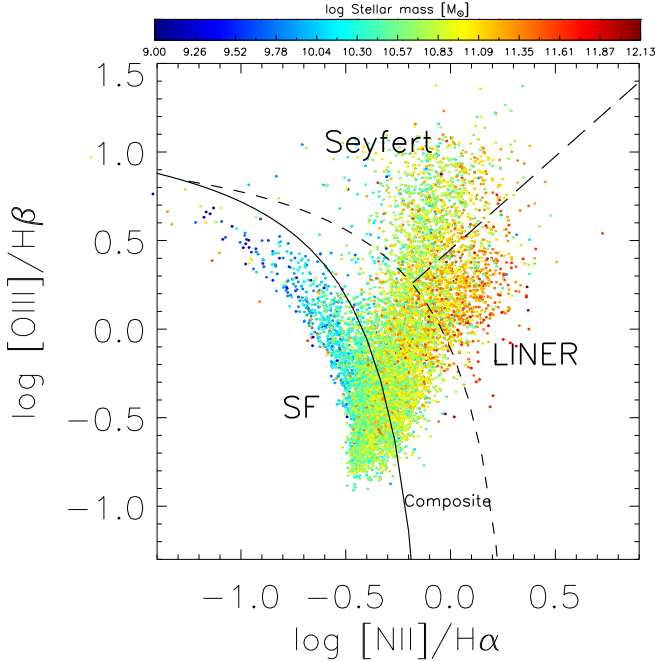


**Figure 1.6:** Example of an optical emission-line diagnostic diagram (4, 23, 24, 25, 26). Data points represent radio emitters for which optical spectral measurements are available. Colors indicate galaxy stellar mass values. “Blue” means low stellar mass, and “red” is high stellar mass. A theoretical demarcation curve (dashed, Kewley et al. 25) separates star-forming galaxies and composites from AGN (Seyferts and LINERs), while an empirical demarcation curve (continuous, Kauffmann et al. 27) separates pure SFGs from composites and AGN. Composite galaxies show a mixed contribution to line emission from both star formation and AGN activity. A further line separates Seyferts from LINERs (long-dashed, Schawinski et al. 28).

### 1.3 Line emission in galaxies and AGN

---

AGN spectra show that the main source of radiation cannot be hot stars. Radiation from such hot stars cannot produce the wide range of ionization observed in AGN, with emission lines of low ionization stages, such as [OI] and [SII], as well as higher stages (e.g. three times ionized species and so on). Thus, the source of the emission must have a much harder spectrum, capable of ionizing one species several times. The energy released from the accretion process that feeds the black hole in the galaxy nucleus might be responsible of photoionizing the emitting gas.

The classification of AGN and star-forming galaxies from their optical spectra is mainly based on the recognition of the main energetic source - nucleus or stars, respectively - responsible for the observed emission. A classification can be achieved by the comparison of ratios of prominent emission lines, like the doubly ionized oxygen, or nitrogen, and the lines of the Balmer series. Balmer lines ( $H\alpha$ ,  $H\beta$ ,  $H\gamma$ ,  $H\delta$ , etc.) are associated with star formation, and are the main line features in the spectra of normal galaxies. In the most commonly used emission-line diagnostic diagram, the [NII]/ $H\alpha$  and [OIII]/ $H\beta$  line ratios are used (23). In such diagram (Fig. 1.6), the star-forming galaxies occupy a sequence from the upper left to the lower center. This sequence is considered to be a consequence of the correlation between metallicity<sup>1</sup> and ionization parameter. Nitrogen enhancement in AGN is thought to originate from secondary CNO nucleosynthesis, where carbon and oxygen are pre-existing, and then distributed by stellar winds from massive stars. This creates a unique scaling relationship with metallicity,  $[N/H] \propto Z^2$ , while other elements scale linearly with metallicity (29).

The ionization parameter indicates the ratio between the ionizing photon flux and the gas density in a cloud, and determines the degree of ionization of a chemical species. The ionization parameter for hydrogen ( $U$ ) at the front of a gas cloud is given by:<sup>2</sup>

$$U = \frac{|\textit{ionizing photon flux}|}{cN_e} = \frac{\int_{\nu_0}^{\infty} L_{\nu} d\nu / h\nu}{4\pi r^2 c N_e}$$

where  $N_e$  is the electron density,  $\nu_0$  is the threshold ionization frequency,  $r$  is the cloud-center distance, and  $c$  is introduced to make  $U$  dimensionless. Typical values for  $U$  in AGN clouds range between 0.1 and 1 (30). Although there is a different ionization parameter for each species, and for different distances from the cloud center,  $U$  gives a

---

<sup>1</sup>The relative percentage of chemical species heavier than helium, usually measured in solar metallicity units.

<sup>2</sup>Source: <http://ned.ipac.caltech.edu/level5/March02/Netzer/Netzer2.html>

## 1. INTRODUCTION

---

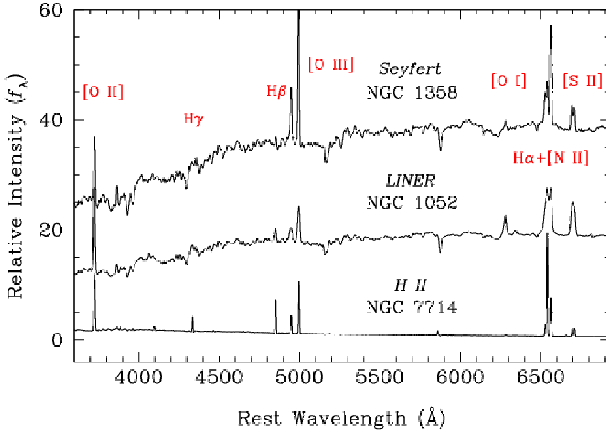


**Figure 1.7:** Emission-line galaxy classes and their optical spectra. Prominent emission lines are identified. Based on Ho, Filippenko & Sargent 1993 and unpublished data.

good approximation of the overall level of ionization. The ionization parameter is also a measure for ionization structure changes, where the thickness of ionization fronts is inversely proportional to  $U$ . A high ionization parameter ( $U \sim 0.1 - 1$ ) corresponds to a sharp transition between successive stages of ionization, and low  $U$  results in thick regions of gradual change in the level of ionization. Low  $U$  indicates several stages of ionization co-existing over large parts of the cloud.

As the metallicity (expressed in Fig. 1.6 by the  $[\text{NII}]/\text{H}\alpha$  ratio) increases, the ionization parameter, expressed by  $[\text{OIII}]/\text{H}\beta$ , decreases at first. The sources on the right-hand side of the star-forming region in the diagnostic diagram represent AGN hosts (Seyferts and LINERs). AGN produce higher  $[\text{NII}]/\text{H}\alpha$  and  $[\text{OIII}]/\text{H}\beta$  than star-forming galaxies, due to their harder ionizing fields (e.g. capable of doubly ionizing more oxygen atoms) and the inefficiency of cooling. The high-energy photons of AGN cause high ionization near the central source, as well as a more extended, partially ionized zone where atoms and ions can be collisionally excited. Collisional excitation gives rise to spectral lines in the spectra of astronomical objects such as H II regions. In these objects, most

atoms are ionised by photons from hot stars, stripping away electrons. The emitted electrons, (called photoelectrons), may collide with atoms or ions within the gas, and excite them. When these excited atoms or ions revert to their ground state, they will emit a photon e form a line. One should keep in mind that line emission-line ratios depend both on the specific element abundances and the strength of the ionizing fields (e.g. the type of stars). High [OIII]/H $\beta$  values require high ionization parameters and are a common feature of metal-poor star-forming galaxies and AGN (31). Fig. 1.7 illustrates the typical optical spectra of AGNs (top and middle spectra), compared with the normal star-forming galaxy NGC 7714 (bottom spectrum). Strong low-ionisation emission lines are very prominent in AGN (Seyferts and LINERs) in contrast to the spectrum of a normal galaxy, where H $\alpha$ , H $\beta$ , and the other lines of the Balmer series are more prominent.

## 1.4 Current understanding of galaxy evolution

Recently, a better overview of galaxy formation and evolution has been developing, with a great contribution coming from large cosmic surveys. Cosmic surveys play an important role in modern astrophysics. They open the door to extensive studies on large statistical samples of galaxies, and catch the light from objects that are not located in the local universe. The fact that all massive galaxies might harbor a black hole at their center has generated new hypothesis on galaxy evolution (32, 33). The central black hole can be either active, if it accretes material from the accretion disk, or inactive. Active black holes might present highly collimated emission of charged particles, the so-called jets, that possibly influence galaxy evolution. Jets can on the one hand be able to clear the gas reservoir of the galaxy, eliminating the fuel to produce new stars, and on the other hand create shock fronts and compress the inter-stellar medium, creating the conditions to form stars. Therefore, studying AGN is crucial to understand whether their presence can affect galaxy properties significantly and/or induce morphological and color evolution.

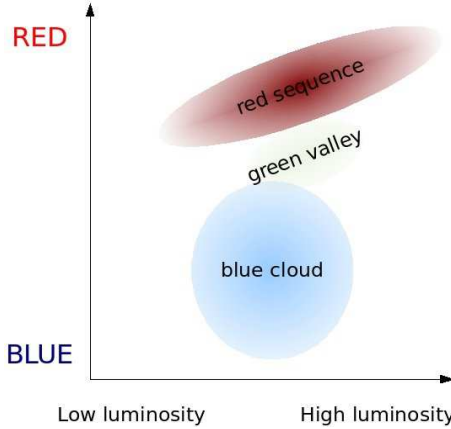


**Figure 1.8:** Representation of the galaxy color bimodality in a color-luminosity plot. Credits: Wikipedia.

### 1.4.1 Galaxy bimodality

The local galaxy's color function, i.e. the distribution of galaxy colors<sup>1</sup>, has been discovered to be a bimodal function (3, 4, 5, 6, 7). The two dominant color sequences are associated with the ellipticals+lenticulars population (*red sequence*) and the spirals+irregulars population (*blue cloud*). Galaxies showing intermediate properties, like early-type red spirals, are considered as composites or transitional objects (*green valley*). Early-type galaxies (ETGs) are mostly found in the red sequence and dominate at the top-end of the local galaxy mass function, which means that they are particularly abundant among massive galaxies. Conversely, late-type galaxies (LTGs) are rare among massive galaxies and occupy the blue cloud preferentially. Fig. 1.8 shows a representation of the galaxy color bimodality in the luminosity-color plane.

The fast suppression of the star formation activity, the so-called *quenching*, is currently thought to initiate passive galaxy evolution and to be largely responsible for the growing abundance of galaxies on the red sequence (34). The star formation quenching could be explained by several mechanisms. The observed decline of the galaxy star

---

<sup>1</sup>Inferred from the band filter.

---

## 1.4 Current understanding of galaxy evolution

---

formation from  $z \sim 1$  to  $z = 0$  can be caused by a gradual and natural *gas exhaustion* (35). Another mechanism that could explain the quenching are *major mergers*<sup>1</sup>. The interaction between a galaxy and its neighbors could indeed produce gravitational torques on the gas, reducing its angular momentum and allowing it to fall it toward the galactic center after an initial starburst phase (36). As a result, fuel is available for accretion, allowing the growth of the central black hole instead of the formation of new stars in the disk. However, the importance of mergers in the build-up of the galaxy bimodality has been criticized, as luminous and massive old galaxies formed via mergers were already common at  $z \sim 1$  (37), and their number density only declines above this value. If merger events were efficient in forming galaxies at  $z < 1$ , we would expect an increasing number of massive objects towards low redshift, which has not been observed.

Similarly, a role for AGN in galaxy evolution has been suggested (38, 39, 40, 41). Black holes are thought to be a basic constituent of most massive systems (42) and they have also been identified in some late-type and dwarf galaxies (43). During the BH accretion, AGNs release a large amount of energy, which could be partially absorbed by the host galaxy and quench the star formation via re-heating of the interstellar gas. Eventually, this transforms blue galaxies into red galaxies (e.g. 44, 45, 46). According to Cattaneo et al. (47), less than 1% of the energy released within a bulge during the BH accretion would be sufficient to heat and/or blow away the entire gas content. Consistent with this framework, Hopkins et al. (48) further developed the scenario described in Sanders (49), where starburst, quasar active phase, BH growth, and elliptical galaxies are connected to each other in a galaxy evolutionary sequence. This sequence starts with mergers, and the gas consumption is coupled with supernova-driven winds and/or AGN-feedback to quench star formation.

The hypothesis of AGN feedback is strengthened by the fact that a large amount of galaxies have been found to go through an active phase. Summed over all Hubble types, roughly half of all galaxies can be considered as active (50), even though some of them show a fairly low activity level. The amount of active galaxies becomes more remarkable for galaxies with a prominent bulge component, rising to 50-70% for Hubble types E-Sb. The percentage of AGNs drops towards later Hubble types (Sc and later), where about 80% of the galaxies host a star-forming nucleus instead. This suggests a

---

<sup>1</sup>Encounters of galaxies of similar mass and size.

## 1. INTRODUCTION

---

clear dependence of nuclear activity on the Hubble type (4, 51). The observed distribution of Hubble types for galaxies hosting active versus inactive nuclei leads to the expectation that the blue and red populations do not only differ in nuclear, but also global properties. In particular, it seems that the observed high fraction of AGNs in the green valley points to a connection between the end of the star formation phase, observed in a change of the galaxy color, and the rise of AGN activity (52, 53). In Fig. 1.9, Schawinski et al. (54) show an example of color-stellar mass relation, and assume  $u - r$  colors<sup>1</sup> as a proxy for the stellar age of galaxies in their Sloan Digital Sky Survey (SDSS) sample divided in spectral classes according to their emission-line ratios. Stellar mass is here considered as a “cosmic clock” and indicates a sort of galaxy evolutionary sequence. On their way to the red sequence, galaxies seem to undergo a phase of significant nuclear activity, indicating that AGN may have a role in galaxy evolution. At the high-mass end of their sample, only quiescent and LINER galaxies are found.

---

<sup>1</sup>Difference between the ultraviolet (u) and red (r) optical filters.

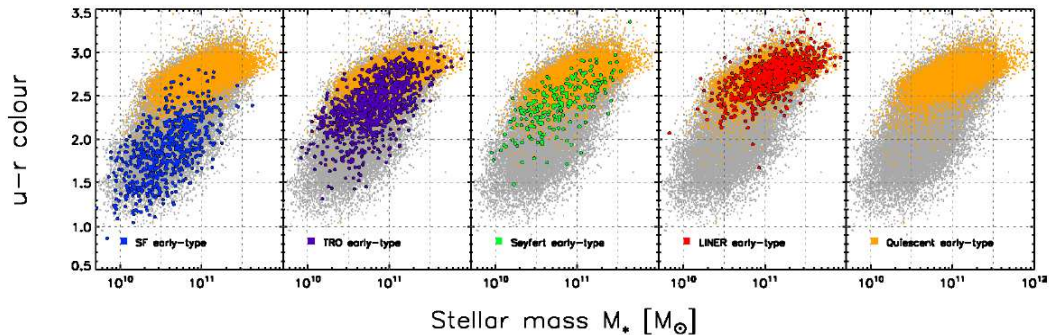


**Figure 1.9:** Color-stellar mass relation for early-type galaxies. Plot from Schawinski et al. (54) illustrating the color-stellar mass relation for a sample of early type galaxies drawn from the SDSS. In each panel, morphological late-type galaxies are gray, quiescent early-types are orange and the various active early-types are blue (star forming), purple (transition region), green (Seyfert), and red (LINER). These spectral classes are based on the classification in Fig. 1.6.

## 1. INTRODUCTION

---

## 2

# Thesis aims

### 2.1 Open questions

The possibility of a general correlation between emission lines and radio luminosities of AGNs has been already explored in the past (55, 56). Radio-loud AGNs are most likely to display optical emission lines in galaxies with low velocity dispersions<sup>1</sup> and radio luminosities greater than  $10^{25}$  W Hz<sup>-1</sup> (57). A similar correlation has been observed between the emission-line luminosity and the ionization state of the gas for a sample of low- $z$  radio galaxies (58). The higher values of the emission-line luminosities have been measured for the more powerful radio sources, as an indication of the presence of a strong ionizing AGN-like field. However, a problem arises since the most powerful radio galaxies are generally detected at higher redshifts than the less powerful radio galaxies. This is due to selection effects, and makes it difficult to establish whether the correlation is between the emission-line luminosity and radio luminosity, or rather between emission-line luminosity and redshift (55). For the same reason, it is also not simple to build a large statistical sample of emission-line radio galaxies placed at intermediate and low redshifts.

The well-known effect of having an increasing number of detected powerful radio AGNs with increasing redshift is not only due to a selection bias, but it is also supported by the downsizing scenario of galaxy evolution (59). Galaxies placed at higher redshifts are more massive than local galaxies, and host massive black holes that accrete gas,

---

<sup>1</sup>Indicated with  $\sigma$ , it is the statistical dispersion of velocities about the mean velocity for a group of object, eg. stars.

## 2. THESIS AIMS

---

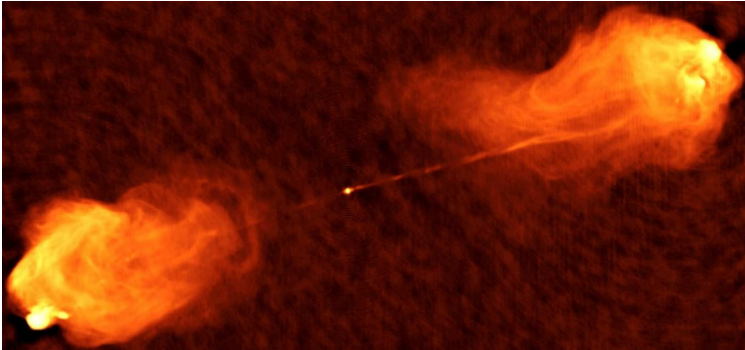


**Figure 2.1:** The powerful radio galaxy Cygnus A shows prominent jets and lobes, originating from the central black hole. Image courtesy of C. Carilli.

producing powerful jets. These galaxies are easily detected in the radio domain, while low-redshift radio galaxies host low-mass black holes, with weak jets that are more difficult to observe. On the other hand, quasars detected in the radio but not in the optical regime might be heavily obscured objects. They experience dust obscuration when observed through the optically thick torus, which surrounds the black hole (unified model by Antonucci, 10), or dust lanes in the hosting galaxy. Proofs of a true correlation between optical and radio galaxy emission, as well as extensive combined studies in these two domains, are still missing.

One of the current scenarios of galaxy evolution includes the possibility of a smooth transition from LTGs, which show blue colors and ongoing star formation, to red and passively evolving ETGs. This transition could be driven by the so-called AGN feedback (47, 60), which is thought to be responsible for star formation quenching. In particular, radio galaxies are excellent candidates for testing this scenario, since they present jets (see Fig. 2.1) that could heat up the interstellar medium, thus preventing cooling and star formation, or push the gas away from the nuclear region. After quenching, a phase of passive evolution starts, and the galaxy color turns redder. Some studies show that there is indeed a correlation between the age of galaxy stellar populations and the AGN activity (61, 62), with the oldest stars inhabiting the AGN-like galaxies. Moreover, AGNs are found to reside almost exclusively in massive galaxies

( $M_* > 10^{10} M_\odot$ ) with structural properties similar to normal early-type systems (63), which are dominated by old stellar populations.

The question of whether the AGN feedback is capable of quenching star formation, or rather triggering it in the vicinity of the black hole and on larger scales, still has to be answered. The standard accretion mode of AGNs, which is associated with quasar activity (64), is related to star formation in the host galaxies (4). This scenario seems to contrast the quenching of the starburst activity due to AGN feedback. Very recent results from studies using integral field spectroscopy techniques (65, 66) or the extremely high spatial resolution of ALMA (67) and other radio facilities (68) show the presence of gas outflows propagating from the center of galaxies. Outflows could be responsible for compressing the medium, or cooling it down, or enhancing the metallicity (important for cooling and star formation).

Star formation and black-hole accretion, both fueled by the same material, might occur with delays with respect to each other (69, 70) and come to an end once the gas is exhausted. A fraction of AGNs discovered in starburst galaxies show powerful radio jets and are therefore radio “loud”. Ivezić et al. (71) have shown that a sample of optically unresolved radio-bright sources from the FIRST radio survey have bluer colors than other SDSS objects. Richards et al. (72) found that the SDSS quasar candidates - which are likely to have a radio counterpart - display blue colors, especially at  $z > 1$ , indicative of ongoing star formation. If this is proven to be right, starburst, AGN, and passive elliptical could be regarded as different but related phases in the evolution of a regular galaxy.

To understand the importance of AGN feedback in the current scenarios of galaxy evolution, a study of AGNs and their host galaxies properties, and the physical mechanisms that trigger line emission or radio activity, is necessary. One of the major goals of modern astrophysics, and topic addressed in this thesis, is the understanding of the interplay between black hole accretion and evolution of the physical properties of the hosting galaxy. In particular, I would like to address the following questions:

- Are optical and radio emission in AGN hosts connected, and originating from the same physical mechanism(s)?
- Does the AGN-feedback have a substantial and formative role in galaxy evolution?

## 2. THESIS AIMS

---

- To what extent are AGN and galaxy properties related?
- Is there a sequence that links the blue color distribution (spirals) to the red color distribution (ellipticals)?
- How can a multi-wavelength approach help us solving these questions?

### 2.2 Aims and Methods

Given the high number of galaxies in the universe, one of the best ways to study these objects is to classify them according to their properties, and use a statistical approach to analyze how galaxies grow and evolve. My research focuses on the study of Active Galactic Nuclei and host galaxy properties in the radio and optical domains. The optical regime is very effective in tracing the host galaxies properties (color, morphology, mass, stellar content), while the radio regime is particularly useful for identifying AGNs. Moreover, observational evidence points towards a tight correlation between emission at optical and radio wavelengths. This indicates a possible common origin of the emission.

The main aim of my PhD project is to bridge the lack of extended multi-wavelength studies of galaxy properties and provide observational evidence to the latest models of galaxy evolution. My research includes my published studies on the correlation of AGN-detection rate with stellar mass of the host galaxies up to  $z \sim 1$  (Chapter 4, see also 62), and investigations on the origin of the optical line emission in radio galaxies (Chapter 5, see also 73, 74). In particular, I study whether AGNs occur more frequently in massive and passive radio-bright hosts, consistently with a scenario where the AGN feedback stops the star formation. Also, the nature of AGNs, as classified in the optical-emission line diagnostic diagrams, is investigated with the goal of identifying the main source of line emission in Seyferts and LINERs. LINERs are mostly regarded as AGNs, although there is growing evidence that some of these objects are actually ionized by fast shocks and old stars, and not by the nucleus. This opens the doors to a new interpretation of the LINER phenomenon as the very last stage of galaxy evolution, starting after the AGN quenching of the star formation.

The multi-wavelength approach, i.e. the study of combined properties as inferred from data taken at different wavelengths, is crucial to unveil the evolution of galaxies over

the cosmic time. For these reasons, I have carried out a research program that makes use of new observations and archive radio data, combined with existing optical data. Subsequently to the submission of a proposal for the use of the Effelsberg 100m radio telescope, I have been granted 50h observing time to conduct a galaxy survey. I have measured continuum intensity and polarization of 150 radio emitters with optical (SDSS) counterpart. The collection of the Effelsberg data aims at probing galaxy evolution in radio emitters that are classified as star-forming, composite, Seyfert and LINER galaxies in the optical emission-line diagnostic diagrams, by looking at their combined optical-radio properties. With this project, I search for a flattening of the radio spectral index along the composite-AGN sequence of the diagnostic diagrams (Chapter 6). Flattening is expected due to the presence of compact nuclei, or jet emission. In particular, I am interested in testing a scenario where the end of the star-forming phase of galaxies represents a turnover point in galaxy evolution, i.e. the start of the quasar phase, which leads to the color and morphological transformation of the hosts (transition from spirals to ellipticals). The analysis of the spectral indexes, combined with the information on the radio morphology (low resolution, from FIRST survey at 20 cm), will help us to investigate the nature of the sources along the composite-AGN branch, their active state, and the chance to spot an evolutionary sequence .

## 2. THESIS AIMS

---

# 3

## Data

For the accomplishment of the thesis aims, I have worked with different optical and radio datasets. This chapter aims at giving a description of the surveys and the specifications of the datasets. Table 3.1 provides a summary of the data I used.

### 3.1 COSMOS and zCOSMOS surveys

The COSMOS survey (75) is a large Hubble Space Telescope (HST) Treasury project that covers  $\sim 2 \text{ deg}^2$  equatorial field with the Advanced Camera for Surveys (ACS). It uses  $I$ -band exposures down to faint magnitudes ( $I_{AB} = 28, 75$ ). The COSMOS field has been the object of extensive multi-wavelength ground- and space-based observations spanning the entire spectrum: X-ray, UV, optical/NIR, mid-infrared, mm/submillimeter, and radio, providing fluxes measured over 30 bands (76, 77, 78, 79, 80, 81, 82, 83, 84).

z range	Ang. resol.	Spectr. resol.	Objects
zCOSMOS			
$0.18 < z < 0.88$	$\sim 1''$	100 km/s	15 715
Cross-matched SDSS-FIRST			
$0.04 \leq z < 0.4$	$\sim 5''$	65 km/s	9 594
Effelsberg			
$0.04 \leq z < 0.4$	$\sim 1'$	65 km/s	150

**Table 3.1:** Datasets summary. Col. 1: Redshift range. Col. 3 and 4: Angular and spectral resolution. Col. 4: Number of objects in the sample.

### 3. DATA

---

The zCOSMOS survey was planned to provide high-quality redshift information to the COSMOS field (79). It benefitted of  $\sim 600$  h of observations at VLT using the VIMOS spectrograph and consists of two parts: zCOSMOS-bright and zCOSMOS-deep. The zCOSMOS-bright is purely magnitude-limited and covers the whole area of  $1.7 \text{ deg}^2$  of the COSMOS field. It provides redshifts for  $\sim 20\,000$  galaxies down to  $I_{AB} \lesssim 22.5$  as measured from the HST-ACS imaging. The success rate in redshift measurements is very high, 95% in the redshift range  $0.5 < z < 0.8$ , and the velocity accuracy is  $\sim 100 \text{ km s}^{-1}$  (85). Each observed object has been assigned a flag according to the reliability of its measured redshift. This work is based on the the zCOSMOS-bright survey final release: the so-called 20k sample, totaling 16 623 galaxies with  $z \lesssim 2$  and secure redshifts measurements with an actual reliability of 99%.

For objects brighter than  $I_{AB} = 22.5$  and without secure spectroscopic redshift<sup>1</sup>, photometric data from the COSMOS survey provide good-quality photometric redshifts<sup>2</sup> (86). Based on a comparison with the zCOSMOS spectroscopic redshifts, Ilbert et al. (86) estimated an accuracy of  $\sigma_{z_{phot}} = 0.007 \times (1 + z_s)$  for galaxies brighter than  $I_{AB} = 22.5$ .

For all galaxies brighter than  $I_{AB} = 22.5$ , absolute rest-frame magnitudes and stellar masses were obtained using standard multi-color spectral energy distribution (SED) fitting techniques. SED fitting was performed using the secure spectroscopic redshift, if available, or the photometric one. Stellar masses were obtained using the *HyperZmass* code (87, 88), by assuming a Chabrier initial mass function (IMF)<sup>3</sup> (89). *HyperZmass* uses the SED fitting technique, computing the best SED fit by minimizing the  $\chi^2$  between observed and model fluxes. When the redshift is known, the best SED fit and its normalization provide an estimate of the stellar mass contained in the observed galaxy. More information on sample and mass completeness can be found in Vitale et al. (62).

#### 3.1.1 Analyzed galaxy sample

For my analysis, I have used the Bright zCOSMOS spectroscopic catalog (*v4.12* version). For AGN that are more luminous than the host galaxy, such as the type-1 AGN,

---

<sup>1</sup>Redshift inferred from spectral lines.

<sup>2</sup>The redshift determination technique uses photometry instead of spectra. Photometry is the brightness of the object viewed through various standard filters, each of which lets through a relatively broad spectrum of colors.

<sup>3</sup>Empirical function that describes the distribution of initial masses for a population of stars.

whose emission is not screened by the dusty torus (AGN-unification model, 90), we are unable to see the emission lines from the host galaxy. Therefore, type-1 AGN have been removed to avoid overshining. This was performed by excluding all objects with broad emission lines. Furthermore, all sources without an indication of well-measured spectroscopic redshift have been excluded from the sample. These and the broad-line AGN constitute, all together, about 6% of the original sample within  $0.1 < z < 1$ . In particular, I excluded 892 low-flag objects and 35 broad-line AGN. There are 15 715 galaxies flagged reliable. Another significant fraction of galaxies is lost during the binning process because underrepresented regions of the redshift-stellar mass diagram were excluded (see binning in Fig. 3.1). After applying these selection criteria, it is possible to study roughly half of the original zCOSMOS-Bright sample.

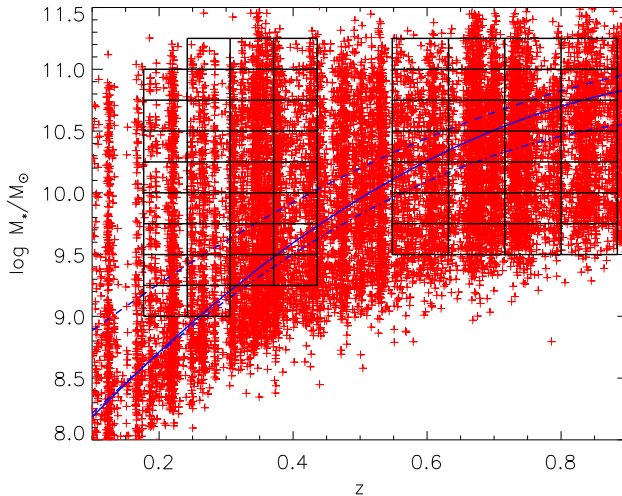


**Figure 3.1:** Stellar mass of zCOSMOS 20k galaxies selected for this study (secure flags, no broad-line AGN), plotted as a function of redshift. The blue lines represent the mass completeness limits of the global galaxy population (solid), the population of early-type (dashed) and the late-type galaxies (dot-dashed). The black boxes mark the 61 mass-redshift bins that define the stacked galaxies studied with the diagnostic diagrams.

### 3. DATA

---

#### 3.1.2 Spectral analysis

To search for variations of galaxy spectral properties as a function of redshift and stellar mass, the sample was divided into bins. The bin width was tested to achieve a good S/N with the largest number of mass-redshift bins. In particular, I tested the increase in S/N according to the increase in the number of stacked spectra. The first indication of a link between total galaxy stellar mass ( $M_*$ ) and classification in the spectral types - AGN, composite galaxies, star-forming galaxies - made me opt for a fine grid in  $M_*$ . The variations I applied to the size of the redshift intervals did not affect the classification significantly. I afterwards decided for the number of  $z$  bins to be equal to 8, with a redshift step  $\sim 0.1$  dex. The sample was divided into nine mass bins, with a mass step of 0.25 dex. The bins include several hundreds of objects for each redshift- and mass range. Mass completeness is achieved when galaxies above the computed completeness curves (87) are included in the bins (Fig. 3.1). While at lower redshifts most bins lie above the completeness limits, at higher redshifts roughly half of the bins are placed below the completeness curves. Although in this case the sample suffers from incompleteness, I have chosen to study all high-redshift bins to probe a dynamical range of masses comparable with the low-redshift case.

The bins were chosen according to these additional considerations:

- below  $10^9$  and above  $10^{11.25} M_\odot$ , objects are poorly represented in the sample. The S/N ratio of the average spectra made out of the stacking of an insufficient number of galaxies would not allow precise line measurements;
- eight redshift bins are a good compromise between the need to explore the cosmological evolution of the galaxy spectral properties and to keep the number of objects per bin above  $\sim 100$ . Four redshift bins cover the redshift ranges of each diagnostic diagram:  $z \lesssim 0.5$  for the “low-redshift diagnostic diagram”, which uses [NII], H $\alpha$ , and [SII] lines;  $z \gtrsim 0.5$  for the “high-redshift diagnostic diagram”, which uses [OII].

For diagnostic diagrams based on [NII], H $\alpha$ , [OIII] and H $\beta$ , the analyzed rest-frame spectral range is 4800 to 6750 Å. The zCOSMOS spectra cover the 5650 to 9550 Å range after cutting off 100 Å at both extremes to avoid noisy regions, where the flux calibration is more uncertain. The useful redshift range for the low-redshift diagnostic

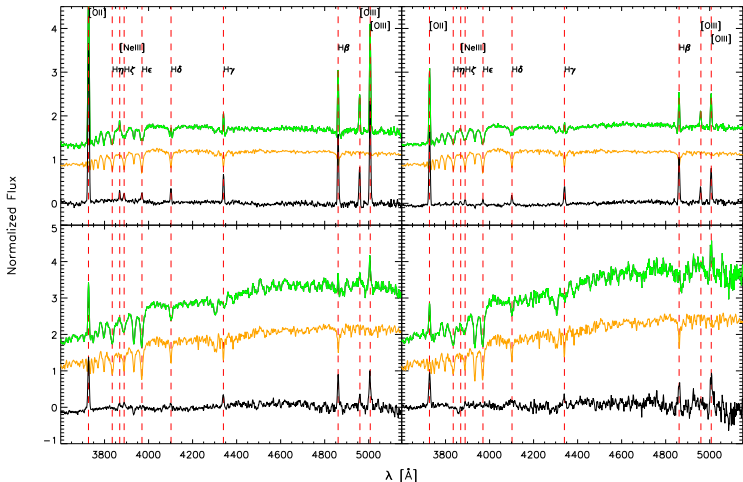


**Figure 3.2:** Examples of stellar continuum subtraction at  $z > 0.5$ . For each panel, the original stacked spectrum (green), the most suitable stellar continuum to be subtracted (orange) and the resulting zCOSMOS stacked spectrum after the stellar continuum subtraction (black) are shown. The main emission and absorption lines are labeled at the top. From top to bottom and from left to right, total stellar mass and redshift increase.

diagrams is then  $0.177 \leq z \leq 0.436$ . In the same way, the redshift range for the high-redshift diagnostic diagram is  $0.548 \leq z \leq 0.884$ .

After binning the sources in the mass-redshift plane, the spectra of each bin were stacked. Since stacked spectra are the result of the average of up to several hundreds of single galaxy spectra included in a single bin, the gain in S/N is considerable and allows a more accurate line fitting. To create the composites, each spectrum was shifted to the rest-frame. The spectra were normalized in wavelength ranges always present in the observed spectroscopic window and lacking prominent spectral features.

A suitable model of stellar continuum was subtracted from each stacked galaxy spectrum to obtain an almost pure emission-line spectrum. To subtract the stellar component, I used the *Bruzual and Charlot (BC) library*, which is a library of stellar population synthesis models computed by Bruzual and Charlot using their *isochrone synthesis*

### 3. DATA

---

*spectral evolutionary code* (91). This code predicts the spectral evolution of stellar populations in various ranges of ages and metallicities at a resolution of 3 Å across the whole wavelength range (from 3200 Å to 9500 Å). Models with different time scales of star formation, initial mass functions, and metallicities, reproduce the spectral and photometric properties of nearby galaxies with various morphological types well, from young irregulars to elliptical galaxies. For each BC template, five spectra with increasing B(E-V) values (0.2, 0.4, 0.6, 0.8 and 1) were created to take reddening due to dust into account. A total of 234 stellar templates were compared with the stacked spectra to find the one most suitable to be subtracted from each composite. The continuum subtraction task degrades the resolution of the template spectra to that of zCOSMOS ( $R \sim 600$  at  $2.5 \text{ \AA/pixel}$ ). The spectral resolution is related to the resolving power of the spectrograph, defined as  $R = \lambda/\Delta\lambda$ , where  $\Delta\lambda$  is the smallest difference in wavelengths that can be distinguished at a wavelength of  $\lambda$ . The template was chosen to have the lowest residuals in pre-selected regions of the continuum-subtracted sample that were free from strong emission lines. Fig. 3.2 illustrates four examples of stellar continuum subtraction at  $z > 0.5$ .

At this point, it is possible to measure the emission lines. The measurement errors of the emission lines in the stacked spectra corrected for the stellar absorption are typically lower than 20%, estimated on the basis of repeated independent measurements. The errors mainly depend on the line intensity and whether the emission line is blended with other spectral features. The resolution of the zCOSMOS spectra is not sufficient to resolve the [OII] doublet, which always appears as a blended feature. For the highest stellar masses, the emission line measurements are more difficult because the S/N ratio is lower due to poor statistics. Moreover, the lines become weaker and the continuum stronger, especially at high redshift. Observed fluxes are corrected for interstellar extinction using the Balmer decrement, which is the ratio of Balmer-line intensities such as  $H\alpha/H\beta$ ,  $H\gamma/H\delta$  (see Appendix).

### 3.2 SDSS

The Sloan Digital Sky Survey (SDSS) is a photometric and spectroscopic survey that covers one-quarter of the celestial sphere in the north Galactic cap (92, 93). It uses a dedicated 2.5 m wide-angle optical telescope at Apache Point Observatory in New

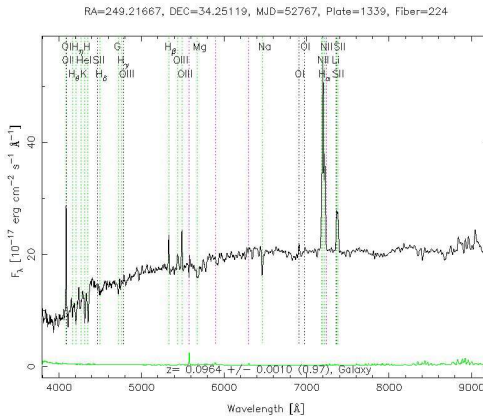


**Figure 3.3:** Example of SDSS galaxy spectrum. The most prominent spectral features are labelled on top. Redshift, redshift uncertainty, and spectral class are indicated at the bottom of the figure.

Mexico, the United States. The spectra have an instrumental velocity resolution of  $\sigma \sim 65$  km/s in the wavelength range 3800 – 9200 Å. The identified galaxies have a median redshift of  $z \sim 0.1$ . Spectra are taken with 3'' diameter fibers (5.7 kpc at  $z \sim 0.1$ ), which makes the sample sensitive to aperture effects. This means that low-redshift objects are likely to be dominated by nuclear emission (see e.g. 94). An example of SDSS spectra is presented in Fig. 3.3.

Physical properties of galaxies from the SDSS have been derived and listed in publicly available catalogs. The Max-Planck-Institute for Astrophysics (MPA)-Johns Hopkins University (JHU) Data Release 7 (DR7) of spectrum measurements (<http://www.mpa-garching.mpg.de/SDSS/DR7/>) contains the derived galaxy properties from the MPA-JHU emission line analysis for the SDSS DR7 (95). It represents a significant extension in size ( $\sim 2$  times, from 567 486 to 922 313 objects) and a general improvement over the previous DR4 data set. This is due to refinements both in the reduction and analysis pipelines. In addition, new stellar population synthesis spectra for the stellar continuum subtraction (updated Bruzual & Charlot, 91) are used. One caveat of the MPA-JHU DR7 is that it does not differentiate between narrow and broad emission lines. Since

### 3. DATA

---

the narrow component alone is used in the diagnostic diagrams, this introduces a bias. An underestimation of the flux due to line fitting uncertainties could lead to galaxies being misclassified. Ossa et al. (96) estimate that 1.3% of the galaxies in the SDSS DR7 present broad components in their spectra. They also show that when a double Gaussian fit (for narrow and broad components of the same line) is performed, it is possible to recover the misclassified objects and increase the number of sources in the AGN region of the diagnostic diagrams.

### 3.3 FIRST

The Faint Images of the Radio Sky at Twenty-Centimeters Survey (FIRST, 97) makes use of the Very Large Array (VLA) in the B-array configuration to produce a map of the 20 cm (1.4 GHz) sky emission with a beam size of 5.4" and an rms<sup>1</sup> sensitivity of about 0.15 mJy/beam. It represents the high-resolution counterpart of the NRAO VLA Sky Survey (NVSS, 98) and has yielded accurate measurements ( $< 1''$  rms) of radio position of faint compact sources. The survey covers an area of about 10 000 deg<sup>2</sup> in the north Galactic cap, corresponding to the sky regions investigated by SDSS, and observed  $\sim 10^6$  sources. At the 1 mJy source detection threshold, about one third of the FIRST sources show resolved structures on scales of 2" – 30" (71). The FIRST latest catalog (released in 2008) contains information on the continuum flux density peak ( $F_{\text{peak}}$ ) and the integrated flux density ( $F_{\text{int}}$ ) at 1.4 GHz, which allow separating resolved from unresolved sources. Example of radio emitters observed with VLA are presented in Fig. 3.4.

### 3.4 Cross-matched SDSS-FIRST sample

For this work, I have cross-matched the optical (SDSS) and radio (FIRST) galaxy samples, with the aim of selecting radio emitters with optical observed counterpart. The cross-match allows for a large and statistically relevant investigation of combined optical-radio properties of galaxies.

---

<sup>1</sup>root mean square or quadratic mean, the statistical measure of the magnitude of a varying quantity.

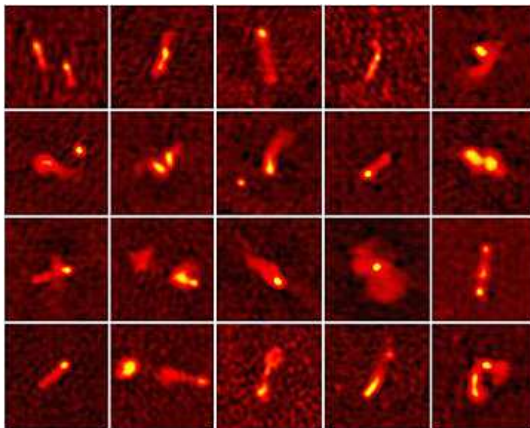


Figure 3.4: Radio galaxies observed with VLA.

### 3.4.1 Selection of SDSS galaxies from the DR7

Galaxies at very low redshift have angular sizes larger than the size of the fiber used for observations (for the SDSS,  $3''$ ). Part of the emission coming from the outer regions of the galaxies could be missed. To take the aperture effect into account and following Kewley et al. (94), I consider only line-emitting sources with  $z > 0.04$ .

Seyfert galaxies usually have bright emission lines, while LINERs present much weaker emission lines, detected at low confidence level. In particular, those line emitters are thought to be the so-called “fake-LINERs” and “retired galaxies” (99, 100, 101), which present low  $H\alpha$  EW and are possibly powered by old post-AGB stars. Galaxies with low EW measurements have been proven to have properties similar to LINERs and to constitute, together with LINERs, the class of low-excitation radio-AGN (102). Therefore, by applying a cut in EW when selecting galaxies for the cross-matched sample (e.g.  $EW < 3\text{\AA}$ ), it is likely to lose a part of these optically-weak emitters. In order not to be biased against LINERs and to represent as many of them as possible in the diagnostic diagrams, I opted not to apply any EW cut. Instead, I included in the sample only those galaxies whose error on the measurement of the EW of the lines that appear in the diagnostic diagrams is less than 30%. This choice was supported by several tests

### 3. DATA

---

on the cross-matched sample. The weakest emission line has been found to be the [OI] line. With 30% error cut and, additionally, a more severe cut in the measured EW of this line ( $EW > 3\text{\AA}$ ), I am left with very few SDSS galaxies (1 808). The second most affected line is [OIII] (6 138 fulfill the requirement), followed by  $H\beta$  (7 573 galaxies). The possibility of setting this condition for all three weakest emission lines has not been considered, since it would imply working with a rather small sample of radio emitters (1 725 galaxies) and poor statistics. The same cut on the strongest lines -  $H\alpha$ , [NII] and [SII] - does not exclude a significant number of galaxies.

In a cross-matched sample where I only apply the redshift cut (34 733 galaxies fulfill the requirement), the mean logarithmic values of the emission line ratios are higher ( $\log [\text{NII}]/H\alpha = -0.13$ ,  $\log [\text{SII}]/H\alpha = -0.29$ ,  $\log [\text{OI}]/H\alpha = -0.91$ ) than when I also apply the 30% error cut on all the emission lines (9 594 galaxies,  $\log [\text{NII}]/H\alpha = -0.24$ ,  $\log [\text{SII}]/H\alpha = -0.42$ ,  $\log [\text{OI}]/H\alpha = -1.22$ ), indicating in the second case a shift in the classification from LINERs to starburst galaxies.

Both  $H\beta$  and [OIII] appear in all the diagnostic diagrams. Their ratio is strongly affected by the weakness of the components, especially the  $H\beta$  line. This line is often superimposed on an absorption component, making its strength dependent on the quality of the stellar continuum subtraction. In the case of a sample in which a cut in redshift and EW error has been applied to all emission lines, as well as the requisite  $EW > 3\text{\AA}$  for the  $H\beta$  and [OIII] lines (5 298 galaxies), the line ratios [NII]/ $H\alpha$ , [SII]/ $H\alpha$ , and [OI]/ $H\alpha$  slightly decrease further, moving the bulk of the population to the SF region. This is probably due to the lack of LINERs. The  $\log [\text{OIII}]/H\beta$  ratios increase from  $-0.01$  of the precedent case to  $0.12$  instead, becoming more characteristic of Seyfert galaxies. This leads to the conclusion that one misses some of the weakest optical emitters (e.g. LINERs) when applying an EW error cut on all the emission lines, but is still left with a significant number of sources. In Kewley et al. (26), the authors prefer to consider an  $S/N > 3$ , to be certain that the quality of the galaxy spectra is high enough to make accurate line measurements. Stasinska et al. (103) mention that this cut does not change the visual shape of the galaxy distribution in the diagnostic diagrams, but it reduces the proportion of the objects in the right wing of the distribution.

After applying redshift ( $z > 0.04$ ), and EW error cut (error on the EW measurements of all lines that are used in the diagrams is  $< 30\%$ ), the resulting sample of SDSS

### 3.4 Cross-matched SDSS-FIRST sample

Emission line	$EW_m$	$ERR_{abs, m}$	$ERR_{rel, m}$
H $\alpha$	40.56	0.43	0.01
H $\beta$	8.12	0.32	0.07
[OIII] $\lambda$ 5007	15.53	0.36	0.08
[OI] $\lambda$ 6300	2.21	0.22	0.14
[NII] $\lambda$ 6583	19.42	0.31	0.02
[SII] $\lambda\lambda$ 6717, 6731	13.30	0.52	0.06

**Table 3.2:** Line EW statistics on the SDSS DR7. Col. 2: Mean values of the EW of the lines in Å. Col. 3 and 4: Absolute and relative mean errors on the EW measurements.

galaxies with emission line measurements from DR7 contains 79 919 galaxies, which is about how many objects have been used by Kewley et al. (26). In that case, the authors made use of a previous SDSS data release (DR4) containing fewer sources, thus our selection criteria are more restrictive. Table 6.1 summarizes the statistics on the EW of the lines for SDSS objects that have been included in the final cross-matched sample.

By using low-redshift emission-line diagnostic diagrams (4, 23, 24, 25, 26), one can represent galaxies up to  $z \sim 0.4$ . Beyond this redshift, spectral features like the H $\alpha$  and [N II] lines are redshifted out of the rest-frame spectra and cannot be observed. The [OII]/H $\beta$  versus [OIII]/H $\beta$  diagram (104, 105, 106, 107) represents a higher-redshift option to the more classic red diagnostic diagram. However, I estimate the sources in our sample placed at  $z \gtrsim 0.5$  to be less than 1%, and the use of another tool is not worth.

#### 3.4.2 Optical-radio cross-matching

For generating the cross-matched FIRST/SDSS sample, matching results provided by the SDSS DR7 via Casjobs (108), an online workbench for large scientific catalogs, were used. Results are based on a matching radius of  $1''$ . The resulting sample contains 37 488 radio emitters and represents nearly 4% of the  $\sim 10^6$  FIRST and SDSS sources. SDSS spectra are available for all objects of the matched sample. Some objects have been lost during the matching procedure owing to the centering problems of radio emission with respect to the optical emission, especially in the case of extended sources. Another considerable number of radio emitters that have an optical counterpart are

### 3. DATA

---

left out of the sample after applying the redshift cut ( $z > 0.04$ ) and the error cut on the EW of the lines involved in the diagnostic diagrams. Best et al. (109) find that radio galaxies extracted from the main spectroscopic sample of the SDSS reside in very massive early-type galaxies, with weak or undetectable optical emission lines. This further proves that the cross-matching process implies the loss of many radio emitters that do not have optical counterparts with emission lines. The final cross-matched sample consists of 9 594 objects, which corresponds to 25.6% of the full cross-matched optical-radio sample, and  $\sim 1\%$  of all the galaxies in the FIRST radio sample and the MPA-JHU data release.

The radio luminosity has been calculated from the integrated flux provided by the FIRST catalog, assuming a cosmology with  $H_0 = 70 \text{ km s}^{-1} \text{ Mpc}^{-1}$ ,  $\Omega_M = 0.3$ ,  $\Omega_\Lambda = 0.7$ .

#### 3.4.3 Completeness of the sample

Sample completeness is strongly related to the completeness of the parent samples (SDSS and FIRST). The SDSS spectroscopic sample can be considered as complete, in the sense that the biggest incompleteness comes from galaxy misclassifications owing to mechanical spectrograph constraints (6%, see 110), which causes slight underrepresentation of high-density regions. For a few sources ( $< 1\%$ ), the redshift cannot be determined or it has been derived in an incorrect way. Moreover, a few targets ( $\sim 1\%$ ) are contaminated by galactic stars. According to Blanton et al. (111), the mechanical constraints are related to the impossibility of placing the fibers close enough to each other. When two galaxies are found to have a small separation, only one source is chosen (independently from its magnitude or surface brightness), and this does not result in a luminosity bias. Reliability and accuracy of the catalog of radio sources extracted from the FIRST images is discussed in White et al. (112). The authors state that source positions are  $\sim 1''$  precise, and the flux density scale is accurate to 5%.

### 3.5 Effelsberg survey

In order to obtain radio spectra of some of the sources in the cross-matched optical-radio sample, I decided to observe a radio-bright subsample with  $F_{20\text{cm}} \geq 100 \text{ mJys}$ , where  $F_{20\text{cm}}$  stands for integrated flux at 20 cm, at two different radio frequencies.



**Figure 3.5:** The Effelsberg 100m radio telescope. Credits: R. Junkers, MPI for Radioastronomy.

Observations were performed at the Effelsberg radio telescope. Sources are listed in Tab. 6.2.

Effelsberg is a 100m single dish telescope (Fig. 3.5) located near Bad Muenstereifel, Germany. It is the second largest fully steerable single-dish radio telescopes in the world and can be used to observe radio emission from celestial objects in a wavelength range from 90 cm (300 MHz) to 3.5 mm (90 GHz). Confusion limit at 6 cm is about  $0.20 - 0.25$  mJy/ $2.4'$  beam (Reich, private communication). After a successful proposal run, I was granted 50h observing time. Objects with integrated  $F_{20\text{cm}} \geq 100$  mJys were selected from the SDSS-FIRST parent sample (about  $4 \times 10^4$  sources) with the goal of studying the spectral index distribution and polarization of the sources across the three emission-line diagnostic diagrams. The selection resulted in a sample of 263 sources, among which 175 present the emission line measurements used in the optical diagnostic diagrams. Furthermore, only galaxies with  $z > 0.04$  were selected to avoid aperture effects (94), for a total of 150 radio emitters. A further cut in signal to noise (S/N) on the equivalent width of the emission lines involved in the diagnostic diagrams leads to a sample of 119 galaxies in the [N II]-based diagram ( $S/N > 3$  for [N II], O[III], H $\alpha$  and H $\beta$ ), 100 galaxies in the [S II]-based diagram ( $S/N > 3$  for [S II] doublet, O[III], H $\alpha$  and H $\beta$ ), and 100 galaxies in the [O I]-based diagram ( $S/N > 3$  for [O I], O[III], H $\alpha$  and H $\beta$ ).

### 3. DATA

---

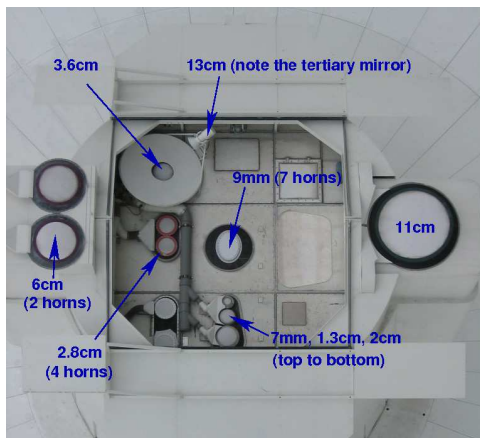


**Figure 3.6:** The receivers at the secondary focus of the Effelsberg 100m radio telescope. Credits: MPI for Radioastronomy.

#### 3.5.1 Observations

Observations were performed between February and October 2013. Each source was observed at 2.8 cm (10.45 GHz) and 6 cm (4.85 GHz) to derive radio spectral indexes and polarization degrees from quasi-simultaneous observations (to avoid time variability effects). The receivers used in these observations are mounted on the secondary focus of the 100-m Effelsberg antenna (Fig. 3.6). The receivers at 4.85 and 10.45 GHz have multi-feed capabilities with 2 and 4 horns, respectively, allowing real-time sky subtraction in every subscan measurement. I have used cross-scanning in azimuth and elevation to determine the total intensity and polarization characteristics. All sources in the sample are fairly bright, thus standard cross-scans, with 4 to 12 subscans per each scan were used, according to the source flux density (see Fig. 3.7). Fainter sources needed to be observed with a higher number of subscans per scan (e.g. 12 subscans), or with multiple scans to be averaged in the data reduction process. The cross-scan length was chosen to be about 3.5 times the beam size at each frequency, for a correct subtraction of linear baselines. This translates into on-source scan integration times

between 100 and 300 sec per source and per frequency.

Before combining, individual subscans were checked to remove those affected by radio frequency interference, bad weather, or detector instabilities (113). The calibration sources 3C286, 3C295 and NGC7027 were regularly observed to correct for both time-dependent gain instabilities and elevation-dependent sensitivity of the antenna, and to perform the absolute flux calibration (114). Data reduction was performed by using a set of standard Python and Fortran routines. The measurement of flux densities from the single-dish cross-scans was done by fitting Gaussians to the detected signal.

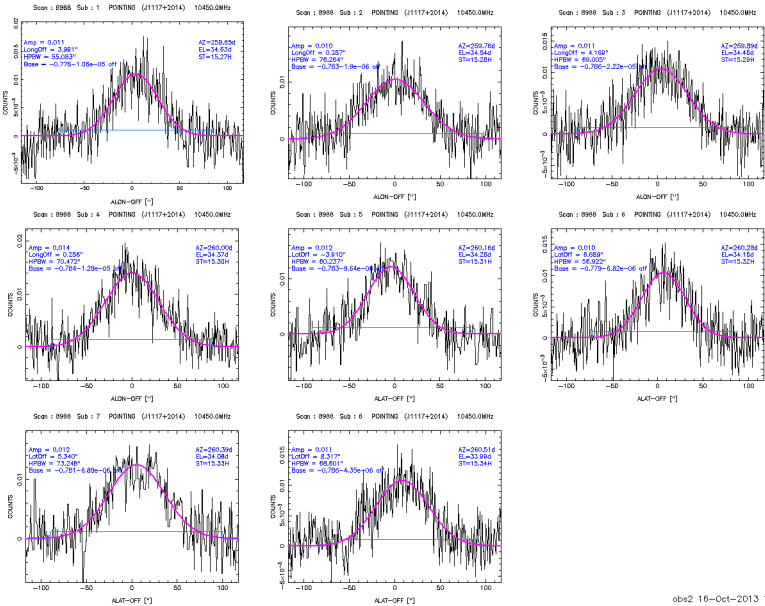


**Figure 3.7:** Cross-scans observation at 2.8 cm of a radio emitter of the sample. This scan contains 8 subscans, 4 in vertical and 4 in horizontal direction. Flux density is determined by a Gaussian fit.

### 3. DATA

---

#### 3.5.2 Selection and completeness of the Effelsberg sample

The Effelsberg sample selects all the cross-matched SDSS-FIRST radio emitters that have an integrated flux at 20 cm  $> 100$  mJys at  $0.04 < z < 0.4$ . The applied radio-flux lower cut automatically selects more active galaxies (AGN in particular) and metal-rich star-forming galaxies (see Vitale et al. 73, Fig.1). The redshift distribution of the Effelsberg sample peaks at  $z \sim 0.1$ . At this redshift, radio-quiet (but not silent) AGN lie in spiral hosts and are mainly classified as Seyfert galaxies. They have mostly weak radio jets (115). Because of this, the sample does not contain many FR II galaxies. However, since the sample is mainly composed by radio-loud objects, due to the lower cut in radio flux, some sources are FRI with particularly strong emission lines.

#### 3.6 Aperture effect

Aperture biases are particularly important in emission-line studies. Spectroscopic observations are performed using different aperture sizes, depending on the specific instrument. This problem plays a critical role in distinguishing the main contribution to galaxy emission. The so-called aperture effect tells us that the shape and size of the instrument aperture influences the galaxy classification. Big fibers and slits select emission from all over the galaxy, hence several contributions to the line emission (AGN from the nucleus, starburst from the outer regions of the host galaxy) are present. On the other hand, a smaller aperture would mainly select light coming from the nucleus and the bulge, missing the disk where most of the star formation takes place. For example, SDSS data are known to be affected by an aperture effect because of the large fixed size ( $3''$ ) of the fiber used for observations, which includes on average  $> 20\%$  of galaxies area at  $z > 0.04$  (26). Therefore, the stellar contribution to the emission from the host causes a large number of sources to be classified as transitional objects in the diagnostic diagrams. The same argument applies at higher redshift, where the slit width becomes similar to the typical angular size of galaxies. Furthermore, higher-redshift galaxies present higher star formation rates, so the effect of host galaxy dilution of the AGN signatures could be even more important and yield more often composite signatures. From this point of view, with the  $1''$  width of the slits used for the zCOSMOS observations and a seeing always better than  $1.2''$  (79), the zCOSMOS sample is less sensitive

to contamination from emission coming from the most outer regions of the galaxies than other studies at similar redshift. Conversely, aperture effects are more severe for SDSS galaxies, where a correction is needed.

The conventional belief that smaller apertures select more AGN-like emission has been challenged in Shields et al. (116). The authors showed that for many composite objects identified in the Palomar spectroscopic survey (117) the observed line-ratios do not appear more AGN-like with smaller apertures (10 – 20 pc). The bias introduced by the fiber/slit observational technique depends on the morphological type of the observed galaxy. Even though the star-forming regions are mainly located at the center of bulge-dominated galaxies, some bright star-forming regions can be located in the outer regions of the disk, or all over the galaxy, like in irregular galaxies. The aperture effect problem remains controversial and it is worth more studies.

### 3. DATA

---

## 4

# Stellar mass-AGN relation in intermediate redshift galaxies

## 4.1 Introduction

AGN can be identified by a variety of methods: an unusually blue continuum, strong radio or X-ray emission, and strong or broad emission lines. In nearby galaxies hosting low-luminosity AGN, we expect the non-stellar signal of the nucleus to be weak with respect to the one coming from the host galaxy. Therefore, one of the least biased methods to search for AGN is to conduct a spectroscopic survey of a complete, optical-flux-limited sample of galaxies and study their spectral properties.

The line-emitting gas in AGN and star-forming galaxies is powered by two different ionizing mechanisms, producing different emission line ratios: accretion around black hole and photoionization by hot massive OB stars. It is important to note that emission lines in narrow-line AGN have a considerably great ionization range and that low-ionization lines are anyhow stronger than in normal star-forming galaxies. It has been demonstrated that ordinary O-type stars do not produce sufficiently strong low-ionization lines to account for the observed AGN spectra, because they can only produce a low percentage of the total blue light at most (118). Therefore, photoionization arising from a powerful central non-thermal source is the ideal candidate for explaining the excitation mechanism in galaxies that display strong low-ionization emission-lines (119). Emission-line diagnostic diagrams (23, 24, 94, 106, 107) represent a powerful tool for probing the nature of the dominant ionizing source in galaxies, hence for distinguish-

#### 4. STELLAR MASS-AGN RELATION IN INTERMEDIATE REDSHIFT GALAXIES

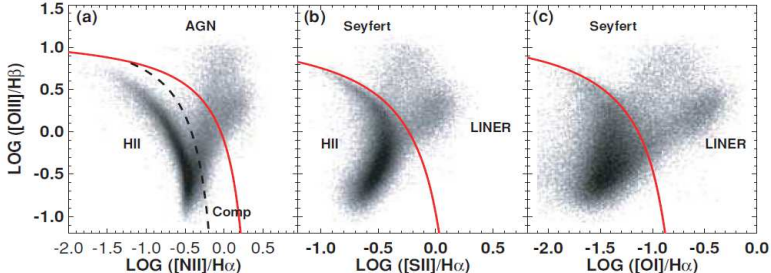


**Figure 4.1:** Plot from Kewley et al. (26): (a) The  $[\text{N II}]/\text{H}\alpha$  versus  $[\text{O III}]/\text{H}\beta$  diagnostic diagram. The extreme starburst line (red) is from Kewley et al.(25), while the black line is the Kauffmann et al.(4) classification. (b) The  $[\text{S II}]/\text{H}\alpha$  versus  $[\text{O III}]/\text{H}\beta$  diagnostic diagram; (c) the  $[\text{O I}]/\text{H}\alpha$  versus  $[\text{O III}]/\text{H}\beta$  diagnostic diagram.

ing between objects dominated by star formation and galaxies where nuclear activity is more relevant. Narrow-line AGN can be identified by the ratio of some distinctive emission-lines, such as  $[\text{NII}]/\text{H}\alpha$  or  $[\text{SII}]/\text{H}\alpha$  and  $[\text{OIII}]/\text{H}\beta$ . Fig. 4.1 shows three examples of diagnostic diagrams from Kewley et al. (26). The lines that appear in the reddest part of the spectrum are shifted out of the visible wavelength range for  $z > 0.5$ . In this case, it is possible to use the  $[\text{OII}]$  line instead (105, 106, 120), which is optically visible up to  $z \sim 1$ .

According to the “downsizing” scenario (59, 121, 122, 123, 124, 125), the sites of active star formation include high-mass galaxies ( $M_* \sim 10^{11} M_\odot$ ) at high redshift ( $z \gtrsim 1$ ) but only intermediate- and low-mass galaxies at  $z \lesssim 1$ . This scenario is supported by several studies; it has been found, for instance, that luminous and massive spheroidals build up most of their stellar mass prior to  $z \simeq 1$ , while low-mass ellipticals continue to grow after this cosmic time (126, 127, 128, 129). Downsizing may be a natural expectation in a hierarchical galaxy formation scenario, provided that there is a mechanism that quenches star formation at earlier times in massive galaxies. As a support to downsizing and the link between mass and galaxy evolution, Bundy et al. (130) found that the relative abundance of red galaxies with intermediate stellar mass ( $M \approx 6 \times 10^{10} M_\odot$ ) increases by a factor of 3 from  $z \sim 1.2$  to  $z \sim 0.55$ , while the number of blue late-type galaxies declines significantly.

I aim at investigating whether it is possible to highlight some evidence of AGN activity in suppressing star formation and leading to an increase in the number of red galaxies, with a particular focus on a possible trend of the galaxy total stellar mass. Here I analyze the evolution of galaxy spectral properties up to  $z \sim 1$  by using galaxies from the zCOSMOS-Bright 20k sample (79). With the large number ( $\sim 2 \times 10^4$ ) of observed objects, it is possible to measure emission lines from high S/N stacked spectra. This attempt has been previously made at low-redshift ( $z < 0.1$ ) and the analysis is now extended to redshift up to  $z \sim 1$ . Kauffmann et al. (4) found, by using Sloan Digital Sky Survey (SDSS) data, that local galaxies divide into two distinct families at a stellar mass threshold of  $3 \times 10^{10} M_{\odot}$ . The least-massive galaxies show young stellar populations and the low concentrations typical of LTG. As the stellar mass increases, galaxies show older stellar populations and higher concentrations, typical of ETG. By using emission-line diagnostic diagrams, Kauffmann et al. shown a dependence of the AGN-detection rate on mass, although the authors warned that many objects are classified as “composites” (contributions to the emission-line spectrum come from both star formation and AGN) because of the large size of the SDSS fiber, which can collect up to 40% of the total light from the galaxy (see Sec. 3.6). Blue star-forming objects have been found to have masses at the low end of the galaxy mass function, while the majority of the ETGs lie at the high end of the mass function (5, 28). Very recently, however, Aird et al. (131) argued that the finding of more AGN in massive hosts is due to selection effects. These seem to be driven by the Eddington-ratio distribution of AGN in galaxies of certain stellar mass. In particular, AGN are more easily detected in massive hosts because sources accreting at low Eddington rate are more luminous than in less massive hosts.

In this work I explore the stellar mass - AGN detection rate relation for galaxies placed at intermediate redshift ( $0.1 < z < 1$ ). I show that not only the relation holds at higher redshifts than those investigated by Kauffmann et al., but the galaxies with progressively higher values of stellar mass also show older stellar populations and metallicities, in agreement with an AGN-feedback quenching scenario.

## 4. STELLAR MASS-AGN RELATION IN INTERMEDIATE REDSHIFT GALAXIES

---

### 4.2 Emission-line diagnostic diagrams

The optical spectra of most of nearby AGN are dominated by emission lines of low-ionization species such as [OI], [OII] and [SII] (117). These emission lines, when compared to the strength of Balmer lines such as  $H\alpha$  and  $H\beta$ , can provide an indication on the galaxy main ionizing mechanism. There are currently many emission-line diagnostic diagrams that make use of low-emission line ratios to be able to distinguish between AGN- and starburst-dominated objects. The classification of galaxies is based on the position that objects assume in the diagnostic diagrams. Fig. 4.1 from Kewley et al. (26) shows the three most used optical emission-line diagnostic diagrams.

AGNs have larger [OIII]/ $H\beta$ , [NII]/ $H\alpha$ , [SII]/ $H\alpha$  and [OII]/ $H\alpha$  values than starbursts and are clearly separated from the loci formed by star-forming galaxies. Nevertheless, some galaxies present intermediate properties and show AGN-like and stellar photoionization-like emission lines.

In this work, the following emission-line diagnostic diagrams are used:

- [NII]/ $H\alpha$  versus [OIII]/ $H\beta$  ( $z < 0.436$ ) (4, 23, 24, 25, 26)
- [OII]/ $H\beta$  versus [OIII]/ $H\beta$  ( $z > 0.548$ ) (104, 105, 106, 107)
- MEx diagram (132)

The redshift range  $0.436 < z < 0.548$  was excluded from the study because [NII] and  $H\alpha$  are redshifted outside the optical spectra and [OII] is not yet visible in the blue part of the spectral range. The same grid of stellar mass and redshift bins is kept for the MEx diagram.

#### 4.2.1 Low-redshift diagnostic diagrams

In the [NII]/ $H\alpha$  versus [OIII]/ $H\beta$  or Baldwin-Phillips-Terlevich (BPT) diagram (23), galaxies are distributed in two arms. The increase of the [NII]/ $H\alpha$  ratio is a linear function of the nebular metallicity and presents a saturation point (133, 134, 135) above which any additional increase in the [NII]/ $H\alpha$  value is only due to AGN contribution (26, 103). The BPT emission-line diagnostic diagram makes use of different demarcation curves, both theoretical and based on observations. The first curve was derived theoretically by Kewley et al. (25) to find an upper limit for star-forming galaxies

## 4.2 Emission-line diagnostic diagrams

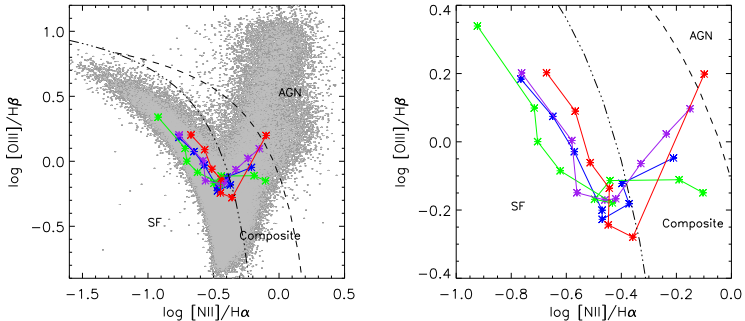


**Figure 4.2:** Classical low redshift diagnostic diagram of zCOSMOS galaxies. A theoretical demarcation curve (dashed, from Kewley et al. 25) separates star-forming galaxies and composites from AGN, while an empirical demarcation curve (three-dot-dashed, from Kauffmann et al. 27) separates pure SFGs from composites and AGN. Asterisks represent galaxy stacked spectra. Colors represent the redshift bins:  $0.177 < z < 0.242$  (blue),  $0.242 < z < 0.306$  (green),  $0.306 < z < 0.371$  (purple), and  $0.371 < z < 0.436$  (red). The total stellar mass increases from left to right. In the left panel, the SDSS galaxies from Vitale et al. (73) are plotted in gray. The right panel offers a closer view of the zCOSMOS composites.

(Figs. 4.1, 4.2). Kauffmann et al. (4), using the large sample of emission line galaxies in the SDSS, defined a demarcation that traces the observed lower left branch more closely. The branch is attributed to purely star-forming galaxies. This results in a larger portion of galaxies residing on the AGN side (Fig. 4.1, left panel, dashed line, and 4.2, three-dot dashed line).

Objects that are classified as AGN in the [NII]-based diagram can be classified as star-forming galaxies in the [SII]/H $\alpha$  versus [OIII]/H $\beta$  diagram. This is thought to be related to the enhancement of [SII] lines in starburst galaxies, due to the mechanical energy released into the gas by supernovae and stellar winds (also called shock excitation, 136). However, it is still not clear whether the [SII] enhancement is driven by highly ionizing photons produced by accretion onto the super massive black hole or if the SNe winds are a sufficiently powerful source of ionization. The [SII]-based

## 4. STELLAR MASS-AGN RELATION IN INTERMEDIATE REDSHIFT GALAXIES

---

diagnostic diagram, due to fringing<sup>1</sup> and line blending, is more affected by errors and leads to a higher probability of misclassifying galaxies than the [NII]-based diagram. For these reasons, the diagnostic diagram that makes use of the [SII] doublet was not used in this work. In Fig. 4.2 (left panel), zCOSMOS stacked data superimposed on the SDSS radio emitters from Vitale et. al (73) are shown. Each color represents a different redshift bin and each asterisk along the curve represents a different mass bin. The right panel offers a zoom on the region of the diagram where data are placed. The stacked spectra show a progressive shift toward the AGN region - on the right-hand side of the diagram - for increasing stellar mass (from left to right). The objects with the highest mass are placed on the right of the Kauffmann's demarcation curve, which separates the region where galaxies start to show significant nuclear activity. The stacks follow, for a fixed redshift bin, tracks that move from the upper part of the SFGs sequence to the high-metallicity (higher [NII]) SF region (26). Objects with the highest stellar masses are classified as composites or AGN, in agreement with what was suggested by Kauffmann et al. (4) for sources at  $z < 0.1$ .

### 4.2.2 High-redshift diagnostic diagram

For the objects placed at higher redshifts ( $z \gtrsim 0.5$ ), for which we lack useful AGN-activity indicators such as the [NII], [SII] or [OI] lines, a different kind of diagnostic diagram is needed. The Lamareille et al. (106) diagnostics involves the [OII] line (Fig. 4.3) and represents a high-redshift option to the more classic diagnostic diagrams. Unfortunately, this diagram is strongly biased against composites (107), which overlap with star-forming galaxies and LINERs. The [OII] emission line is thought to be either an indicator of ongoing star formation or AGN activity, because of the relatively low ionization potential that is required compared with the [NII] or [SII] transitions. As a consequence, this diagnostic diagram cannot be considered as reliable as the set of low-redshift diagnostic diagrams (132, 137).

In this diagram it becomes necessary to correct line ratios for reddening. This is because the emission-lines that are used as indicators are placed far away from each other in the spectra, and therefore are differently affected by reddening. Another way to overcome this problem is to use the equivalent width (EW) of the emission lines. Using the

---

<sup>1</sup>Effect of observing fringe patterns in spectra. It is caused by reflections on the Charge-Coupled Device (CCD) surfaces.

## 4.2 Emission-line diagnostic diagrams

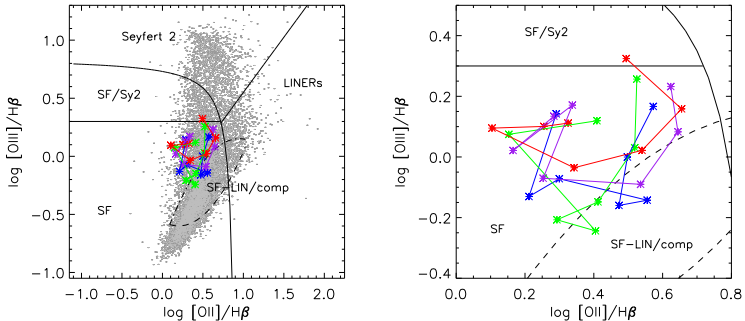


**Figure 4.3:** OII-based diagnostic diagram of zCOSMOS galaxies. Asterisks represent galaxy stacked spectra.  $[\text{OII}]/\text{H}\beta$  flux dust-corrected ratios are used. The solid demarcation lines are taken from Lamareille (107). Color represent the redshift bins:  $0.548 < z < 0.632$  (blue),  $0.632 < z < 0.716$  (green),  $0.716 < z < 0.8$  (purple), and  $0.8 < z < 0.884$  (red). Total stellar mass increases from left to right. In the left panel, the SDSS galaxies from Vitale et al. (73) are plotted in gray. The right panel shows a closer view of the zCOSMOS composites.

EW instead of the extinction-corrected fluxes does not change galaxy classification significantly (62).

To separate AGN from star-forming galaxies, I used lines that have been empirically defined by Lamareille (107) by using galaxies from the SDSS (Fig. 4.3). The left panel of Fig. 4.3 shows the distribution of SDSS galaxies (in gray) and the zCOSMOS composites superimposed on it. For every redshift bin (indicated with different colors) a higher mass means, in most cases, a shift toward higher values of  $[\text{OII}]/\text{H}\beta$ . Although the stacked galaxies show, as in the  $[\text{NII}]$  diagram (Fig. 4.2), a trend with the total stellar mass, almost all objects are placed in the SF zone. For the higher masses, I notice that some of the stacked galaxies fall in the region of mixed contribution from star-forming galaxies and LINERs, while only the point representing the highest mass at redshift  $z \sim 0.8$  falls in the star-forming/Seyfert region. This poor ability to properly classify AGN using the  $[\text{OII}]/\text{H}\beta$  ratios was also noticed in the analysis of zCOSMOS spectra for 24 micron-selected galaxies (138, 139). The diagram is also known to be the most sensitive to shocks. This might be the reason why some objects are likely to

## 4. STELLAR MASS-AGN RELATION IN INTERMEDIATE REDSHIFT GALAXIES

---

be misclassified as star-forming galaxies rather than LINERs, which would appear in a similar position along the y-axis, but at higher  $[\text{OII}]/\text{H}\beta$  values.

### 4.2.3 Mass-Excitation diagnostic diagram

Classical diagnostic diagrams are largely used by the scientific community to classify AGN from emission line ratios, especially in the optical range. Nevertheless, these diagrams present some problems that make it preferable to look for new and more effective diagnostic methods. Recently, Juneau et al. (132) adopted a new diagram (Mass-Excitation, or MEx, diagram) that can be used at higher redshift than the classical diagnostic diagrams. A correlation between galaxy stellar mass and metal content has been observed (mass-metallicity relation 140, 141) and the  $[\text{NII}]/\text{H}\alpha$  ratio is known to trace metallicity for SFGs (26, 103). For this reasons, the authors chose to substitute the emission line ratio  $[\text{NII}]/\text{H}\alpha$  in the BPT diagram with the total stellar mass. This new kind of diagnostics has the considerable advantage that one can classify all objects of a quite wide redshift range within a unique diagram. Moreover, it avoids some of the problems connected to the reliability of the  $[\text{OII}]$  diagram, though the MEx diagram suffers from more blending between LINERs and Seyferts than the latter.

The mass trend we already observed in the  $[\text{NII}]$  diagram is now clear in the MEx diagram (Fig. 4.4), where I can represent galaxies spanning the entire redshift range ( $0.18 < z < 0.88$ ). As in Figs. 4.2 and 4.3, each color represents a different redshift bin and the asterisks indicate the mass bins. At  $\log M_*/M_\odot > 10.2$ , the galaxies leave the SF region to enter the composite region of the diagram. With increasing mass, the  $[\text{OIII}]/\text{H}\beta$  ratio decreases up to the point where galaxies start to be classified as composites. Then, the ratio increases again, as already noted in the  $[\text{NII}]$  diagram. While the stellar mass tracks overlap in Figs. 4.2 and 4.3, they are parallel to each other in the SF region of the MEx diagram and systematically offset toward the AGN region for increasing redshift (Fig. 4.4). Therefore, the higher the redshift the higher the number of composites that are classified as transitional objects or AGN. In this respect, the MEx diagram shows the clearest sign of redshift evolution.

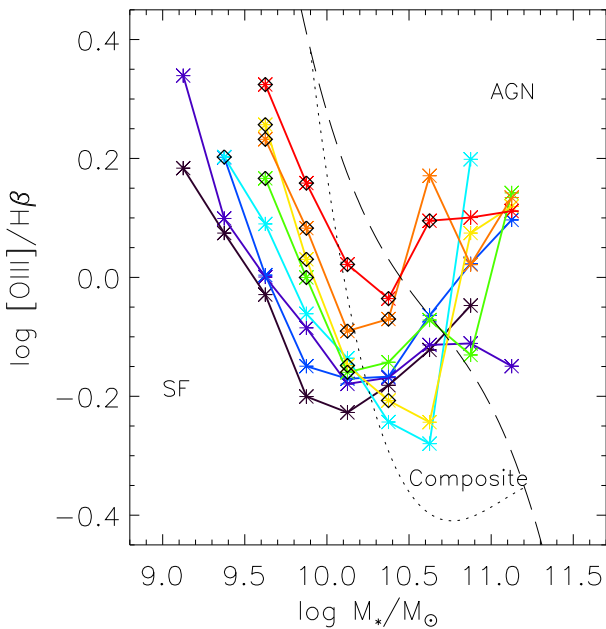


**Figure 4.4:** New diagnostic diagram by Juneau et al. (132) uses the stellar mass instead of the  $[\text{NII}]/\text{H}\alpha$  emission line ratio. In this plot, each color represents a redshift bin (the whole  $z$ -range):  $0.177 < z < 0.242$  (black),  $0.242 < z < 0.306$  (purple),  $0.306 < z < 0.371$  (blue),  $0.371 < z < 0.436$  (light blue),  $0.548 < z < 0.632$  (green),  $0.632 < z < 0.716$  (yellow),  $0.716 < z < 0.8$  (orange), and  $0.8 < z < 0.884$  (red). The mass increases from left to right along each track. The black diamonds indicate mass incompleteness (see Fig. 3.1).

## 4. STELLAR MASS-AGN RELATION IN INTERMEDIATE REDSHIFT GALAXIES

---

### 4.3 Mass evolution

Emission lines are a good indicator of star-forming or AGN activity. By means of diagnostic diagrams and spectral stacking, I found indications of a link between the total stellar mass and the chance of identifying galaxies as AGN. A temporal evolution - namely, an observed trend with redshift - is also possible but, even if present, it is obscured within the classical diagnostic diagrams. This could be because the redshift bins are too close to each other for the stacked galaxies to show a trend with redshift in the classification provided by the diagrams.

The time interval over which to probe evolutionary effects is longer when using the MEx diagram ( $0.17 \lesssim z \lesssim 0.88$ ) than when using the BPT ( $0.17 \lesssim z \lesssim 0.44$ ) or [OII]-based ( $0.55 \lesssim z \lesssim 0.88$ ) diagrams alone. Therefore, the indication of an evolutionary trend is present in the MEx diagram (Fig. 4.4). Here the data points representing galaxies in the same mass range are progressively offset to higher values of [OIII]/H $\beta$  for increasing redshift. On the other hand, along each track (fixed redshift, increasing stellar mass) the data show a metal enhancement (see also Fig. 4.2 and the Appendix). The reason for the latter could be researched in the mass-metallicity relation and the efficiency of galactic winds in removing metals from low-mass galaxies (140, 142, 143). Outflows generated by starburst winds may easily eject metal-enriched gas from low-mass galaxies placed at low redshifts, making their enrichment less significant than in massive systems (140). Moreover, low-mass systems are, according to the galaxy-downsizing scenario (124, 144, 145), at an earlier evolutionary stage, where they are still converting most of their gas into stars. For this reason, they are poorly metal-enriched compared with massive galaxies. However, it should be kept in mind that this purely magnitude-limited sample suffers from selection biases and mass incompleteness toward the highest redshifts, where most of the AGN are found among the stacked galaxies.

While the [NII] diagram nicely shows that the mass can determine the galaxy classification, the [OII]-based diagram leaves big uncertainties because of the intrinsic nature of the diagram itself (rather sensitive to shocks, it is unable to distinguish the contribution of stellar sources from AGN). Indeed, the diagram shows an overlap between star-forming galaxies and Seyfert II, as well as an overlap between the former and composites. However, the higher-mass galaxies are closer to the demarcation line and the AGN region. Using the MEx diagnostic diagram partially solves the problems related

to the ineffectiveness of the classical diagnostic diagram at high redshift ([OII]-based) and enables one to look for AGN contamination at high masses.

## 4.4 Quenching of the star formation

There is a general increase of the age of the stellar populations for increasing mass at both high and low redshifts. Appendix 8.1 summarizes all information on the stacked galaxy spectra in the stellar mass and redshift bins. The metallicity of the stellar template used for the stellar-continuum subtraction gives an important indication of the age-metallicity degeneracy (146). For a fixed redshift and along the mass sequence, the stellar populations become progressively older (in terms of time from the last burst of star formation). A young stellar population following an older one in the mass sequence presents, in most cases, a higher metallicity and a higher reddening than inferred from the stellar fit. A stellar population following one of the same age along the mass sequence is often characterized by equal or higher values of  $Z$  and  $E(B - V)_s$ <sup>1</sup>.

This evidence finds a possible explanation in the mass-assembly downsizing scenario, where most of the massive galaxies build their mass earlier than lower-mass galaxies (59, 121, 122, 123, 124, 125). According to this scenario, the number of red massive objects is constant up to  $z \sim 1$ , dominating as the main contribution to the mass population, while the number density of red galaxies with  $M_* < 10^{11} M_\odot$  increases with cosmic time. Conversely, the number density of blue galaxies decreases from  $z \sim 1$  to today. Downsizing suggests that something turns the galaxy transformation out at  $z \sim 1$ . If the most massive objects build their mass during an earlier period of time than the less massive galaxies, we expect to find older stellar populations in the former because they had more time to evolve.

If the effect of having younger stellar populations at higher redshifts was already expected from different galaxy evolutionary scenarios, the evidence of older stellar populations with increasing mass and fixed redshift points to the downsizing scenario in particular. It is likely that a mechanism acted to quench the star formation in these objects. Now the question is: can this process be an AGN-feedback? Considering the downsizing scenario where young low-mass galaxies are still undergoing star formation

---

<sup>1</sup> $E(B-V) = A(B) - A(V)$ , extinction in set bands.  $A(B)$  and  $A(V)$  are the total extinction at the B and V filter bands. Extinction is the absorption and scattering of electromagnetic radiation by dust and gas, between an emitting astronomical object and the observer.

## 4. STELLAR MASS-AGN RELATION IN INTERMEDIATE REDSHIFT GALAXIES

---

and high-mass galaxies are the product of an earlier mass assembly, the latter are passively evolving galaxies without star formation episodes. In this respect, AGN might have just suppressed star formation with their (negative) feedback by means of transforming blue galaxies into red ones that continue to accrete mass. As a support to this theory, it has been found that the stellar population of the host galaxies appears to be older after the AGN active phase (118). Currently, several theories and models include AGN feedback, but observational evidence is still needed to prove them right.

### 4.4.1 AGN identification

AGNs are clearly common amongst the high-mass bins (see Fig. 4.2 and Fig. 4.4). This is particularly true for higher redshift bins. However, some stacked spectra are placed directly on the demarcation curves that separate AGN from composites, or immediately next to them. In these cases, either the stacking galaxies do not belong to a single population - namely, they are a mixture of AGN and star-forming galaxies - or the underlying population is truly dominated by composite galaxies.

Using stacked spectra instead of individual spectra leads to some difficulties in estimating the number of SFGs and AGN. If, on one hand, this technique allows one to study the average properties of galaxies in a given mass-redshift bin - providing average spectra for otherwise individually unclassifiable galaxies with too low S/N - on the other hand it does not provide us with the exact number of spectral types. Furthermore, each bin collects a variable number of galaxies, because of filaments (overdensities), voids (underdensities), and selection effects acting at the highest as well as at the lowest stellar masses (Fig. 3.1). Therefore, it is not possible to compare the exact number of AGN between the different bins. Assuming that all galaxies in a given stack have the same classification as the stacked spectrum, we obtain the following statistics. The number of single galaxies that are spectroscopically identified as AGN in the four high-redshift bins (5 568 galaxies in total, see Fig. 3.1) is 1 690 (30.3%), while there are 2 491 composites (44.7%). These numbers are higher than the galaxies placed in the four bins at lower redshift (3 742 galaxies), where we find 395 AGN (10.5%) and 775 composites (20.7%). However, assuming that all galaxies in a given composite or AGN bin are indeed AGNs will very likely result in an overestimate of the true AGN fraction. Nevertheless, the relative difference between the higher and lower redshift bins remains an interesting hint of a greater AGN fraction at earlier epoch. Based on the study of

individual galaxy spectra, Ivezić et al. (71) found a starburst-over-AGN ratio equal to 18 from SDSS data, which is a much higher ratio than found here.

## 4.5 Conclusions

Strong nebular emission lines such as  $H\alpha\lambda 6563 \text{ \AA}$ ,  $H\beta\lambda 4861 \text{ \AA}$  and  $[\text{OII}]\lambda 3727 \text{ \AA}$  are formed in HII regions and are indicators of ongoing star formation, while  $[\text{OIII}]\lambda 5007 \text{ \AA}$ , and  $[\text{NII}]\lambda 6583 \text{ \AA}$ , which are higher ionized, are considered as AGN indicators. The combination of these lines can be used to distinguish between the two main ionizing mechanisms inside galaxies and separate SFGs from AGN (119).

The zCOSMOS 20k catalog was used to create a sample of galaxies with reliable spectroscopic redshift and without broad-line AGN to avoid overshining problems (AGN brighter than the surrounding galaxy) and investigate the evolution of galaxy spectral properties up to  $z \sim 1$ . The sample, containing  $\sim 1.5 \times 10^4$  objects, was divided into 61 bins over the stellar mass-redshift plane. To improve the S/N of the single spectra and allow accurate flux measurements, I combined all spectra in each bin to obtain average stacks. After stacking the spectra, stellar continuum subtraction on the galaxy composites were performed, using templates of stellar population synthesis. This provided new spectra that are almost free from absorption contaminations by stars. Finally, optical emission-line diagnostics were used to search for AGN contamination at the highest stellar masses.

Main findings of this work are:

- Galaxy stellar populations are older (in terms of time from the last burst of star formation) in more massive objects. This agrees with an evolutionary scenario that accounts for a fast mass assembling and stellar population aging for massive objects.
- Galaxy-stacked spectra are more likely to be classified as AGN than star-forming galaxies for high values of their total stellar mass. In particular, galaxies with  $\log M_*/M_\odot > 10.2$  start to be classified as composite objects (where both photoionization by stars and nuclear activity contribute to produce the emission lines). They are placed in the AGN region of the diagnostic diagrams for the highest masses considered in the sample.

#### 4. STELLAR MASS-AGN RELATION IN INTERMEDIATE REDSHIFT GALAXIES

---

- At fixed redshift, the classification of the stacked spectra displays a trend with increasing stellar mass. The general trend follows the left branch of the SDSS classification to the bulk of the star-forming galaxy population. At the highest stellar masses, the tracks fall in the composite and then in the AGN region. This is visible in the [NII]-based and in the MEx diagram, whereas it is not well observed in the [OII]-based diagram.
- The MEx diagram represents a useful tool for investigating the ionizing mechanisms inside galaxies, especially at high redshift. The Lamareille [OII]-based diagram is not as effective because of the ambiguity between star-forming, composites, and Seyfert 2 galaxies in some regions of the diagram (107). Moreover, it is necessary to be in a specific redshift interval to measure all involved emission lines. The confusion that this diagram shows can be due to its higher sensitivity to shocks than to AGN photoionization.
- While there is no clear trend with redshift on the low-redshift BPT diagram, there is a trend on the MEx diagram when combining the low- and high-redshift bins. The high-redshift stacks display clearly more composite- and AGN-like spectra. However, the explanation of this trend (higher AGN-detection rate at higher redshift) may include true evolutionary effects as well as selection biases.
- The link between stellar population age and galaxy stellar mass, combined with the increasing AGN-detection rate for increasing mass and redshift, is consistent with a scenario where AGN could act to quench the star formation and then contribute to the transformation from young blue late-type galaxies to old red early-type galaxies.

## 5

# Radio emitters and their optical counterparts

### 5.1 Introduction

Several authors have found strong correlations between the fraction of detected Active Galactic Nuclei (AGNs) at different wavelengths and optical properties such as flux, color, and emission-line strength (147). AGNs can be selected from an optical spectroscopic survey using optical emission line ratios. Emission-line diagnostic diagrams have been extensively used during the past decades to point out the connection between the galaxy nuclear activity, its morphological type (117), and its evolutionary stage (48). The Baldwin-Phillips-Terlevich (BPT) diagnostic diagram (23) and its subsequent versions (24, 94, 106, 136, 148, 149) make use of emission line ratios whose strength is a function of the hardness of the ionizing field of the galaxy, the ionization parameter  $U$ , and the metallicity. Higher ratios are thought to mainly be the product of the ionization that arises due to accretion around the black hole - which implies there is an AGN at the center of the galaxy - rather than photoionization by hot massive OB stars. This diagnostic technique, largely used in the optical wavelength regime, allows differentiation of galaxies that show activity in their nuclei, and starbursts.

Spectra from the Sloan Digital Sky Survey (SDSS) - the largest optical galaxy survey - have been used to compute the line strength of several emission lines to classify galaxies into starbursts and AGNs by using diagnostic diagrams. Radio emission can also be considered to be strong AGN signature. Some attempts to link optical and radio prop-

## 5. RADIO EMITTERS AND THEIR OPTICAL COUNTERPARTS

---

erties of a large sample of galaxies by using combined spectroscopic and photometric information have been already made in the past. For example, Ivezić et al. (71) discuss the optical and radio properties of  $\sim 30\,000$  FIRST (97) radio sources, positionally associated with SDSS sources, by analyzing their colors. The authors find that the number of radio galaxies classified as AGNs rather than starbursts is six times more than the corresponding number for all the SDSS galaxies, and  $\sim 30\%$  of the total. Furthermore, the radio emission from AGNs turns out to be more concentrated than the radio emission from starburst galaxies, as we expect from the nuclear origin of AGN emission. Radio emission is point-like in compact quasars detected at high redshift, while local galaxies tend to have larger radio sizes. This suggests that a significant amount of the radio emission either originates outside the nuclear region or that the radio lobes are resolved. Depending on the beam size, it can happen that not all the light from the galaxy is taken into account. The relative number of AGNs decreases with the radio flux, and this is consistent with the differences in the radio luminosity functions of starburst and AGNs (150, 151). Best et al. (109) compare the optical SDSS survey to both FIRST and NVSS radio surveys, in order to derive the local radio luminosity functions of radio-loud AGNs and star-forming galaxies. We should, however, bear in mind that cross-match might lead to data loss, i.e. the exclusion of some galaxies from the optical-radio cross-matched sample. In the SDSS Early Data Release (71),  $\sim 70\%$  of FIRST sources do not have an optical counterpart within  $3''$ . This is probably because the majority of unmatched FIRST sources, detected down to  $1\text{ mJy}$  sensitivity, are too optically faint to be detected in the SDSS images. Moreover, the fraction of quasars in the FIRST catalog seem to be a strong function of the radio flux, monotonically decreasing from bright radio sources towards the FIRST radio sensitivity limit.

This study is meant to bridge the lack of extended studies on AGN hosts at combined optical and radio wavelengths. Literature data offers the chance to build on a very large galaxy sample, and investigate the multi-wavelength properties of AGNs and normal galaxies. Here I make use of both optical - for the part concerning emission lines and diagnostic diagrams - and radio data to conduct a statistical study. The prospect is to identify radio galaxies in some well-defined regions of the low-ionization emission lines diagnostic diagrams, by using a combination of radio and optical properties. A comparison of the spectroscopic measurements with some photoionization and shock

models is then presented to shed light on the origin of the emission lines in AGNs and star-forming galaxies.

## 5.2 Analysis

A statistical study of the spectral properties of radio emitters from the SDSS has been carried out, starting from the determination of the fraction of star-forming galaxies and AGNs composing the sample (see Chapter 3 for details on sample selection and completeness). For this purpose, I exploited the emission-line diagnostic diagrams to separate sources with a hard ionized spectrum (AGNs) and those that are dominated by star formation, characterized by a considerably softer ionizing field. Since all the emission lines that are used in the diagrams are placed close to each other in the spectrum, their ratios are almost insensitive to reddening, so there is no need to correct for the interstellar and galactic extinction. The luminosity of the  $H\alpha$  line has been derived after correcting the corresponding flux for the visual extinction, by using a theoretical  $H\alpha/H\beta$  Balmer ratio of 2.86 (12).

### 5.2.1 Diagnostics of the SDSS and the cross-matched samples

Figure 5.1 presents the optical emission-line diagnostic diagrams for the MPA-JHU (Data Release 7 of SDSS measurements) and the cross-matched optical-radio samples. In all the diagrams, 79 235 of the 79 919 (99.1%) galaxies in the MPA-JHU high S/N sample (see Sect. 3.4.1) are represented, and 9 408 of the 9 594 radio emitters (98.1% of the optical-radio sample). The difference comes from the lack of some emission-line measurements in the parent catalog of SDSS galaxies and especially the [O $\text{I}$ ] line, which is weaker than the other lines. The dashed demarcation curve in the panels in the first column of Fig. 5.1 ([N $\text{II}$ ]-based or BPT diagram) has been derived by Kewley et al. (25), by constructing a detailed continuous starburst model with broad realistic metallicity and ionization parameter ranges. This was done to find an upper limit for the position of the star-forming galaxies in the diagram. The upper limit can be used to separate AGNs from star-forming galaxies. The dot-dashed curve has been derived by Kauffmann et al. (4), who propose an empirical and more conservative cut to identify starbursts by using the large sample of emission line galaxies in the SDSS.

## 5. RADIO EMITTERS AND THEIR OPTICAL COUNTERPARTS

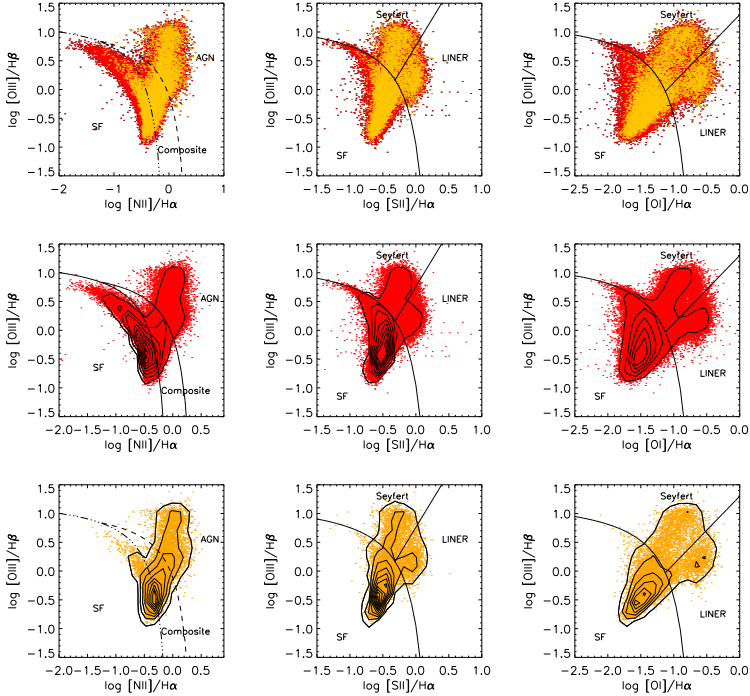


**Figure 5.1:** Radio emitters classified according to optical emission-line diagnostic diagrams. SDSS (DR7) targets are represented in red, while the radio emitters from the cross-matched sample are plotted in orange. Demarcation curves in the left panels ([NII]-based diagram) are by Kewley et al. (25) (dashed) and Kauffmann et al. (4) (dot-dashed); in the middle ([SII]-based diagram) and right ([OI]-based diagram) panels, the demarcation curves are by Kewley et al. (26). The top panels show the SDSS targets superimposed with the radio emitters. The middle and bottom panels show density contours of SDSS and radio emitters, respectively. Density levels represent 800 galaxies per contour in case of SDSS targets, while it is 80 for the radio emitters.

Diagram	Spectral type	SDSS DR7	Cross-match
[NII]	AGNs	11 756±108 (14.8%)	2 968±54 (31.5%)
	Composites	13 856±118 (17.5%)	3 021±55 (32.1%)
	SFGs	53 623±232 (67.7%)	3 419±58 (36.3%)
[SII]	Seyferts	7 646±87 (9.6%)	1 747±42 (18.6%)
	LINERs	4 107±64 (5.2%)	1 012±32 (10.8%)
	SFGs	67 482±260 (85.2%)	6 649±81 (70.7%)
[OI]	Seyferts	10 269±101 (13.0%)	2 180±47 (23.2%)
	LINERs	6 543±81 (8.3%)	1 500±39 (15.9%)
	SFGs	62 423±250 (78.8%)	5 728±76 (60.9%)

**Table 5.1:** Statistics on the SDSS DR7 sample and the cross-matched optical-radio sample, including the number of different objects placed in the AGN, composite, and SF region (left panels, Fig.5.1), or Seyfert, LINER, and SF region (middle and right panels) of the diagnostic diagrams. The relative fraction of different spectral types is reported in parenthesis.

This method selects many fewer star-forming galaxies than AGNs - according to the main ionizing mechanism that produces the emission lines - compared to the Kewley’s criteria. The enclosed region between the two curves is considered to be populated by mixed or transitional objects. In the middle ([SII]-based diagram) and right ([OI]-based diagram) panels, the demarcation curves are from Kewley et al. (26). Another line allows us to separate Seyfert galaxies from LINERs (28).

In Table 5.1 I present the statistics on the samples. For each diagnostic diagram, I report the number of AGNs (with the distinction between Seyferts and LINERs, when available), composites, and star-forming galaxies for both samples. The absolute number of objects per region is followed by the purely statistical error (Poisson error estimated as  $\sqrt{N}$ ) and the percentage with respect to the total number of galaxies with measured emission-lines. A higher relative number of radio emitters are placed in the transitional or AGN regions than in the full optical sample, and the percentage of radio emitters in the left arm of the “seagull” shape defined by the SDSS targets in the [NII]-based diagram is lower. The SDSS is strongly dominated by star formation rather than AGN-like emission. In figure 5.1, the bottom panels show that the radio galaxies with AGNs are drawn from a population that has higher metallicity than the overall SDSS sample. The lower-metallicity objects are predominantly star-forming,

## 5. RADIO EMITTERS AND THEIR OPTICAL COUNTERPARTS

---

and populate the upper left-hand portions of these diagrams. The [O<sub>I</sub>]-based diagram is the one that shows the largest number of objects classified as AGNs (39.1% of the cross-matched sample).

We should take into account that the redshifts considered in this study is limited because of reliance on the diagnostic diagrams, requiring [NII] and H $\alpha$  in the observable spectral window. Some of the emission lines are shifted out of the SDSS spectral range for objects with  $z \gtrsim 0.4$  ( $\sim 2\%$  of the optical-radio sample). However, with this set of diagrams one is able to easily compare results with the studies that have been already conducted using SDSS data.

### 5.2.2 Trend with $L_{20\text{cm}}/L_{\text{H}\alpha}$

The luminosity of the H $\alpha$  line,  $L_{\text{H}\alpha}$ , is considered to be a good optical star formation rate (SFR) indicator (152). The ratio between the radio luminosity and  $L_{\text{H}\alpha}$  can be used to compare emission from radio components with the emission from young stars. I divided the cross-matched optical-radio sample into four bins with increasing  $L_{20\text{cm}}/L_{\text{H}\alpha}$ , containing approximately 2350 galaxies each, to keep the number of objects per bin constant. I search for a threshold above which the objects start to be classified as AGNs (Seyfert or LINERs) rather than star-forming galaxies.

I would expect to find a correlation between the optical and the radio emission, according to the hypothesis that they are linked to each other (e.g.  $L_{20\text{cm}} - L_o$  relation, where  $L_o$  is the luminosity at optical wavelengths) because they arise from the same physical process.

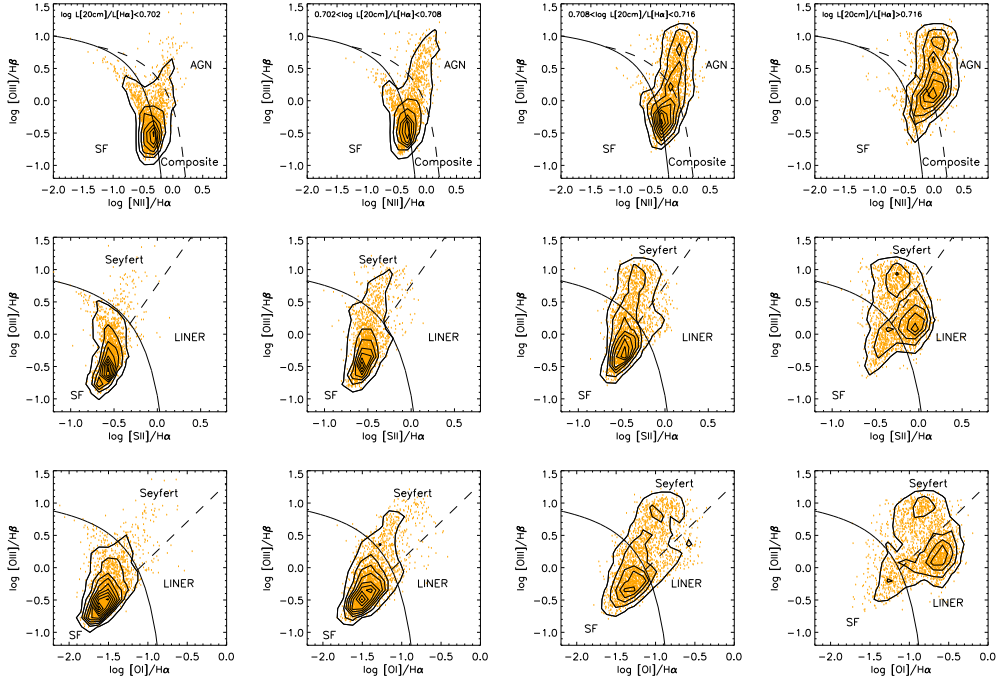


**Figure 5.2:** [NII]- (top), [SII]- (middle), and [OII]-based (bottom) diagnostic diagrams for the optical-radio sample. From left to right,  $\log(L_{20\text{cm}}/L_{\text{H}\alpha})$  increases. The number of radio emitters per bin is constant and equal to  $2350 \pm 25$ . The contours represent the number density of the radio emitters (20 galaxies per density contour, and 40 in the first two panels of the middle and bottom rows).

## 5. RADIO EMITTERS AND THEIR OPTICAL COUNTERPARTS

---

Strong emission lines, such as [OIII], [OII], and H $\beta$ , are indeed believed to come from powerful radio emitters (56, 153, 154, 155, 156, 157, 158). These lines are also used to select AGNs from a spectroscopic survey, pointing to a possible correlation between the AGN-detection rate and the radio luminosity of the host galaxies.

The following results show that the peak of the distribution of the radio emitters shifts from the SF region of the diagrams to the composite or AGN part (on the right-hand side of the diagrams) for increasing  $\log(L_{20\text{cm}}/L_{\text{H}\alpha})$  (Fig. 5.2). In particular, the left-hand panels mostly show starbursts with high metallicity, while the middle panels display a mixed population and the right-hand panels show a nearly pure AGN population, together with some metal-rich starbursts. The distribution shows a peak in the LINER region for  $\log(L_{20\text{cm}}/L_{\text{H}\alpha}) > 0.716$ , where 50% of the radio emitters are classified as LINERs in the [OI]-based diagram (36.2% in the [SII]-based diagram, see Table 5.2).

In the two middle panels ( $0.702 < \log L_{20\text{cm}}/L_{\text{H}\alpha} < 0.708$  and  $0.708 < \log L_{20\text{cm}}/L_{\text{H}\alpha} < 0.716$ ) of each row, the Seyfert region appears increasingly more populated (from a few per cent up to more than 30%), while the number of Seyfert galaxies seems to remain constant for  $\log(L_{20\text{cm}}/L_{\text{H}\alpha}) > 0.716$ . In contrast, the increase in the number of LINERs is exponential in the last bin, where it goes from the few per cent of the first three bins to half of the entire population of radio emitters in the last bin. All diagrams exhibit this behavior, though the trend is most obvious in the [OI]-based diagram, which is also the most sensitive to shocks. In Table 5.2 and Fig. 5.4, I report the statistics on the  $L_{20\text{cm}}/L_{\text{H}\alpha}$  bins on all the diagnostic diagrams. The number of Seyfert galaxies and AGNs in the BPT diagram increases progressively by a factor 2.7 in the first three bins, while it remains almost constant in the last bin. The number of LINERs drastically increases ( $\times 5$ ) from the third to the last bin, while the number of SFGs decreases in the last bin. For each diagnostic diagram I indicate the number of classified star-forming galaxies, Seyferts, and LINERs (or composites and AGNs in the [NII]-based diagram) per  $L_{20\text{cm}}/L_{\text{H}\alpha}$  bin.

Diagram	Spectral Type	$L_{20\text{cm}}/L_{\text{H}\alpha} < 0.702$	$0.702 < L_{20\text{cm}}/L_{\text{H}\alpha} < 0.708$	$0.708 < L_{20\text{cm}}/L_{\text{H}\alpha} < 0.716$	$L_{20\text{cm}}/L_{\text{H}\alpha} > 0.716$
[O <sub>I</sub> ]	Seyferts	126±11 (5.4%)	347±19 (14.5%)	859±29 (36.5%)	848±29 (36.5%)
	LINERs	20±5 (0.8%)	64±8 (2.7%)	254±16 (10.8%)	1 162±34 (50.0%)
	SFGs	2 199±47 (93.8%)	1 973±44 (82.8%)	1 241±35 (52.7%)	315±18 (13.5%)
[S <sub>II</sub> ]	Seyferts	88±9 (3.7%)	261±16 (10.9%)	676±26 (28.7%)	722±27 (31.0%)
	LINERs	10±3 (0.4%)	24±5 (1.0%)	136±12 (5.8%)	842±29 (36.2%)
	SFGs	2 247±47 (95.8%)	2 099±46 (88.0%)	1 542±39 (65.5%)	761±28 (32.7%)
[N <sub>II</sub> ]	AGNs	134±12 (5.7%)	346±19 (14.5%)	918±30 (39.0%)	1 570±40 (67.5%)
	Composites	659±26 (28.1%)	820±29 (34.4%)	925±30 (39.3%)	617±25 (26.5%)
	SFGs	1 552±39 (66.2%)	1 218±35 (51.1%)	511±23 (21.7%)	138±12 (5.9%)

**Table 5.2:** Statistics on the  $L_{20\text{cm}}/L_{\text{H}\alpha}$  (in logarithmic value) bins of the optical-radio sample, showing the number of different objects placed in the Seyfert, LINER, and SF region, or AGN, composite, and SF region (Fig. 5.2) of the diagnostic diagrams. The relative fraction of spectral types is reported in parenthesis.

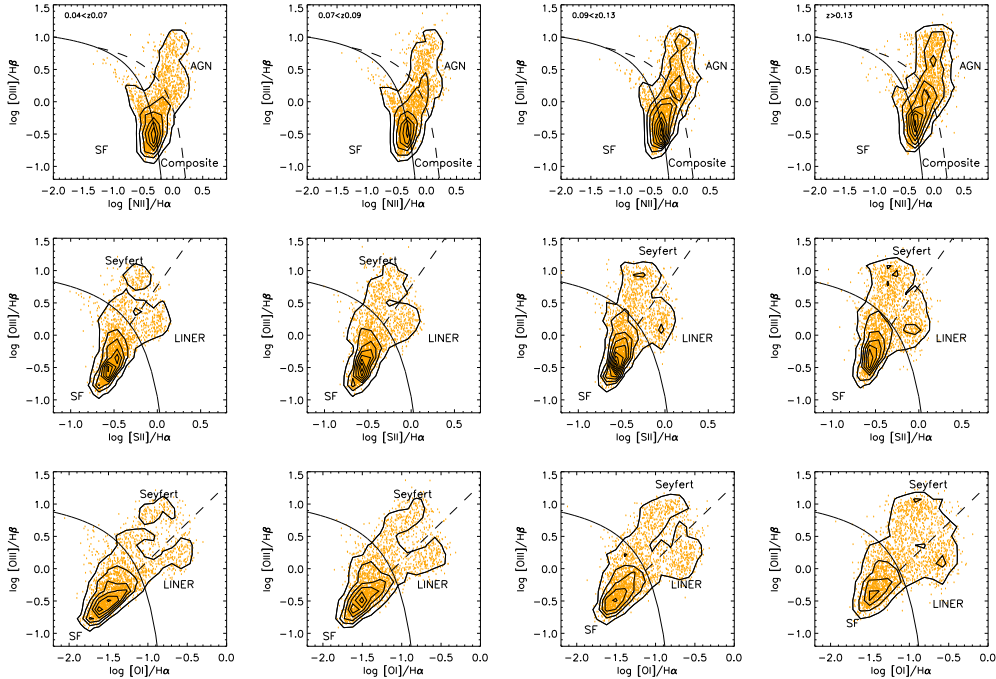


**Figure 5.3:** [NII]- (top), [SII]- (middle), and [OII]-based (bottom) diagnostic diagrams for the optical-radio sample. From left to right,  $z$  increases. The number of radio emitters per bin is constant and equal to  $2\ 350 \pm 5$ . The contours represent the number density of the radio emitters (20 galaxies per level, and 30 in the first two panels of the middle and bottom rows).

Diagram	Spectral type	$0.04 < z < 0.07$	$0.07 < z < 0.09$	$0.09 < z < 0.13$	$z > 0.13$
[O <sub>I</sub> ]	Seyferts	385±20 (16.4%)	461±21 (19.6%)	585±24 (24.9%)	749±27 (31.7%)
	LINERs	288±17 (12.3%)	314±18 (13.3%)	386±20 (16.5%)	512±23 (21.7%)
	SFGs	1 675±41 (71.3%)	1 580±40 (67.1%)	1 374±37 (58.6%)	1 099±33 (46.6%)
[S <sub>II</sub> ]	Seyferts	308±17 (13.1%)	364±19 (15.5%)	465±22 (19.8%)	610±25 (25.8%)
	LINERs	213±15 (9.1%)	211±14 (9.0%)	261±16 (11.1%)	327±18 (13.8%)
	SFGs	1 827±43 (77.8%)	1 780±42 (75.6%)	1 619±40 (69.0%)	1 423±38 (60.3%)
[N <sub>II</sub> ]	AGNs	553±23 (23.5%)	620±25 (26.3%)	790±28 (33.7%)	1 005±32 (42.6%)
	Composites	758±27 (32.3%)	744±27 (31.6%)	740±27 (31.6%)	779±28 (33.0%)
	SFGs	1 037±32 (44.2%)	991±31 (42.1%)	815±28 (34.7%)	576±24 (24.4%)

**Table 5.3:** Statistics on the  $z$  bins of the optical-radio sample showing the number of different objects placed in the Seyfert, LINER, and SF region, or AGN, composite, and SF region (Fig. 5.3) of the diagnostic diagrams. The relative fraction of spectral types is reported in parenthesis.

## 5. RADIO EMITTERS AND THEIR OPTICAL COUNTERPARTS

---

### 5.2.3 Trend with redshift

The diagnostic diagrams are further exploited as a function of redshift by dividing the sample into four bins, containing approximately 2 350 objects each. As for the  $L_{20\text{cm}}/L_{\text{H}\alpha}$  bins, this choice comes from the intent to keep the number of objects per bin constant, together with the intention to further explore the dependence of the optical classification with redshift.

The results show that the distribution of the radio emitters in the diagnostic diagrams depends slightly on the redshift (Fig. 5.3). The number of AGNs (both LINERs and Seyferts) always increases with  $z$ . The bulk of the population remains in the SF, composite or SF+composite region in all  $z$  bins (see statistics on Table 5.3 and Fig. 5.4). The number of Seyferts, LINERs and AGNs in the BPT diagram is nearly double in the last bin with respect to the first one. The number of composites remains almost constant, while the number of SFGs decreases of a variable percentage (22% in the [SII]-based diagram, 34% in the [OI]-based diagram and 45% in the [NII]-based diagram).

### 5.2.4 The WHAN diagram

Emission from some of the galaxies classified as LINERs in the diagnostic diagrams is nowadays thought to be triggered by post-asymptotic giant branch (post-AGB) and white dwarf stars, which are abundant in early-type galaxies. The radiation from old stellar populations in these galaxies, classified as “retired” (RGs, 99), is harder than the radiation produced by young stars, providing higher emission-line ratios than those typical of star-forming regions. Because of the tight correlation between metallicity,  $Z$ , and ionization parameter,  $U$ ,  $[\text{NII}]/\text{H}\alpha$  can be used as an empirical measure of the gas metallicity up to  $[\text{NII}]/\text{H}\alpha = 0.4$ , where higher values become an indication of the presence of AGN activity (103, 135, 159). On the other hand, the  $\text{H}\alpha$  equivalent width,  $\text{EW}(\text{H}\alpha)$ , is considered as a powerful star formation indicator, although it is also related to strong non thermal excitation (e.g. the one from Seyferts). Therefore, the  $[\text{NII}]/\text{H}\alpha$  line ratio and  $\text{EW}(\text{H}\alpha)$  can be combined in a diagnostic diagram (WHAN, 100).

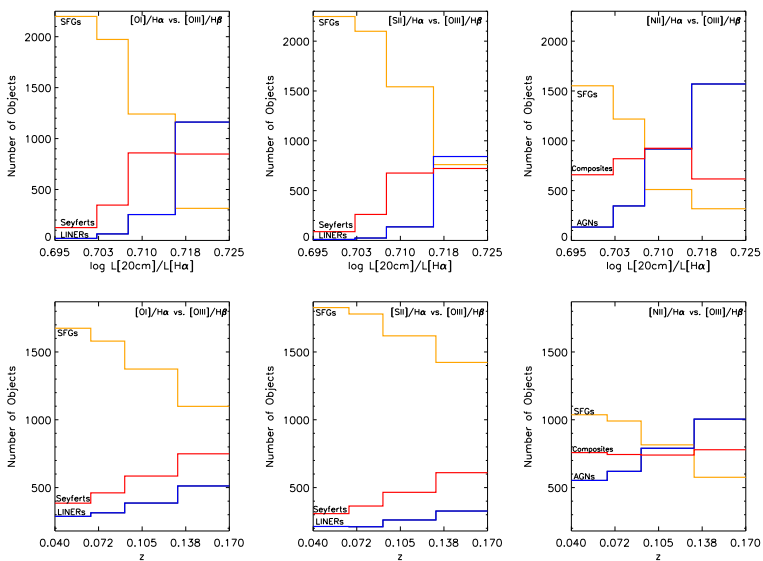


**Figure 5.4:** Histograms of the luminosity and redshift distributions. Top panels: Number of identified spectral types in the  $L_{20\text{cm}}/L_{\text{H}\alpha}$  bins per each diagnostic diagram. Star-forming galaxies are in orange, Seyferts in red, and LINERs in blue (composites in red and AGN in blue in the right panel). The  $L_{20\text{cm}}/L_{\text{H}\alpha}$  value is indicated on the x-axis. Bottom panels: Number of identified spectral types in the  $z$  bins for each diagnostic diagram. The redshift is indicated on the x-axis.

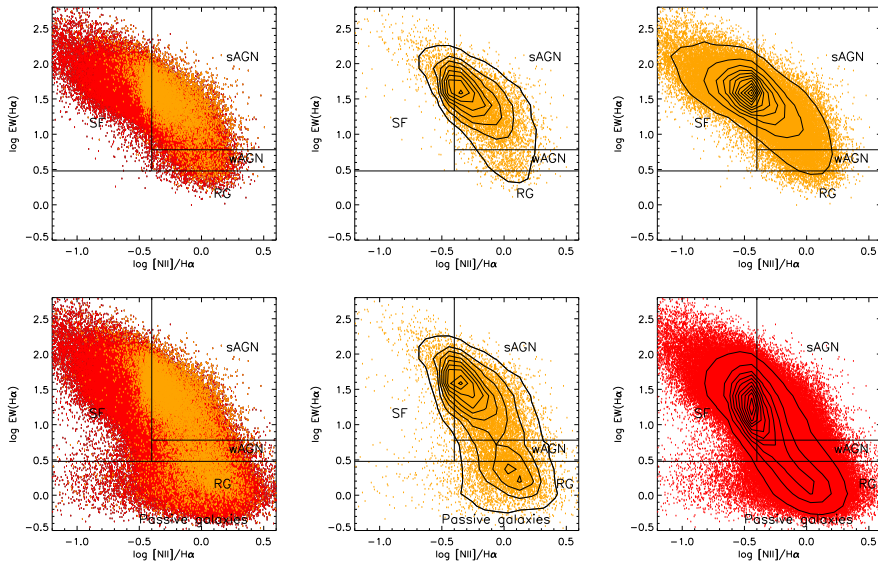


**Figure 5.5:** WHAN diagnostic diagrams of the cross-matched optical-radio (orange) and the SDSS (red) samples. The upper-left panel shows the radio emitters of the SDSS superimposed on the SDSS parent sample. The upper-middle and upper-right panels show density contours of the optical-radio and SDSS samples, respectively. The lower panels represent samples where a less severe error cut (only on  $[\text{NII}]$  and  $\text{H}\alpha$ ) has been applied. In this way, a considerable number of objects have been recovered, which appear to be classified as wAGNs or RGs. Density levels represent 70 galaxies per contour in both middle panels, 500 galaxies per contour in the upper-right panel and 2 000 galaxies per contour in the bottom-right panel.

---

The WHAN diagram can distinguish between retired galaxies and true AGNs, besides having the advantage of being able to classify galaxies with weak [OIII] and/or  $H\beta$  lines. With this diagram it has been found that a large number of weak-line emitting galaxies in the SDSS have LINER-like emission with  $3 < EW(H\alpha) < 6 \text{ \AA}$  in the case of actual LINERs (labeled in the diagram as wAGN, where “w” stands for “weak”) and  $EW(H\alpha) < 3 \text{ \AA}$  for retired galaxies (101). Galaxies that have both high values of  $EW(H\alpha)$  and  $[NII]/H\alpha$  are classified as strong AGNs (sAGNs).

In Fig. 5.5, I show the WHAN diagram for the cross-matched optical-radio sample and for the SDSS parent sample. Radio emitters and optical parent population (upper panels) exhibit a different distribution, with the former having the peak of the distribution in the sAGN region, but close to the demarcation line that separates it from the star-forming galaxies. In the SF region, the number density drops and the contours show a very steep gradient. The majority of galaxies showing LINER-like emission in the classical diagnostic diagrams are found to be true LINERs rather than retired galaxies, because they are mostly placed in the wAGN zone. On the other hand, in the upper right-hand panel the optical distribution appears to be spread more across the SF region, with relatively fewer true AGNs (both strong and weak) and retired galaxies.

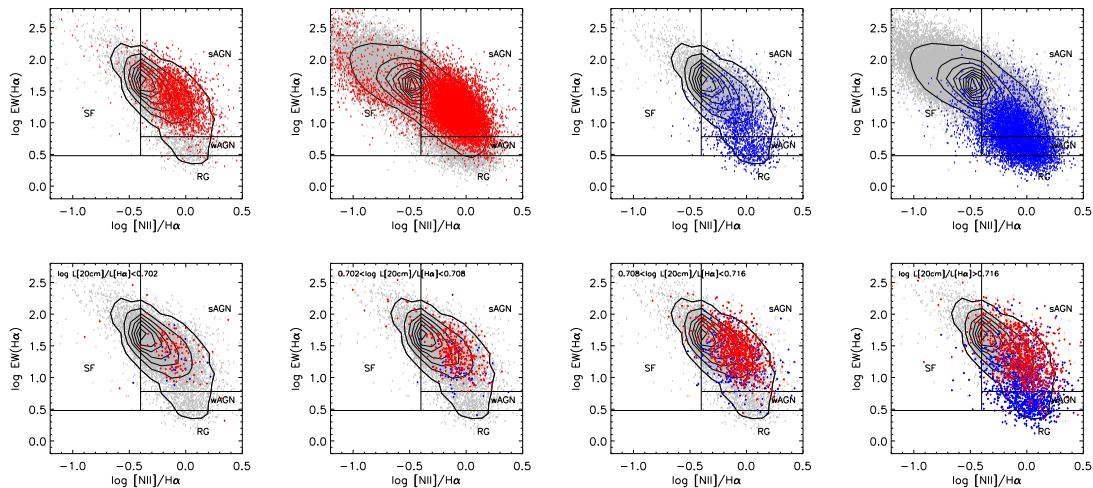


**Figure 5.6:** Upper panels: WHAN diagnostic diagrams for the cross-matched (first and third panels) and the SDSS samples (second and fourth panels) superimposed with AGNs selected from the [OII]-based diagram. Seyferts are in red and LINERs in blue. Contours number density refers to the underlying distribution of each plot and is equal to 70 galaxies per contour in case of cross-matched sample and to 700 galaxies per contour in case of SDSS sample. Bottom panels: WHAN diagnostic diagrams for the cross-matched sample (gray) superimposed with Seyferts (red) and LINERs (blue) selected from the [OII]-based diagram. Each plot represents, from left to right, a different  $L_{20\text{cm}}/L_{\text{H}\alpha}$  bin (Fig. 5.2). Contours number density refers to the underlying distribution of each plot and is equal to 70 galaxies per contour.

The lower panels represent samples where a different error cut (30% on the [NII] and H $\alpha$  lines only) has been applied. In this way, a considerable number (12 419 from the cross-match, 398 272 for the SDSS sample) of objects with weak [OIII], [OI], and H $\beta$  lines have been recovered. They appear to be mostly classified as wAGNs or RGs (as shown by the density contours). Though I miss many passive galaxies in the lower part of the upper WHAN diagrams, I found that the shape of the upper part of the distributions is almost preserved for both the radio emitters and the SDSS targets. The comparison with the lower panels suggests, as already mentioned in Sect. 2.3, that the galaxy classification is strongly influenced by the error cut applied to the samples.

Figure 5.6 (upper panels) shows the WHAN diagnostic diagrams for the cross-matched and the SDSS samples superimposed with AGNs selected from the [OI]-based diagram. I chose the latter as the one diagram that can classify the most Seyferts and LINERs (see Table 5.2). The Seyferts distributions peak in the sAGN region of the WHAN diagram, with only few galaxies falling in the SF or wAGN regions. Moreover, it appears that most of the Seyferts do not lie close to the demarcation curve between SF and sAGN. The LINERs distributions look much more spread across the sAGN region instead, while they are supposed to be confined in the wAGN (in the case of true LINERs) or in the RG region (in case of fake LINERs). Some LINERs appear in the SF region as well. Interestingly, the latter are found to have low [OIII]/H $\beta$ , while the LINERs that fall in the RG region of the diagram have an average higher [OIII]/H $\beta$ . Figure 5.6 (lower panels) shows WHAN diagnostic diagrams for only the cross-matched sample, overplotted with Seyferts and LINERs selected from the [OI]-based diagram. Each plot represents a different  $L_{20\text{cm}}/L_{\text{H}\alpha}$  bin (as in Fig. 5.2). While the distribution of Seyferts always peaks in the sAGN region and only the number of sources increases, LINERs are mostly present in the sAGN region in the first three bins, and they appear to be mostly located in the wAGN region only in the very last  $L_{20\text{cm}}/L_{\text{H}\alpha}$  bin. The radio strong (large  $L_{20\text{cm}}/L_{\text{H}\alpha}$ ) sources deviate from the RG and passive regions, so we can say that the radio-selection helps in removing RGs from the sample. This leads to a cleaner pure AGN sample whose LINERs may well be dominated by shocks.

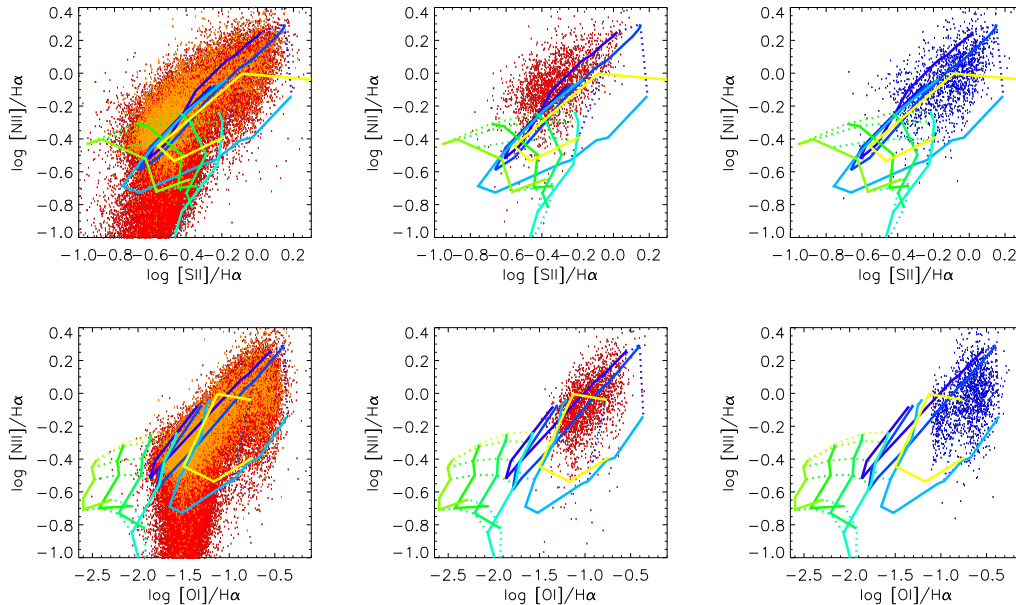


**Figure 5.7:** Data comparison with models. Galaxies from the SDSS sample are in red, while the optical-radio sample is orange (left panels). In the middle panels, Seyferts of the optical-radio sample selected via [OII]-based diagram are in red. In the right panels, LINERs selected with the same diagram are in blue. All models have  $Z = 2 Z_{\odot}$ . The star formation models (160) are represented by green lines; the dusty AGN models (148) are in yellow; the models for shocks without precursors (161) are in blue.

### 5.2.5 Comparison with models

By exploiting optical emission-line diagnostic diagrams, both classical and WHAN, I have stressed the higher concentration of LINERs with increasing  $L_{20\text{cm}}/L_{\text{H}\alpha}$ . The point whether LINERs are pure AGNs - i.e. the main ionizing mechanism in the host galaxy is accretion onto the super-massive black hole - is still a matter of debate. There are several processes that could account for LINER emission: photoionization by a non stellar source such as an AGN accreting at a low rate (148, 162, 163) and ionization by fast large-scale shocks (164) produced either by AGN radio jets, galactic super-winds (165, 166, 167), or starburst-driven super winds (168). It has also been found that hot post-asymptotic giant branch (post-AGB) stars and white dwarfs can be responsible for the LINER-like emission in a considerable fraction of galaxies (169).

To further explore this topic, I decided to investigate the physical mechanisms from which the observed optical emission-lines are developing. According to Dopita & Evans (1986), the emission lines in the spectrum of individual HII regions are determined by three main physical parameters, namely the temperature of the stars,  $T$ , and thus their age, the metallicity, and the ionization parameter,  $U$  (usually defined as the ratio of the mean ionizing photon flux to the mean atom density). Using available photoionization and shocks models that can account for the line emission (148, 160, 161), it is possible to unveil the dominant physical processes taking place in the galactic nuclei and their vicinity. For this purpose, I used the  $[\text{SII}]/\text{H}\alpha$  vs.  $[\text{NII}]/\text{H}\alpha$  and  $[\text{OI}]/\text{H}\alpha$  vs.  $[\text{NII}]/\text{H}\alpha$  diagrams. This choice has been made by considering that these emission line ratios do not depend strongly on the age of the stellar population (103, 170, 171).

The left-hand panels in Fig. 5.7 show the models compared to the optical sample and the cross-matched optical-radio sample. I found that the position of most objects can be explained by models with  $Z = 2 Z_{\odot}$ . Solid lines represent different  $\log U$  values, ranging from 0 to  $-6$ . Dashed lines indicate various ages, from 0.5 Myrs to 3.0 Myrs (160).

Models that account for AGN emission, parametrized by a smooth and featureless power law or broken power law (12, 172, 173, 174, 175, 176), are mainly characterized by the ionization parameter. Dust is related to the ionization parameter by the amount of ionizing photons that can be scattered. It is thought to be a fundamental component of AGN tori, and there is also evidence of dust in the narrow-line region (NLR) (177, 178).

## 5. RADIO EMITTERS AND THEIR OPTICAL COUNTERPARTS

---

The dusty AGN model from Groves et al. (148), represented in yellow in Fig. 5.7, considers a ionization parameter ranging from  $10^0$  to  $10^{-4}$ , and spectral index  $\alpha = -2.0$ . The models for shocks without precursors are from Allen et al. (161). The authors consider only fast shocks, where the ionizing radiation generated by the hot gas behind the shock front creates a strong photoionizing radiation field (8, 164, 179). The flux of the ionizing radiation emitted by the shock, hence the ionization parameter, increases with the velocity of the shock front ( $\propto v^3$ ). The magnetic fields in the gas behind the shock front act to limit the compression through the shock itself. This effect is treated with the introduction of the magnetic parameter ( $B/n_e^{1/2}$ ), where the electron density ( $n_e$ ) is equal to  $1 \text{ cm}^{-3}$ . The different values of the magnetic parameter range from  $B/n_e^{1/2} = 0$  to  $4 \mu G \text{ cm}^{3/2}$ . Velocities go from  $100 \text{ km s}^{-1}$  to  $300 \text{ km s}^{-1}$ .

From the first row of plots in Fig. 5.7 ([SII]/H $\alpha$  vs. [NII]/H $\alpha$  diagrams), it appears that I am only partially tracing the star formation in the cross-matched sample, since the left-hand side of the diagrams, where the lines indicating photoionization by hot massive stars are located, does not represent all the radio emitters. The star-forming region is indeed mostly populated by sources that do not have strong detected radio emission, so the models by Dopita et al. (160) represent the SDSS parent sample better. The higher emission-line ratios of the rest of the radio emitters could be explained by shocks and dusty AGNs models. The lines that extend from the central part of the diagram to the upper right corner represent the full length of the distribution quite well. In the upper-middle and upper-right panels of Fig. 5.7, the Seyferts and the LINERs of the cross-matched optical-radio sample selected by the [OI]-based diagram are represented. The emission-line ratios of the Seyferts cannot be fully explained by the models for shocks and dusty-AGNs that we considered in this work. On the other hand, LINERs are mostly placed in the region of the diagram that is enclosed by the sequences for fast shocks and dusty-AGNs, with only a few sources lying in the region explained by photoionization by young hot stars. The latter are found to have a rather low [OIII]/H $\beta$  ratio. In general, LINERs shift to the upper left-hand corner of the diagram for increasing [OIII]/H $\beta$ . However, many galaxies of different spectral type are not explained by these models. The second row of Fig. 5.7 ([OI]/H $\alpha$  vs. [NII]/H $\alpha$  diagrams) shows that neither the cross-matched nor the optical samples are represented well by models for photoionization by hot massive stars. The Seyferts and LINERs are

instead confined much better within the fast shocks and dusty AGNs models than in the  $[\text{SII}]/\text{H}\alpha$  vs.  $[\text{NII}]/\text{H}\alpha$  diagram.

## 5.3 Discussion

### 5.3.1 Classical diagnostic diagrams

With a cross-matching of optical (SDSS) and radio (FIRST) data, I obtained a sample of radio emitters with optical counterpart and thus optical spectral information. By using diagnostic diagrams, I am able to separate AGNs from starburst galaxies, studying the dependence of this classification on quantities such as  $L_{20\text{cm}}/L_{\text{H}\alpha}$  or  $z$ .

#### 5.3.1.1 General trend of the full optical and optical-radio samples

In this study of an optical-radio sample of galaxies, I found that a relatively large number of radio emitters tend to be placed in the transitional or AGN region of the diagnostic diagrams (Fig. 5.1, Table 5.1), suggesting a strong connection between the detection of radio emission/features and the AGN activity. The percentage of detected AGNs increases from the  $[\text{SII}]$  (29, 4%) to the  $[\text{NII}]$  (31, 5%) and  $[\text{OI}]$  (39, 1%) diagrams, partly due to the higher sensitivity of  $[\text{OI}]$  to shocks. The MPA-JHU subsample of SDSS galaxies populates a larger area of the SF region instead. The percentage of star-forming galaxies is maximum in the  $[\text{SII}]$  (85, 2%) diagram, and the percentage of pure SFs (without composites) is 67.7% in the  $[\text{NII}]$  diagram and 78.8% in the  $[\text{OI}]$  diagram. This is mainly due to the selection of more starburst galaxies than in the radio-sample, where the star formation can be observed in the optical but not in the radio, below the 1 mJy sensitivity threshold.

The galaxy radio emission seems to be a function of either optical luminosity or redshift (180). The high number of AGNs among the population of radio emitters has already been pointed out by other authors (181) but never extensively investigated with a set of classical and new diagnostic diagrams and by using a large sample of galaxies.

#### 5.3.1.2 Explaining the trend with $L_{20\text{cm}}/L_{\text{H}\alpha}$

The sample was divided into four equally populated bins with different ranges of  $\log L_{20\text{cm}}/L_{\text{H}\alpha}$ . The significant variation in the number of galaxies justifies the bin choice, although I am aware that the errors on the luminosity could affect the distribution of

## 5. RADIO EMITTERS AND THEIR OPTICAL COUNTERPARTS

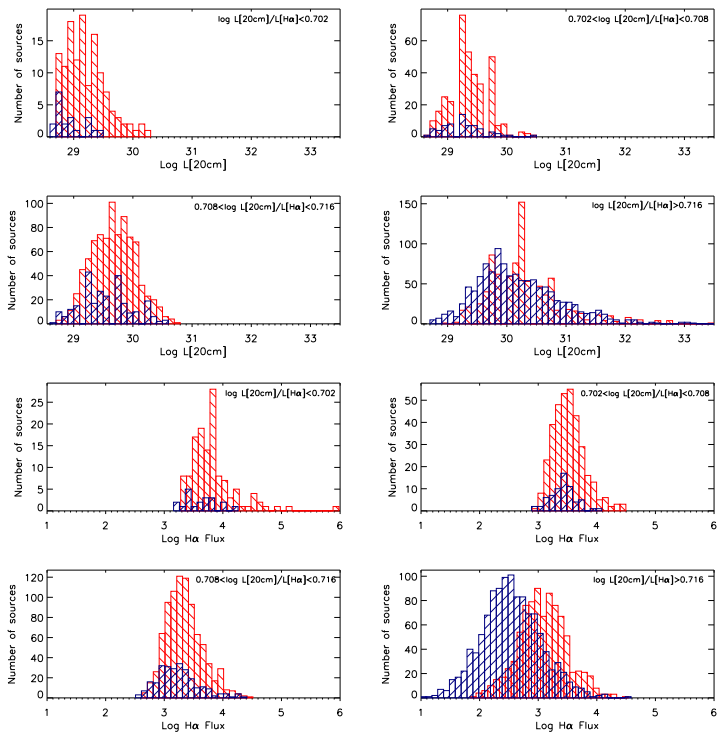


**Figure 5.8:** Histograms of radio luminosity and luminosity of  $H\alpha$  line distributions. First and second rows:  $L_{20\text{cm}}$  distribution for Seyferths (red) and LINERs (blue) in the four  $L_{20\text{cm}}/L_{H\alpha}$  bins. Third and fourth rows:  $H\alpha$  flux distribution.

the sources within the bins. Although we expect different behavior for FRI and FR II, with the latter more abundant in the highest  $L_{20\text{cm}}/L_{\text{H}\alpha}$  bin, where the radio luminosity is higher, it is not possible to prove this with FIRST data alone. Owing to the large beam size of the FIRST radio survey, most of the galaxies are not structurally resolved, thus a distinction between jet-dominated and lobe-dominated emitters is not made.

The optical classification displays a peak in the star-forming or composite region of the diagnostic diagrams for relatively low  $L_{20\text{cm}}/L_{\text{H}\alpha}$  values ( $\log L_{20\text{cm}}/L_{\text{H}\alpha} < 0.716$ ), while the distribution appears to have a peak in the LINER region when above this threshold. In all diagrams there is a progressive shift of the sources towards the AGN region with increasing  $L_{20\text{cm}}/L_{\text{H}\alpha}$ , indicating a change in the galaxy properties (Fig. 5.2). The observed shift in the galaxy distribution, from the SF region of the diagnostic diagrams to the Seyfert region first and LINER region, could eventually be determined by two factors. First, the progressive increase in the radio luminosity peak distribution of about one order of magnitude (from  $\log L_{20\text{cm}} \sim 29.2$  to  $\log L_{20\text{cm}} \sim 30.2$ ) is due to the presence of many AGNs in general, and Seyferts in particular. In this respect, the larger number of AGNs suggests the radio nature of the nuclear and extended emission. Possibly, we are looking at low-luminosity AGNs producing radio-emission. Second, the different  $L_{\text{H}\alpha}$  distribution of Seyferts and LINERs, with the LINERs always peaking for a particular bin at lower  $L_{\text{H}\alpha}$  values with respect to Seyferts, assumes its maximum separation in the last  $L_{20\text{cm}}/L_{\text{H}\alpha}$  bin. Here the  $L_{\text{H}\alpha}$  distribution of LINERs peaks at its lowest value,  $10^{41}$  erg/s, and the  $L_{\text{H}\alpha}$  distribution of Seyferts peaks at its highest value,  $10^{42}$  erg/s), thus the high  $L_{20\text{cm}}/L_{\text{H}\alpha}$  of the last bin is the reason for the appearance of a very large number of LINERs.

In Fig. 5.8 (first and second rows) I show the  $L_{20\text{cm}}$  distribution for Seyferts (red) and LINERs (blue) in the four  $L_{20\text{cm}}/L_{\text{H}\alpha}$  bins. In the first three bins, the distributions span the same range of values. For  $\log(L_{20\text{cm}}/L_{\text{H}\alpha}) > 0.716$ , the distributions nearly overlap. In the third and fourth rows of Fig. 5.8, the  $\text{H}\alpha$  flux distribution is shown. The last bin presents a clear dissimilarity in the distribution of Seyferts and LINERs, where Seyferts peak at higher values. This suggests that the exponential increases in the number of LINERs (Fig. 5.2, most right panels) is probably due to the lower  $L_{\text{H}\alpha}$  values that LINERs present compared to Seyferts.

The [OI]-based diagram (Fig. 5.2, bottom panels) is the one that represents the observed increase in the number of radio emitters in the LINER region best (from 1%

## 5. RADIO EMITTERS AND THEIR OPTICAL COUNTERPARTS

---

to 50%, see Table 5.2) for increasing value of  $L_{20\text{cm}}/L_{\text{H}\alpha}$ . This could be due to the  $[\text{O}I]/\text{H}\alpha$  ratio, which is particularly sensitive to shocks. However, using the diagnostic diagrams might present some problems. It is well established that the activity from the AGN and the star formation inside the host are related, since they depend on the presence of fueling material (4). Galaxies that do not present strong nuclear radio activity could be detected via radio emission arising from supernovae explosions, which can contribute significantly to the emission at low radio levels. In that case, it is likely that these AGNs show up as starbursts (low tale of the radio luminosity distribution) or LINERs (high radio emission) in the classification provided by the diagnostic diagrams.

### 5.3.1.3 Explaining the trend with redshift

It has already been noticed in the past that there are more AGNs at high redshift, and that this could be related to selection effects. At high redshift, we are likely to select powerful emitters such as Seyferts, while LINERs seem to be traced by radio-emission coming from shocks, so they are easier to find at higher radio luminosities. I explored the dependence of the optical galaxy classification on the redshift by dividing our sample of radio emitters into four different redshift bin. The classification appears to slightly depend on the redshift. The number of classified AGNs increases almost by a factor 2 from the first to the fourth redshift bins (Fig. 5.3). This is true for both AGN classes, with a small difference between LINERs (the average factor is equal to 1.65, based on the statistics of the  $[\text{O}I]$ -based and the  $[\text{S}II]$ -based diagrams, Table 5.2) and Seyferts (1.95). This suggests that the AGN detection rate could be biased against the higher number of powerful sources, such as Seyferts, which are detected at higher redshifts. At the same time, it does not exclude AGNs and high redshift being in a genuine relation.

### 5.3.2 Recent diagnostics

The WHAN diagnostic diagram can help shed light on the nature of the emission lines in the LINER-like spectra of galaxies selected with the classical diagnostic diagrams. Figure 5.6 shows that Seyferts (selected by using the traditional  $[\text{O}I]$ -based diagnostic diagram) are mostly placed in the sAGN region and only a few of them are located in the wAGN region. Their number density drops at  $\log [\text{N}II]/\text{H}\alpha \lesssim -0.3$ , before reaching the left boundary with the SF region. LINERs mostly appear in the wAGN region,

but they are spread in the RG and sAGN regions as well. One of the possible reasons for the misclassifications of these objects could be the selection of AGNs from the [O I]-based diagram. A full consistency between the latter and the WHAN diagram cannot be achieved.

Figure 5.6, as well as Fig. 5.2, display how the separation between Seyferts and LINERs becomes more pronounced in the last  $L_{20\text{cm}}/L_{\text{H}\alpha}$  bin, where many LINERs are identified, indicating general agreement between the classification provided by the different diagnostic diagrams.

I found the use of the WHAN diagram complementary to the one of the classical diagnostic diagrams, as the former is the only current optical diagnostic tool that can further distinguish between objects with LINER-like emission. In particular, the radio sources of the radio-optical sample are more likely to be identified as true LINERs (wAGN) than as passive galaxies, suggesting that photoionization by old stars possibly gives only a minor contribution to line emission.

### 5.3.3 Photoionization and shock models for the [S II]/H $\alpha$ vs. [N II]/H $\alpha$ and [O I]/H $\alpha$ vs. [N II]/H $\alpha$ diagrams

The presence of a large number of LINER-classified galaxies in the classical diagnostic diagrams does not imply a high detection rate of central engine-dominated objects. In particular, for radio-selected sources, the observed high fraction of LINERs can be due, for example, to the detection of radio jets, as well as of SNe-driven winds. A large fraction of radio emitters are found to be AGNs (see Table 5.1), thus their emission-line ratios are expected to be at least partially explained by shock and dusty AGN models, and less by star formation. The star-forming region is, indeed, mostly populated by sources that have shallow radio emission. Models of photoionization by hot young stars (103) can nicely explain the star-forming region (left wing of the seagull) in the classical diagnostic diagrams. Regarding the right wing of the distributions, where the AGNs are located, a comparison with photoionization models (99) shows that radiation from old metal-rich stellar populations can explain the emission-line ratios that are typical of LINERs. On the other hand, these models do not work well for Seyfert, which could be explained by other mechanisms producing the observed emission lines.

In Fig. 5.7 ([S II]/H $\alpha$  vs. [N II]/H $\alpha$  diagram, first row), the star formation models by Dopita et al. (160) represent the SDSS parent sample better than the cross-matched

## 5. RADIO EMITTERS AND THEIR OPTICAL COUNTERPARTS

---

radio sample. Although the bulk of the radio emitters are placed in the region of the diagram that is enclosed by the models for star formation, shock and dusty-AGN models could account for most of the cross-matched sources that are found to be AGNs, and LINERs in particular (upper-middle and upper-right panels). However, many radio emitters are placed in regions of the  $[\text{SII}]/\text{H}\alpha$  vs.  $[\text{NII}]/\text{H}\alpha$  diagram that the chosen models cannot predict. This is especially the case for Seyferts. This points to the possibility that these objects have emission-lines that can be explained by multiple mechanisms acting at the same time, e.g. to produce the higher  $[\text{NII}]/\text{H}\alpha$  ratio that no model can predict. The  $[\text{OI}]/\text{H}\alpha$  vs.  $[\text{NII}]/\text{H}\alpha$  diagram (Fig. 5.7, second row) does not show any Seyfert or LINER of the radio-selected sample in the region enclosed by the star formation models, but it shows more clearly that the AGNs (most of the Seyferts and almost all the LINERs) are best represented by shock and dusty AGN models. These diagrams show that, as mentioned before, the radio sources are drawn from a metal-rich population, whether starburst, LINER, or Seyfert-dominated.

However, this is not sufficient to disentangle the complicated “nature of LINER” issue. What we can say is that some LINERs are triggered by mechanisms responsible for shocks, thus they are linked to radio-emission and easily identifiable with increasing  $L_{20\text{cm}}/L_{\text{H}\alpha}$  values. I acknowledge that this evidence is just a step in unveiling the nature of LINERs, so further studies are required to provide a thorough investigation.

### 5.4 Conclusions

Main findings and conclusions follow:

- The requirement of detected radio emission predominantly selects active galaxies, a considerable number of AGNs and metal-rich starburst galaxies, where the radio-emission mainly has a stellar origin. Radio emission correlates with optical emission-line ratios, so a cross-match allows us to classify and study radio emitters according to their optical spectral identification.
- Emission-line diagnostic diagrams show that many radio emitters are classified as AGNs with increasing  $L_{20\text{cm}}/L_{\text{H}\alpha}$ . In particular, the increase in  $L_{20\text{cm}}$  selects powerful radio emitters such as Seyferts, while the decrease in  $L_{\text{H}\alpha}$  strongly contributes to the selection of a considerable fraction of galaxies with LINER-like emission.

- The higher number of identified AGNs with increasing values of factor  $z$  from the first to the fourth redshift bin can indicate a true correlation between these quantities, as well as a bias, related to the selection of the most powerful radio emitters.
- Emission-line diagnostic diagrams are useful tool for classifying sources according to the main ionizing mechanism producing emission lines, though the classification depends on the choice of the chemical species that is used in the diagram. In general, we found good agreement between the classifications given by the classical diagnostic diagrams and the  $[\text{NII}]/\text{H}\alpha$  vs. equivalent width of the  $\text{H}\alpha$  line (WHAN) diagram. Diagnostic diagrams can only give hints on the nature of the observed emission-lines, making a complementary comparison between data and models necessary.
- While the star-forming sequence in the diagnostic diagrams can be successfully fit by photoionization models, the AGN region seems to collect objects whose observed emission lines are due to different processes. Most of the radio emitters of the sample, which are mainly classified as LINERs at high  $L_{20\text{cm}}/L_{\text{H}\alpha}$  values, have emission lines whose ratio can be explained by fast-shock and dusty-AGN models. Shocks, closely linked to the presence of radio emission, can be produced both by stars and AGNs, so that unveiling the nature of LINERs requires a more detailed study.
- By using diagnostic diagrams, it is possible to select populations of LINER-like objects and further distinguish between the “true-AGNs” and the galaxies whose emission is produced by old stars. For this radio-selected sample, LINERs are more like true AGNs than retired galaxies. Resolving the spatial radio structure of these groups of LINER-like objects, as well as Seyferts that are particularly bright in the radio, would help us shed light on the physical mechanisms that are responsible for the observed radio luminosity and optical emission-line ratios.

## **5. RADIO EMITTERS AND THEIR OPTICAL COUNTERPARTS**

---

## 6

# Galaxy evolution across optical emission-line diagnostic diagrams

## 6.1 Introduction

Radio-source spectra can be in general described as power laws ( $S_\nu \propto \nu^\alpha$ , where  $\alpha$  indicates the spectral index). While this approximation is fairly good at meter-wavelength, surveys at cm wavelengths found that spectra can differ from the classical power-law shape, showing flattenings and/or rises to the high frequencies, or humps in the radio regime (see review from De Zotti et al., 1982, and references therein). AGN-powered radio sources are classified in two categories: steep- (with  $\alpha < -0.5$ ) and flat-spectrum ( $\alpha > -0.5$ ). Steep-spectrum sources show extended double-lobed structures, while the flat-spectrum objects are mostly point sources. The shape of the integrated spectra can be considered as the result of different components, each of them being dominated by a physical process responsible for emission in the radio source. For example, the compact nature of flat-spectrum sources points to the synchrotron self-absorption, namely the re-absorption of radiation by the synchrotron electrons caused by the high energy of the synchrotron radiation itself, as the main emission mechanism. Sources that possess an intense magnetic field usually have an enhanced synchrotron emission. However, a source having a steep- or a flat- spectrum depends on its orientation as well. An observer's line of sight close to the jet axis of the source offers a view on the base of the jet. The jet base is compact, Doppler-boosted, which means that the observed flux is magnified by relativistic effects of the jet traveling at  $\sim c$  speed and

## 6. GALAXY EVOLUTION ACROSS OPTICAL EMISSION-LINE DIAGNOSTIC DIAGRAMS

---

shows a flat spectrum. This special class of objects for which it is possible to spot the black hole is addressed as *blazars*. The same objects observed from the side have radio low-frequency emission dominated by the lobes instead, which are *optically thin* and show a steep spectrum. Optical thickness measures the transparency of a medium to radiation, and is defined as the negative natural logarithm of the fraction of light that is not scattered or absorbed on a path. A dusty torus hides the accreting black hole (183). Since the emission of source components peaks at different frequencies (e.g. nuclear emission peaks at higher radio frequencies than the lobes emission), the power law approximation of the spectral shape of a radio source holds only when we consider a limited frequency range. Moreover, at high frequencies the steeping of the spectra by electron energy losses (the “aging” of the radiation), and the transition from the *optically thick* to the optically thin synchrotron regime of compact sources, contribute to the production of complex spectra. The radio emission from star-forming galaxies is mostly due to optically thin synchrotron emission, coming from relativistic electrons interacting with the magnetic field of the galaxy, but a significant contribution comes from the ionized interstellar medium via *free-free emission*, which is produced by free electrons scattering off ions without being captured. At mm wavelengths the radio emission starts to be swamped by thermal dust emission, which causes the spectrum to rise steeply with frequency.

The local luminosity function (LLF) describes the local space density of sources as a function of luminosity. It has been found that radio AGNs dominate the LLF above  $S_{1.4\text{GHz}} \simeq 10$  mJy, where  $S$  is the flux density. At lower values, another population becomes important, namely the nearby galaxies, whose emission is triggered by star formation. A common way to identify the main source of the emission is to use the optical emission-line diagnostic diagrams (see Chapter 1). However, even if a source is classified as AGN in the diagrams, the radio emission may not be of nuclear origin. An important hint of this is the fact that most AGNs (90%) are radio quiet. This statement opens the door to multiple discussions on the validity of radio loudness as an important physical property of galaxies (115), and on the possibility of optical and radio emission to be still related but delayed with respect to each other, or the latter to have a more cyclic character (i.e. can occur many times, at different stages of galaxy evolution). However, radio emission and star formation are correlated (184, 185, 186, 187) because stars are source of radio synchrotron emission (via SNe explosions), dust heating (whose

emission peaks at far-IR frequencies), and UV-optical emission (from hot young stars). Some attempts to study the correlation between AGN activity and evolution of host properties in the radio-optical regime have been already made in the past by using the large SDSS sample combined e.g. with FIRST, or NVSS (71, 73, 109, 147, 181). In Ivezić et al. (71), the radio emission from AGNs turns out to be more concentrated than the radio emission from starburst galaxies, as we expect from the nuclear origin of AGN emission. Radio emission is point-like in compact quasars detected at high redshift, while local galaxies tend to have larger radio sizes. This suggests that a significant amount of the radio emission either originates outside the nuclear region or that the radio lobes are resolved. In Vitale et al. (73), the relative number of AGNs increases with the radio luminosity over the luminosity of the  $H\alpha$  line. In particular, the trend is prominent in case of LINERs. This is consistent with the differences in the radio luminosity functions of starburst and AGNs (151, 188). Best & Heckman (158) used a sample of radio-loud AGN drawn from the SDSS DR7 to study the “high excitation” and the “low excitation” radio galaxies (HERG and LERG, respectively, also indicating the “quasar mode” and the “radio mode” of AGN feedback) and found that HERG are in bluer and younger hosts, accreting at more efficient rates (1 – 10% of Eddington accretion rate), while LERG show a passive evolution and accrete at very low rates (< 1%). The authors speculate that this might be due to mergers or interactions. Moreover, HERG present lower stellar and black hole masses than LERG at same radio luminosities. According to these findings, the two populations of HERG and LERG could roughly correspond to Seyferts and LINERs.

Due to selection biases, different surveys count more objects belonging to one class or the other. For example, a 1.4 GHz survey as FIRST or NVSS mostly selects steep-spectrum sources. Moderate and low-luminosity flat- or inverted-spectrum sources are mostly found to be BL Lac objects, while very weak, inverted-spectrum radio sources whose hosts are passive ellipticals could represent late phases of AGN evolution. These sources might be dominated by Advection-Dominated Accretion Flows (ADAFs), or Adiabatic Inflow-Outflow Solutions (ADIOS). Rees et al. (189) proposed that the final stage of gas accretion onto the black hole in massive elliptical galaxies might occur via ADAF, which require a very low radiative efficiency. In the ADIOS scenario (190) the outflow can be responsible to carry mass and angular momentum out, suppressing the radio emission from the most inner regions of the galaxy. Surveys at  $\nu > 5$  GHz are

## 6. GALAXY EVOLUTION ACROSS OPTICAL EMISSION-LINE DIAGNOSTIC DIAGRAMS

---

dominated, at high flux densities, by flat-spectrum sources. In these cases, the spectra also show higher complexity (e.g. bumps and inversions) and cannot be represented by simple power-laws. This complex spectral shape might result from the presence of peaked (self-absorbed) components, relativistically beamed along the line of sight (e.g. blazars).

To understand the role of AGN-feedback in the current scenarios of galaxy evolution and the connection between nuclear activity and development of the observed physical properties of the host, a study in the radio-optical domain is crucial to unveil the AGN/host coevolution, including the physical mechanisms that trigger the production of the emission lines or the radio-activity. In the scenario where powerful (predominantly high excitation) and weak (predominantly low excitation) radio AGNs represent different (i.e., earlier and later, respectively) stages of the blue-to-red galaxy evolution (102), the triggering of radio AGN activity is a strong function of host galaxy properties, linked to different stages of galaxy formation.

Despite lacking univocal observational evidence for the existence of a galaxy sequence along which all the spectral and morphological types can be represented, this thesis work aims at highlighting the chance of tracing galaxy evolution in diagnostic diagrams by using combined optical and radio properties. In particular, I make use of observations at the Effelsberg 100m telescope at 2.8 and 6 cm (10.45 and 4.85 GHz, respectively, see Chapter 3) to calculate spectral indexes and study the differences between star-forming galaxies, composite galaxies, Seyferts and LINERs, looking for possible evidence of an evolutionary sequence across the optical emission-line diagnostic diagrams.

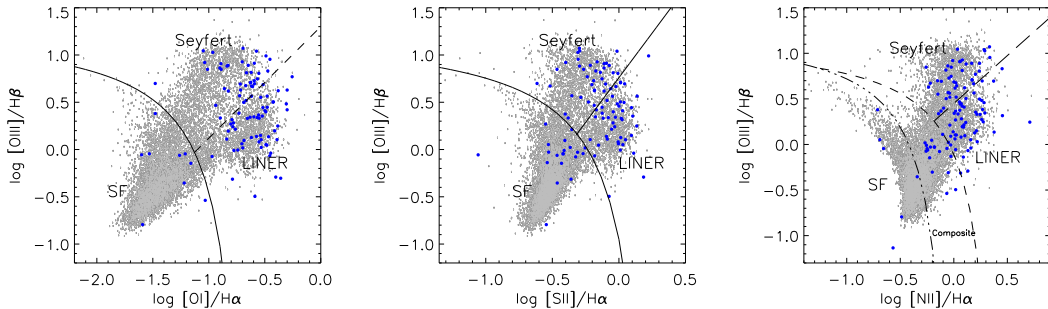


**Figure 6.1:** Diagnostic diagrams of the cross-matched optical-radio (grey) and Effelsberg (blue) samples. The curves in the right panel ([NII]-based diagram) were derived by Kewley et al. (25) (dashed) to set an upper limit for the position of star-forming galaxies, and by Kauffmann et al. (4) (three-point dashed), to trace the observed lower left branch (purely star-forming galaxies) more closely. The dividing line between Seyferts and LINERs was set by Schawinski et al. (28). In the middle ([SII]-based diagram) and right ([OI]-based diagram) panels, the demarcation curves are by Kewley et al. (26).

## 6. GALAXY EVOLUTION ACROSS OPTICAL EMISSION-LINE DIAGNOSTIC DIAGRAMS

---

### 6.2 Low-ionization emission-line diagnostic diagrams of the Effelsberg sample

In this study based on Effelsberg data (see Chapter 2) I make use of low-ionization emission line diagnostic diagrams to separate galaxies into four different spectral kinds: star-forming galaxies, composites, Seyferts, and LINERs. Low-ionization emission-line diagnostic diagrams (23, 24, 94, 106, 107, 136, 148, 149) are largely used by the astronomical community to classify galaxies according to the main contributions to line emission - photoionization by hot stars and/or SN-driven shocks from HII regions, photoionization by disk accretion or fast shocks from AGN, or both. In general, AGNs differ from star-forming galaxies because their ionizing fields have a high energy component. Behind the fully ionized region, there lie large partially ionized regions, which are kept hot by X-ray heating. It is in these regions that the [O I], [N II] and [S II] lines are generated efficiently.

In Fig. 6.1 the sources that I observed at the Effesberg telescope are distributed according to the relative strength of their emission lines. The SF region appears underpopulated, because the  $F_{20\text{cm}} > 100$  mJy cut mainly selects AGN. Seyferts have strong [OIII]/H $\beta$ , [N II]/H $\alpha$ , [S II]/H $\alpha$  and [O I]/H $\alpha$  (i.e. a wide range of ionization degrees). LINERs have lower ionization degree, which means weaker [OIII]/H $\beta$  but still strong [N II]/H $\alpha$ , [S II]/H $\alpha$  and [O I]/H $\alpha$ . HII regions have much weaker [O I]/H $\alpha$  and slightly weaker [N II]/H $\alpha$ . For this reason, the [O I]-based diagram is particularly useful to separate star-forming galaxies from AGN and, further, to distinguish Seyferts from LINERs. HII regions lie along a sequence in metallicity, of which [N II] is an indicator (134, 135). Low-metallicity galaxies have higher ionization and [OIII]/H $\beta$  values comparable to those of Seyferts. The [N II]/H $\alpha$  ratio presents a saturation point above which any further increase is only due to AGN contribution (26, 103).

In the [N II]/H $\alpha$  versus [OIII]/H $\beta$  or Baldwin-Phillips-Terlevich (BPT) diagram (Fig. 6.1, right panel), galaxies are distributed in two arms, representing star-forming galaxies and AGNs. Some of the AGN and composite galaxies occupy the star-forming regions of the other diagrams. This is especially the case for the [S II]/H $\alpha$  versus [OIII]/H $\beta$  diagram (Fig. 6.1, middle panel). The effect is thought to be related to the enhancement of [S II] lines in starburst galaxies, due to the mechanical energy released into the gas

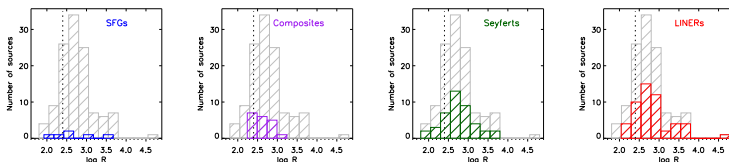


**Figure 6.2:** Radio-loudness distribution for each spectral kind as classified by the [NII]-based diagram. Star-forming galaxies are in blue, composites in purple, Seyferts in green and LINERs in red. In each panel, sources to the left of the dashed line ( $\log R = 2.4$ ) are radio quiet, while sources to the right are radio loud (Panessa et al. 2007). The overall Effelsberg sample is shown in grey.

SFGs		Composites		Seyferts		LINERs	
6		19		42		52	
R mean	R median	R mean	R median	R mean	R median	R mean	R median
2.66	2.61	2.61	2.58	2.74	2.72	2.83	2.70
Quiet	Loud	Quiet	Loud	Quiet	Loud	Quiet	Loud
2	4	4	15	8	34	7	45

**Table 6.1:** Statistics on the radio loudness of the sample. Row.1: Number of galaxies per spectral class as inferred from the [NII]-based diagram. Row.2: Mean and median values of  $R$  (radio loudness). Row.3: Number of radio-quiet and radio-loud objects per spectral class.

by supernovae and stellar winds (also called *shock excitation*, 136)

## 6.3 Results

### 6.3.1 Radio loudness

Galaxies can be classified into two families, radio quiet and radio loud, depending on the value of their radio luminosity ( $L_R$ ) over their optical luminosity ( $L_O$ ).  $\log L_R \lesssim 2.4 \times \log L_O$  in case of radio quiet objects, and  $\log L_R \gtrsim 2.4 \times \log L_O$  in case of radio loud galaxies (191). It is commonly accepted that only 10% of AGNs are radio loud. In radio loud AGNs, the biggest contribution to the integrated radio luminosity comes from the compact nucleus, or the extended lobes. Seyfert galaxies are considered as “strong” AGNs when observed at optical wavelengths, but are mostly radio quiet. LINERs, on

## 6. GALAXY EVOLUTION ACROSS OPTICAL EMISSION-LINE DIAGNOSTIC DIAGRAMS

---

the other hand, can be either radio quiet or loud. They are often addressed as “weak” AGNs, since they show narrow-emission lines of moderate strength.

Note that the radio loudness classification is to some degree arbitrary, as there is a continuum of radio loudness values, with no obvious bimodality in this distribution. Radio loudness suffers from selection effects. As radio galaxies are selected to have high radio luminosities, this results in large values of  $R$  and the lack of many low-power galaxies and AGNs (151). This is the case for our sample, where the lower limit in radio flux density ( $F_{1.4\text{GHz}} \geq 100$  mJys) selects strong radio emitters, leading to a quite severe selection bias. In the optical regime, radiation from star-forming galaxies could be suppressed by dust, which would result in high radio-optical flux ratios (192). These sources are, however, mostly revealed as submillijansky and microjansky radio sources placed at high redshifts ( $z \gtrsim 1$ , see 193), and are excluded from our sample. Another problem arises when computing the optical luminosity. A correct computation of the  $R$  parameter would imply a method to subtract the contribution of the host to the overall optical emission, e.g. via galaxy image decomposition, which disentangles nuclear and bulge components. This technique, although powerful, can be used on high-resolution images only, and at best for local sources. When the host-light subtraction is not achievable, central optical luminosity is the next good option. Unfortunately, the Effelsberg sample has been selected to avoid aperture effects. Thus, the 3” SDSS fibers collect light from the galaxy nuclear regions as well as from the bulge, and we cannot retrieve central luminosities. All this evidence suggests that radio loudness varies strongly for different galaxy populations, and it is arduous to estimate  $R$  for a mixed sample of radio-bright star-forming galaxies and AGNs placed at intermediate redshifts. We nevertheless calculate the radio loudness seeking for broad trends in our sample.

The sample I have observed at Effelsberg is composed by 6 SFGs, 19 composites, 42 Seyferts, and 52 LINERs. In the local universe, powerful AGN are rather rare objects and we would expect the percentage of radio-loud sources to be low. However, this intermediate-redshift ( $0.04 \leq z < 0.4$ ) sample has been selected to have high radio fluxes at 20 cm, and this leads to the selection of many radio-loud sources. I calculate the radio loudness ( $R$ ) of the sample by using the logarithmic ratio between the 4.85 GHz integrated flux and the  $g$ -band and  $r$ -band observed flux densities in Jy (calculated from SDSS DR7). There is no obvious bimodality in  $R$  as seen in the overall Effelsberg

sample (Fig. 6.2). The dividing line, though, corresponds well to the location of the peak in the observed radio loudness distribution. I found that 98 (82.3%) of our radio emitters are radio loud, and 21 (17.6%) are radio quiet. Radio loudness for each spectral class is also shown in Fig. 6.2, and the statistics are listed in Tab. 6.1. LINERs are the most radio loud objects of the sample (mean  $R = 10^{2.83}$ , median  $R = 10^{2.70}$ ) and their  $R$  reaches values of  $R \sim 10^{4.70}$ . Seyferts and LINERs show a gaussian distribution, with peaks at  $R \sim 10^{2.7}$

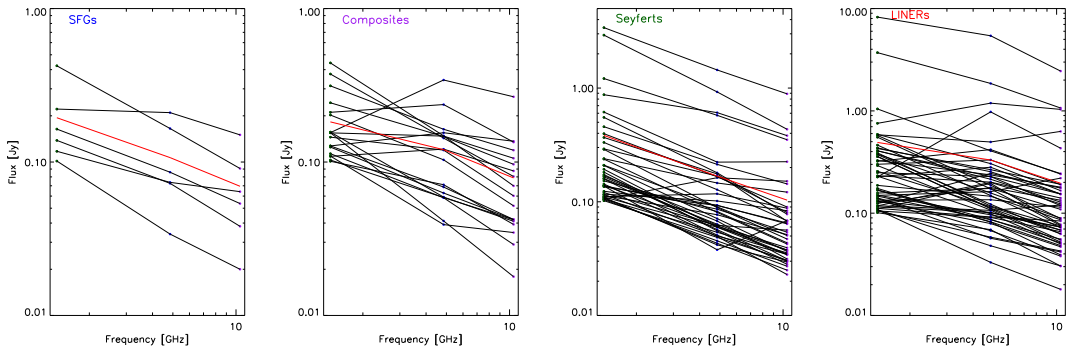


**Figure 6.3:** Radio spectra of the Effelsberg sample. Dots indicate the fluxes at 1.4 GHz (20 cm, FIRST data, green), 4.85 GHz, and 10.45GHz (6 and 2.8 cm, respectively, from Effelsberg observations, blue and purple). Spectra are divided in 4 classes: Star-forming galaxies, composites, Seyferts and LINERs, according to the [NII]-based classification. Mean spectra are shown in red in each panel.

### 6.3.2 Radio spectra

Fig. 6.3 shows the three-point radio spectra, divided by spectral classes as in Fig. 6.1 (right panel). Mean spectra are represented in red. Most of the spectra are rather steep, especially when lying in the SFG or Seyfert region of the diagnostic diagram. A few spectra seem to peak at around 5 GHz. This is usually an indication of extremely compact sources (GHz-Peaked Sources or GPS<sup>1</sup>, and Compact Steep Sources sources or CSS<sup>2</sup>), whose nuclear radio emission peaks at high radio frequencies (up to  $\sim 5$  GHz), giving the spectra an “humped” look. A few other sources show a concave shape instead. This is because sources show both the emission contribution from the extended structures (lobes, which have steep spectra) at  $\nu < 5$  GHz, and from the nucleus, which makes the spectra rise at frequencies higher than 10.45 GHz (inverted spectra). However, it must be mentioned that Effelsberg data (4.85-10.45 GHz) correspond roughly to the radio emission from the core. This is because the lobes, when present, emit at lower frequencies, due to the aging of the synchrotron radiation. Therefore, we assume that the flattening of the spectral index comes almost exclusively from core activity.

### 6.3.3 Spectral index and spectral curvature

In general, high radio-flux sources are found to be powerful AGN, while the fainter sources include many more normal or starburst galaxies. At GHz frequencies, it is more common to observe compact flat spectrum AGN. In Fig. 6.4, a set of histograms show the spectral index distribution<sup>3</sup> as derived for the data at 4.85 and 10.45 GHz for star-forming, composite, Seyfert, and LINER galaxies. The mean error on the spectral index is  $\sigma_{\alpha \text{ mean}} = 0.22$ , while the median is  $\sigma_{\alpha \text{ median}} = 0.14$ , estimated from the theory of the propagation of errors:

$$\sigma_{\alpha} = \frac{1}{\log(10.45/4.85)} \times \sqrt{\left(\frac{\sigma_{F_{4.85}}}{F_{4.85}}\right)^2 + \left(\frac{\sigma_{F_{10.45}}}{F_{10.45}}\right)^2} \quad (6.1)$$

where 10.45 and 4.85 are the observing frequencies in GHz,  $\sigma_{F_{4.85}}$  and  $\sigma_{F_{10.45}}$  are the errors on the fluxes, and  $F_{4.85}$  and  $F_{10.45}$  the observed fluxes.

The grey histograms of the overall population show one peak at  $\alpha \sim -0.7$  and another

<sup>1</sup>GPS are compact sources whose radio emission peaks at GHz frequencies. They have been hypothesized to be young sources, progenitors of the more extended radio galaxies.

<sup>2</sup>CSS are compact sources whose radio emission decreases with the frequency.

<sup>3</sup>The spectral index is defined as  $\alpha$  in  $F \propto \nu^{\alpha}$ .

## 6. GALAXY EVOLUTION ACROSS OPTICAL EMISSION-LINE DIAGNOSTIC DIAGRAMS

---

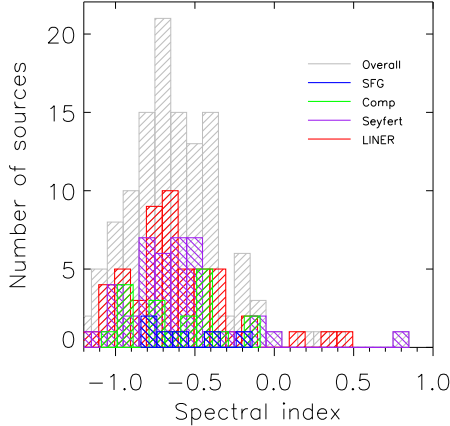


**Figure 6.4:** Spectral index distribution per galaxy spectral class. Colors indicate the spectral classes according to the  $[\text{N II}]$ -based diagnostic diagram. The overall Effelsberg population is plotted in grey.

(tentative) one at  $\alpha \sim -0.2$ . As suggested by previous studies (194), at 5 GHz the spectral index distribution shows indeed two peaks. The highest peak is at  $\alpha \sim -0.7$ , while the second is at  $\alpha \sim 0$ . It has been shown that, at short cm-wavelengths, the distribution has still a bimodal shape, with the most prominent peak at  $\alpha \sim 0$ . The overall  $\alpha$  distribution for the Effelsberg sources does not show clear bimodality. Seyferts and LINERs span a wider  $\alpha$  range than star-forming galaxies and composites. As a comparison, I calculate the spectral index for the 1.4 GHz (FIRST) and 4.85 GHz (Effelsberg) non-simultaneous data. I then calculate the spectral curvature ( $C$ ), defined as  $\alpha_{[4.85-10.45\text{GHz}]} - \alpha_{[1.4-4.85\text{GHz}]}$  following Gregorini et al. (195). Spectral curvature includes the effect of spectral variability, i.e. change in the spectral slope between 1.4 – 4.85 GHz and 4.85 – 10.45 GHz. Variability can be due to flux increase at the highest frequencies of the spectral range, because of the flaring of the compact nucleus on short time scales. FIRST data were collected about 18 years ago, so a change in the spectral index on time-scales of years may be associate to nuclear variability.

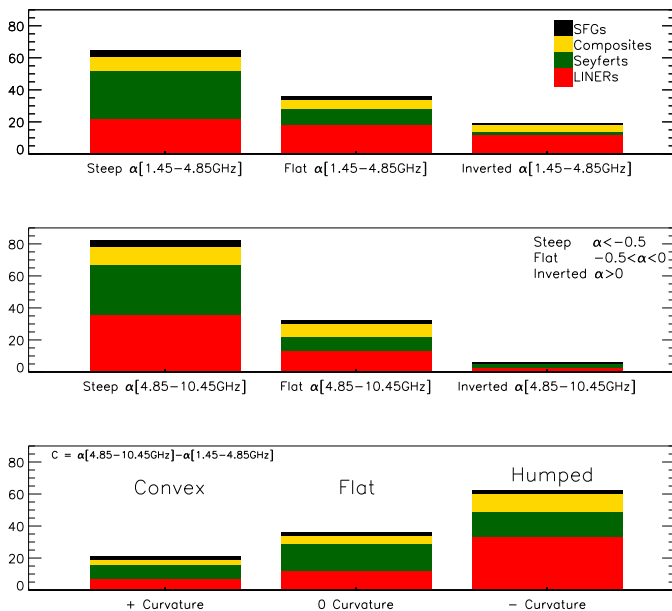


**Figure 6.5:** Spectral indexes and spectral curvature per galaxy spectral class. The top panel shows the cumulative histograms of the spectral index  $\alpha_{[1.4-4.85\text{GHz}]}$ , while the middle panel shows  $\alpha_{[4.85-10.45\text{GHz}]}$ . Spectra are classified as steep, flat, or inverted. The bottom panel shows the spectral curvature ( $C$ ), defined as the difference between  $\alpha_{[4.85-10.45\text{GHz}]}$  (higher frequency) and  $\alpha_{[1.4-4.85\text{GHz}]}$  (lower frequency).

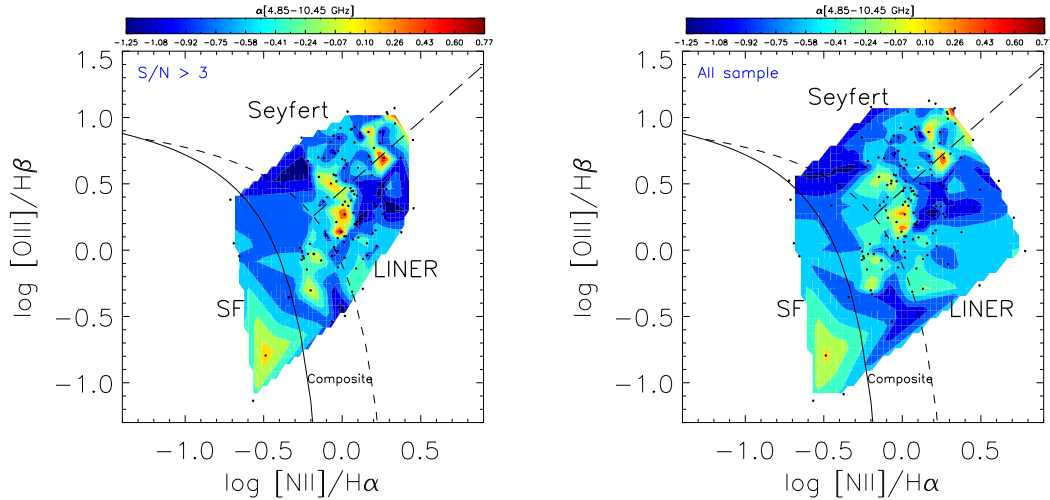


**Figure 6.6:** Spectral index distribution represented in the diagnostic diagram. The color gradient indicates the  $\alpha[4.85-10.45 \text{ GHz}]$  values, blue meaning steep and red inverted. Black dots correspond to source positions. The left panel shows only sources with  $S/N > 3$ , while the right panel shows the entire sample.

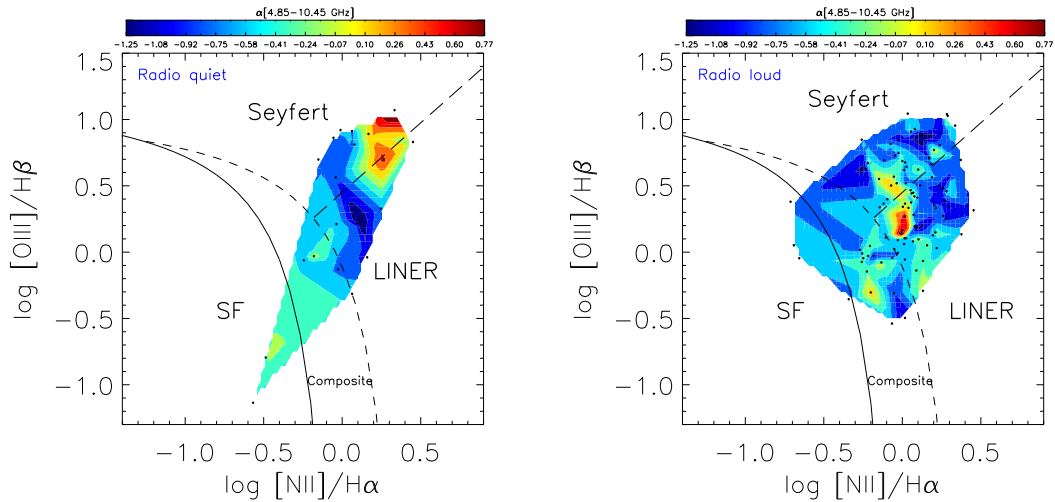


**Figure 6.7:** Spectral index distribution for radio quiet (left panel) and radio loud (right panel) galaxies.

## 6. GALAXY EVOLUTION ACROSS OPTICAL EMISSION-LINE DIAGNOSTIC DIAGRAMS

---

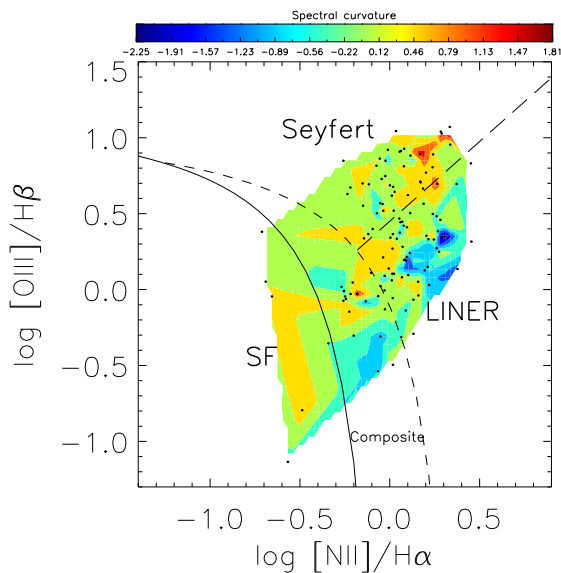
Variability on short time scales (days to years) is a secure signature of AGN activity, and can be addressed as a method to select those objects from a galaxy survey. Surprisingly, the cases of highest variations in the spectral indexes as calculated at different frequencies are not associated with blazars or blazars candidates (according to NED classification).

Fig. 6.5 shows cumulative histograms of the spectral indexes, divided per spectral classes. Here I call the spectra “steep” when  $\alpha \leq -0.5$ , “flat” when  $-0.5 < \alpha \leq 0$ , and “inverted” when  $\alpha > 0$ . In the top panel it is shown that most of the sources have a rather steep spectrum between 1.4 and 4.85 GHz. Seyfert galaxies dominate the distribution, though they are not the most abundant spectral class in the sample. On the other hand, LINERs show the highest number of flat and inverted spectra at these wavelengths. At the higher Effelsberg frequencies (4.85-10.45 GHz, middle panel), the number of steep-spectra sources slightly increases, especially in case of LINERs. The bottom panel of Fig. 6.5 shows the spectral curvature. Curvature classes are: concave ( $C \geq 0.1$ ), flat ( $-0.1 < C < 0.1$ ), and humped ( $C \leq -0.1$ ). Seyferts dominate the “concave” and “flat” distributions, while LINERs are the class of objects showing the highest number of “humped” spectra, peaking at  $\sim 5$  GHz. Following the relation between turnover frequency, source size, turnover frequency and peak flux density, as well as magnetic field strength (196) this implies that the high frequency emission of Seyferts along the division line between Seyferts and LINERs in the [N II] diagram is dominated by (milli)arcsecond sized radio core components, whereas the emission of LINERs is dominated by larger source components. Those could be due to (up to several) milliarcsecond sized components that may be associated with nuclear jets, compact working points in radio lobes, or very compact wind/shock regions that are bright in the radio domain.

Fig. 6.6 shows the spectral index distribution in the BPT diagnostic diagram. In the left panel, only sources with  $S/N > 3$  are represented. Flat (green-yellow) and inverted (orange-red) sources in this 119-galaxy sample are mainly clustered along a diagonal line that extends from the end of the star-forming sequence to the Seyfert region. The spectral index “flattening sequence” roughly follows the division line between Seyferts and LINERs. An extra region of spectral flattening is located at the bottom of the LINER region, close to the composites-division line. In the right panel, also sources with  $S/N < 3$  are represented. With a better statistics, the plot shows the same trend

as in the left panel.

In Fig. 6.7 I check whether the flattening of the spectral index is only present in case of radio loud objects. In the left panel, I plot the radio-quiet galaxies. Though most of the radio quiet sources have steep spectra ( $\alpha_{[4.85-10.45\text{GHz}]} \leq -0.5$ ), the sources with flat/inverted spectra ( $\alpha_{[4.85-10.45\text{GHz}]} > -0.5$ ) are located along the sequence described above. Outliers have steeper spectra. The trend is even clearer in the right panel of Fig. 6.7, where the radio-loud galaxies are shown.



**Figure 6.8:** Spectral curvature distribution represented in the diagnostic diagram. The color gradient indicates the spectral curvature values. Black dots correspond to source positions.

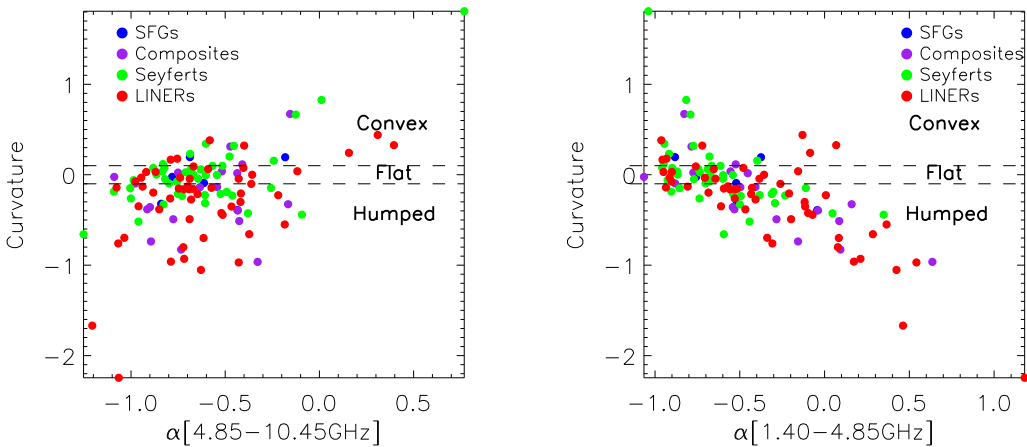


**Figure 6.9:** Spectral indexes versus spectral curvature. The left panel shows the trend between  $\alpha_{[4.85-10.45\text{GHz}]}$  and  $C$ . The dashed lines indicate  $0.1 < C < 0.1$ , while the colors refer to the four different spectral classes. The right panel shows the anti-correlation between  $\alpha_{[1.40-4.85\text{GHz}]}$  and  $C$ .

Fig. 6.8 illustrates the spectral curvature distribution in the BPT diagram. The diagram shows a clearer difference between Seyferts and LINERs with respect to the spectral index distribution in Fig. 6.6. This is because star-forming galaxies and Seyferts tend to have a zero or positive curvature, indicating flat or concave-shaped spectra, while LINERs show more humped spectra, as shown in Fig. 6.5.

Fig. 6.9 shows the correlations between spectral indexes and spectral curvature for star-forming galaxies, composites, Seyferts and LINERs. Composite galaxies and LINERs are spread over the diagram. Star-forming galaxies show humped spectra only in one case at frequencies between 4.85 and 10.45 GHz (left panel). Seyfert galaxies are more clustered in the “flat curvature” part of the diagrams, though still a few of them show humped or convex spectra.

**Table 6.2:** Sources observed with the Effelsberg telescope at 10.45 and 4.85 GHz. From left to right: redshift ( $z$ ), coordinates (RA, DEC), integrated flux density at 1.4 GHz ( $F_{[1.4\text{GHz}]}$ ) in mJy, flux density at 10.45 GHz ( $F_{[10.45\text{GHz}]}$ ) in Jy, its error (Err), flux density at 4.85 GHz ( $F_{[4.85\text{GHz}]}$ ) in Jys, its error (Err), optical morphology ( $M_o$ ) from SDSS images, radio morphology ( $M_r$ ) from FIRST images, activity type (Activity) from NED, and spectral classification according to the [OI]-, [SII]-, [NII]-based diagnostic diagrams ( $OI_d$ ,  $SII_d$ ,  $NIId$ ). Optical morphology: “E” stands for elliptical, “Cl” for cluster, “S” for spiral, “SB” for barred spiral, “PM” for post merger, “Comp” for compact and “int” for interacting. Radio morphology: “PS” stands for point source, “NAT” for not asymmetric tales (lobes), “Extend” for extended source, “Asym dbl” for asymmetric double. Activity type: “r-1” stands for radio-loud, “Blaz” for blazars, “c” for candidate.

$z$	RA	DEC	$F_{[1.4\text{GHz}]}$	$F_{[10.45\text{GHz}]}$	Err	$F_{[4.85\text{GHz}]}$	Err	$M_o$	$M_r$	Activity	$OI_d$	$SII_d$	$NIId$
0.298	204.38	0.5913	127.25	0.1366	0.0015	0.1552	0.0027	E	PS	BLLAC	L	SF	C
0.106	176.30	-2.994	108.93	0.0875	0.0374	0.1213	0.0281	E	PS	AGN	L	SF	C
0.112	185.30	-2.816	105.55	0.1516	0.0036	0.1628	0.0108	E	PS	AGN	L	S	S
0.182	184.48	-3.623	208.86	0.0366	0.0043	0.0711	0.0029	E	PS	AGN	S	S	S
0.247	261.84	55.181	149.13	0.2200	0.0034	0.1624	0.0030	E/Cl	PS		L	L	L
0.041	222.34	63.270	2922.8	0.4338	0.0049	0.9249	0.0047	SBO	PS/FRI?	Sy2	S	S	S
0.105	240.69	52.732	575.70	0.0886	0.0078	0.1876	0.0024	SO/E	PS	Sy1	L	L	L
0.179	239.86	53.515	182.35	0.0282	0.0096	0.0555	0.0019	E	PS	Sy2	S	L	S
0.224	251.08	45.779	115.05	0.0684	0.0008	0.1020	0.0024	E	lobes/FRI?	BLLAC c	SF	SF	L
0.084	181.02	2.4118	145.27	0.0602	0.0031	0.1196	0.0031	E/SO	lobes		SF	SF	C
0.050	159.13	2.3626	202.42	0.0518	0.0000	0.1033	0.0029	S/PM	Double PS	III	SF	SF	C
0.370	223.41	3.9926	378.48	0.0893	0.0035	0.1575	0.0028	E	PS		L	L	L
0.086	323.38	-7.213	193.21	0.0376	0.0000	0.0597	0.0018	S	PS	AGN	S	S	S
0.040	119.61	37.786	225.50	0.4315	0.0012	0.9773	0.0069	SO	Jets/FRII		L	L	L
0.131	127.91	46.133	130.74	0.0732	0.0116	0.1008	0.0034	E	PS		L	L	L
0.225	143.62	3.0959	292.08	0.0521	0.0023	0.1071	0.0013	E	PS		L	L	L
0.319	119.09	35.911	423.67	0.0907	0.0000	0.1653	0.0027	E	PS		SF	SF	SF
0.055	129.15	44.019	139.30	0.0394	0.0046	0.0609	0.0007	SO	PS	AGN	S	S	S
0.097	155.57	0.5139	167.36	0.0482	0.0012	0.0824	0.0030	SO	PS	AGN	L	L	L
0.096	159.02	0.1018	109.91	0.0774	0.0019	0.1953	0.0036	Scd	Jets/FRII		L	SF	L
0.187	235.82	2.5976	442.5	0.0699	0.0035	0.1481	0.0027	E	PS	Sy2	SF	SF	C
0.263	201.08	4.3186	155.16	0.0179	0.0015	0.0413	0.0011	E	PS	AGN	L	L	C
0.133	211.78	4.8837	109.33	0.0347	0.0378	0.0391	0.0002	E	PS	AGN	L	SF	C
0.095	228.85	4.3627	138.32	0.0381	0.0039	0.0726	0.0030	S	PS	III	SF	SF	SF
0.052	230.34	4.3418	155.38	0.2662	0.0008	0.3424	0.0048	E/SO	Jet?		SF	SF	C
0.190	234.65	55.428	209.83	0.0505	0.0012	0.0902	0.0025	E	PS	Sy2	S	S	S
0.149	206.32	-1.940	374.64	0.0805	0.0023	0.1432	0.0037	E/SO	PS	AGN/r-1	L	L	C
0.239	207.65	-3.345	104.48	0.0271	0.0004	0.0453	0.0004	E	PS?	AGN	S	S	S
0.166	208.09	-1.946	552.19	0.0778	0.0070	0.1797	0.0036	E	PS		S	S	S
0.132	214.17	-2.936	101.12	0.0392	0.0000	0.0711	0.0033	E/SO	PS	AGN	L	SF	C
0.137	234.47	-0.955	107.55	0.0250	0.0034	0.0431	0.0022	E	PS	Sy2/NLAGN	S	S	S
0.266	223.16	6.4606	291.60	0.0805	0.0011	0.1683	0.0027	S	PS		S	S	S
0.102	229.69	6.2322	210.86	0.1348	0.0095	0.2368	0.0034	SO	NAT/jet?		SF	SF	C

0.195	339.40	0.3441	115.98	0.0346	0.0062	0.0499	0.0004	E	PS	AGN	S	L	S
0.276	355.27	0.3093	428.95	0.1915	0.0108	0.2661	0.0004	S/E	PS	NLAGN	S	S	L
0.266	132.51	40.602	118.29	0.1200	0.0019	0.1064	0.0025	E	PS	AGN	L	SF	L
0.082	122.41	34.926	154.86	0.1058	0.0004	0.1476	0.0026	E/SO	jet?	BLLAC	L	SF	L
0.172	124.00	38.070	157.25	0.1089	0.0008	0.1746	0.0011	E	Extend		L	SF	L
0.143	164.65	56.469	221.38	0.1503	0.0780	0.2098	0.0023	S/E	PS	BLLAC	SF	SF	SF
0.084	136.56	46.605	313.57	0.1194	0.0089	0.1635	0.0009	SO	PS	LINER	L	L	C
0.151	156.57	45.708	105.18	0.0659	0.0046	0.0909	0.0019	E	PS		L	L	L
0.178	222.33	42.350	165.63	0.0563	0.0033	0.0620	0.0006	PM/QSO	PS	Blaz	S	S	S
0.214	162.71	7.9477	138.52	0.0540	0.0015	0.0861	0.0040	E	PS		S	S	S
0.129	141.36	7.4449	103.06	0.0420	0.0004	0.0587	0.0008	SO	PS		SF	SF	C
0.117	210.21	52.268	174.49	0.0391	0.0056	0.0817	0.0020	E	PS	AGN	L	L	L
0.099	218.84	50.856	140.96	0.0380	0.0012	0.0674	0.0004	E	PS	AGN	L	L	L
0.076	212.95	52.816	321.58	0.2412	0.0034	0.4185	0.0048	E	Extend		L	SF	L
0.151	242.95	40.672	553.08	0.0757	0.0004	0.1730	0.0035	E	PS		L	L	L
0.079	129.81	28.844	124.72	0.1760	0.0131	0.2445	0.0043	E/SO	jet		S	S	L
0.115	133.34	9.4622	123.72	0.0650	0.0027	0.0927	0.0013	E/SO	PS		S	S	S
0.206	188.45	50.439	243.22	0.0966	0.0027	0.1466	0.0030	E/SO	Extend	Blaz	L	SF	C
0.206	191.78	49.005	1212.6	0.3512	0.0005	0.5757	0.0018	E	PS	Sy2	L	L	S
0.083	184.36	15.903	137.5	0.0682	0.0171	0.0378	0.0030	S	PS		S	S	S
0.152	206.18	55.050	456.95	0.1436	0.0005	0.2132	0.0013	E	PS	AGN	S	S	S
0.152	214.94	54.387	583.66	0.6297	0.0092	0.4965	0.0053	E/SO/QSO	Double PS	BLLAC	SF	SF	SF
0.078	226.84	10.312	407.85	0.1281	0.0085	0.2146	0.0029	SO,Comp	PS		L	L	L
0.082	210.80	6.1691	125.0	0.1338	0.0091	0.1781	0.0029	E/SO	jets		L	SF	L
0.132	207.59	9.6696	300.57	0.1904	0.0081	0.3315	0.0039	E/CI	PS	Blaz/Sy1.9	L	L	L
0.061	220.07	5.9427	133.99	0.1144	0.0083	0.1353	0.0029	SO	Extend?		S	S	L
0.109	230.95	32.230	169.28	0.0314	0.0058	0.0677	0.0016	SO	PS		S	S	S
0.135	229.28	33.889	120.38	0.0346	0.0000	0.0616	0.0014	E/QSO2	Double PS	Sy1	S	S	S
0.148	212.42	36.071	143.24	0.0229	0.0004	0.0495	0.0018	E/int	PS		S	S	S
0.241	128.72	55.572	8254.5	2.4487	0.1362	5.4221	0.0388	E/int/QSO?	PS	LINER	L	L	L
0.095	124.72	22.796	187.0	0.0862	0.0050	0.1463	0.0026	E	Asym dbl		L	L	L
0.081	164.16	14.324	173.41	0.0302	0.0008	0.0568	0.0060	S/PM	PS		S	L	S
0.112	123.34	7.5682	462.92	0.0720	0.0012	0.1488	0.0039	E/SO_bar	PS	Sy1	L	L	L
0.099	151.50	34.902	3399.3	0.8897	0.0098	1.4429	0.0141	SO	PS	LINER	L	L	S
0.098	121.50	19.104	113.29	0.0514	0.0031	0.0769	0.0003	SO	FRII?		S	S	S
0.158	138.08	27.929	230.35	0.0500	0.0012	0.0984	0.0011	E	PS		L	L	L
0.062	176.84	35.018	615.09	0.2251	0.0244	0.2232	0.0035	SO/Comp	Jets	BLAC?/Sy2	S	S	S
0.230	224.08	27.919	108.12	0.0305	0.0066	0.0480	0.0025	E	PS		S	L	L
0.289	212.22	30.350	332.55	0.0681	0.0006	0.1277	0.0023	E	PS		S	S	S
0.078	188.00	33.296	101.47	0.0200	0.0050	0.0339	0.0002	S	Extend		SF	SF	SF
0.045	208.07	31.446	3709.1	1.0669	0.0706	1.8531	0.0135	S	FRI	LINER	L	L	L
0.091	160.12	29.966	388.36	0.0751	0.0288	0.1174	0.0024	S	PS		L	L	L
0.159	212.06	25.565	589.27	0.1661	0.0098	0.3051	0.0043	E	Extend		L	L	L
0.079	249.98	11.466	163.94	0.0536	0.0073	0.0858	0.0030	S/int?	PS		SF	SF	SF
0.154	128.06	18.536	874.23	0.3816	0.0008	0.6079	0.0015	E,N_gal	PS		S	S	S
0.089	127.27	17.904	231.80	0.1405	0.0023	0.2010	0.0028	E/SO	Jets	BLLAC c	L	L	L
0.155	179.22	26.542	116.58	0.0834	0.0016	0.1016	0.0022	SO?.g	PS		L	S	S
0.112	170.12	27.603	156.75	0.0411	0.0004	0.0591	0.0026	E	PS		SF	SF	C

6. GALAXY EVOLUTION ACROSS OPTICAL EMISSION-LINE  
DIAGNOSTIC DIAGRAMS

0.063	162.38	23.456	105.55	0.0427	0.0027	0.0582	0.0018	E/S0	Extend		L	SF	L
0.134	167.58	21.529	289.01	0.0470	0.0024	0.0889	0.0015	S/int?	PS		S	S	S
0.349	185.52	23.193	374.16	0.0627	0.0000	0.1222	0.0021	E	Extend		L	SF	L
0.250	214.47	20.668	110.83	0.0878	0.0016	0.1175	0.0028	E	jet?		S	S	S
0.135	141.02	14.172	108.25	0.0180	0.0008	0.0330	0.0009	E/S0/QSO	PS		L	L	L
0.214	230.31	15.202	356.98	0.0628	0.0038	0.1121	0.0025	E	PS		L	L	L
0.178	166.75	18.430	159.92	0.0376	0.0004	0.0634	0.0017	S0/int?	PS		S	S	S
0.137	169.27	20.235	117.45	0.0641	0.0004	0.0737	0.0029	S0	PS	Sy2/BLLAC?	SF	SF	SF
0.144	212.61	14.644	434.41	0.1544	0.0103	0.2537	0.0036	E/S0	Extend		L	SF	L
0.187	227.46	15.957	406.70	0.1185	0.0058	0.2276	0.0054	E	Double PS		S	L	L
0.229	187.09	16.437	105.58	0.0355	0.0066	0.0539	0.0028	E	lobes		S	S	S
0.180	202.24	17.645	158.77	0.0300	0.0012	0.0508	0.0019	E/S0	PS		S	S	S
0.238	190.46	16.556	359.38	0.0545	0.0039	0.1104	0.0031	E	PS		L	L	L
0.066	131.33	11.431	168.82	0.0512	0.0019	0.0871	0.0023	S0	Extend		L	L	L
0.212	152.48	14.031	1044.7	0.2435	0.0194	0.4066	0.0045	E	PS		L	L	L
0.163	245.13	17.665	111.44	0.0839	0.0019	0.0918	0.0034	S0/int?	PS		S	S	S
0.101	138.00	53.343	135.64	0.0639	0.0015	0.0932	0.0042	S0/E	Double PS	NLAGN/Sy2	S	S	S
0.255	201.34	3.9802	113.29	0.0290	0.0004	0.0585	0.0027	E	PS	AGN	SF	SF	C
0.104	7.1392	0.9197	237.22	0.0425	0.0015	0.0806	0.0064	S/S0	PS	Sy2/r-1	S	L	S
0.247	37.788	0.9509	109.26	0.0295	0.0023	0.0418	0.0017	E	PS		L	S	S
0.195	221.80	40.796	396.94	0.0899	0.0020	0.1659	0.0011	E	Extend		L	SF	S
0.125	172.92	47.002	127.34	0.0422	0.0006	0.0687	0.0011	S0	PS		L	SF	C
0.204	173.82	12.886	139.19	0.0418	0.0008	0.0568	0.0031	E	PS		L	L	L
0.058	180.83	13.325	110.27	0.0341	0.0031	0.0597	0.0024	S0	Double PS?	AGN	L	L	S
0.258	217.05	39.205	239.44	0.1214	0.0031	0.1462	0.0022	S0/QSO?	Extend?	Blaz	L	S	S
0.299	176.41	44.339	327.30	0.1794	0.0002	0.2368	0.0017	S0/QSO?	Extend	AGN	L	S	L
0.085	196.58	11.227	117.94	0.1233	0.0000	0.1998	0.0029	E0	lobes		L	L	L
0.066	199.41	41.262	248.86	0.1537	0.0074	0.2280	0.0001	S0	PS		L	L	L
0.131	185.38	8.3622	150.13	0.0733	0.0134	0.0964	0.0030	S0	PS	BLLac?	L	L	L
0.249	191.08	40.860	367.63	0.0672	0.0023	0.1757	0.0014	S0/QSO?	PS	Sy?	S	S	S
0.083	190.53	9.4793	101.15	0.0304	0.0016	0.0690	0.0055	E	jet?		L	L	L
0.168	224.40	43.993	152.63	0.0435	0.0052	0.0821	0.0027	S0	jet?		S	S	S
0.232	234.74	35.952	146.91	0.0556	0.0016	0.0863	0.0026	E	Extend		L	SF	L
0.237	253.23	25.952	125.12	0.0422	0.0014	0.0628	0.0000	E	PS		L	SF	C
0.153	137.47	17.857	257.0	0.0681	0.0011	0.1155	0.0019	S0	PS		SF	SF	L
0.130	170.95	20.281	102.18	0.0306	0.0034	0.0486	0.0026	S0	PS		S	S	S
0.104	137.97	37.403	226.92	0.1536	0.0004	0.2813	0.0015	S0	Extend		L	SF	L
0.052	229.16	0.2505	755.71	1.0338	0.0568	1.1906	0.0108	S0/Comp	FRII	LINER	L	L	L

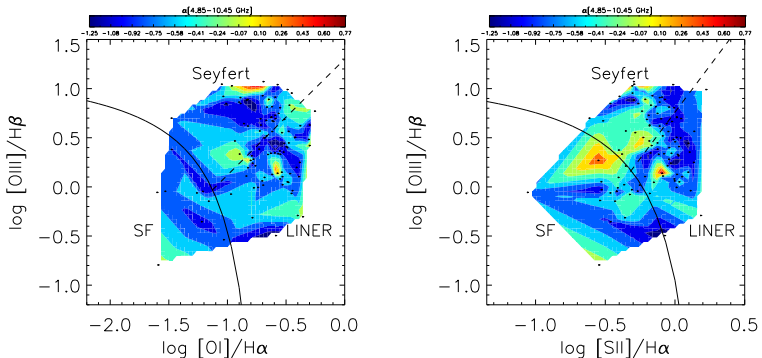


**Figure 6.10:** Spectral index distribution in the additional low-ionization emission-line diagnostic diagrams. The [O I]-based and the [S II]-based diagrams show 100 galaxies each.

Tab. 6.2 contains general information about the sample, such as redshift, coordinates, fluxes, morphological and spectral classifications. Fig. 6.10 shows the [O I]- and the [S II]-based diagnostic diagrams. Here a flattening of the spectral index along a sequence is not well visible as in Fig. 6.6, probably due to the fact that the composite region which is present in the [N II]-based diagram is not shown in the other two diagrams.

### 6.3.4 Black hole mass

I calculate the black hole mass from the scaling relation with stellar velocity dispersion according to Gueltekin et al. (197):

$$M_{BH} = 8.12 + 4.24 \times \log \frac{\sigma}{200 \text{ km/s}} \quad (6.2)$$

The stellar velocity dispersion measurements are from the SDSS DR7. Fig. 6.11 shows the  $M_{BH}$  distribution in the BPT diagram. The objects with the highest black hole masses ( $M_{BH} > 10^{8.5} M_{\odot}$ ) are mostly located in the LINER region of the diagram. For a few objects (indicated with white circles) the determination of the black hole mass is not reliable<sup>1</sup>. The latter objects are not isolated cases of stellar velocity dispersion mis-measurements, but they occupy precise regions of the diagnostic diagrams of the parent

<sup>1</sup>According to error flags on the measurement of  $\sigma$ , which is measured from the Balmer lines.

## 6. GALAXY EVOLUTION ACROSS OPTICAL EMISSION-LINE DIAGNOSTIC DIAGRAMS

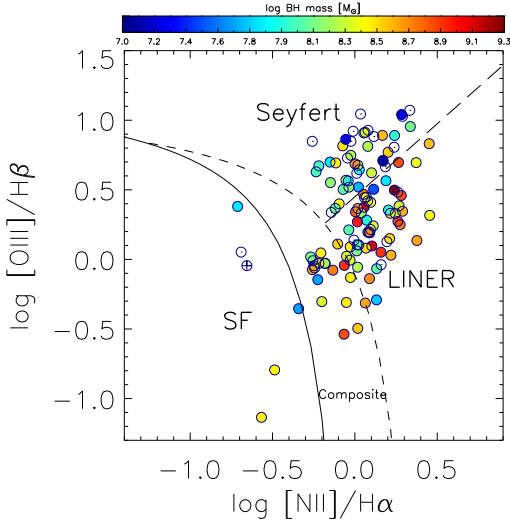
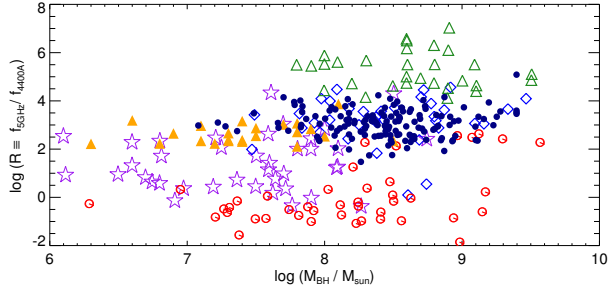


**Figure 6.11:** Black hole masses distribution. The color bar indicates  $M_{BH}$  in solar masses, where blue means low black hole mass and red means high. White circles indicates sources where the SDSS measurement of the stellar velocity dispersion is not accurate. The crossed circle indicates again a non reliable measurement, which has not been flagged in the SDSS catalog.

sample (cross-matched SDSS-FIRST). In particular, I checked the SDSS morphology and identified the Seyferts that have very high  $[OIII]/H\beta$  with the newly discovered population of “green beans” galaxies (198). These objects appear green in the SDSS images, and often show signs of perturbed morphology and post-merger activity. The perturbations the green beans undergo could be an explanation for the stellar velocity dispersion mismeasurements. A second class of objects, having extremely high black hole masses ( $\geq 10^9-10^{10} M_{\odot}$ ) and located on the left-hand side of the diagram, may be part of the “green peas” population (199). Green peas are associated with starburst activity and are very compact, blue-green galaxies showing merging activity. According to Cardamone et al. (199), the green peas might be the downscaled version of high redshift massive merging galaxies, observed in the local universe due to the mass



- $\triangle$  Fanaroff-Riley I sources
- $\diamond$  Broad-line Radio Loud galaxies
- $\star$  Seyferts and LINERs
- $\circ$  PG Quasars (Sikora+ 2007)
- $\blacktriangle$  Radio-loud NLSy1s (Yuan+ 2008)
- $\bullet$  Effelsberg (this work)

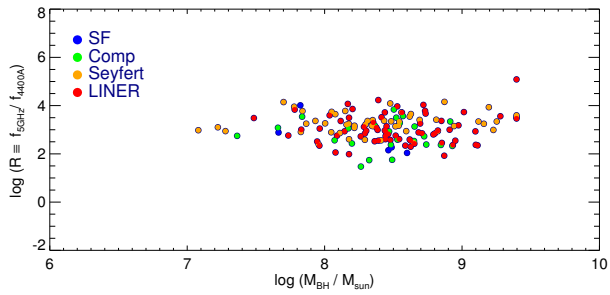


**Figure 6.12:** Black hole mass versus radio loudness for some selected galaxy samples (top panel) and for the Effelsber sample alone, divided by spectral types (bottom panel).

## 6. GALAXY EVOLUTION ACROSS OPTICAL EMISSION-LINE DIAGNOSTIC DIAGRAMS

---

downsizing (less massive galaxies evolve in a longer interval of time). It is interesting to notice that the black-hole mass distribution for the Effelsberg sample (and even clearly for the parent sample, because of a much better statistics) points to a transition from low-metallicity star-forming galaxies to composites and LINERs, where the latter are found to be the galaxies harboring the most massive black holes. However, one can notice that high black-hole mass values do not cluster in any particular region of the diagnostic diagram.

Fig. 6.12 shows the  $M_{BH} - R$  plane. The upper panel shows that the sample is mostly consistent with broad-line radio loud galaxies. The lower panel shows that the four spectral classes are almost equally spread in. The least radio-loud objects are composite galaxies, while AGNs (Seyferts, LINERs) have the highest BH masses.



**Figure 6.13:** Optical SDSS images of the star-forming galaxies.

### 6.3.5 Optical and radio morphologies

The spectroscopic surveys find a link between emission type and Hubble type. HII-emission regions tend to be in late type Spirals, including lower luminosity galaxies. LINERs and Seyferts tend to inhabit early-type spirals and to avoid low luminosity galaxies. The radio morphology can also give important hints on the evolutionary stage of the galaxy. Under precise assumptions, the extension of the lobes and their shape can be used to estimate the “AGN age” (200). The presence of the jets in the radio images, on the other hand, helps us constraining the cases where the AGN feedback can act to influence star formation.

The objects in the Effelsberg survey are mostly unresolved ( $\sim 70\%$ ) at FIRST res-

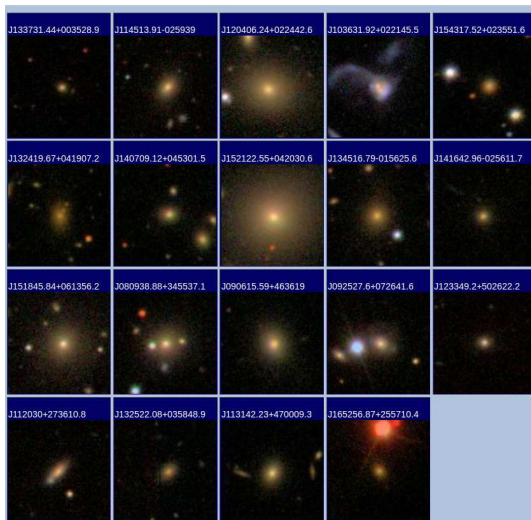


**Figure 6.14:** Optical SDSS images of the composite galaxies.

olutions. The resolved ones show extended radio lobes, and are almost exclusively classified as LINERs. In particular, I find 21 galaxies (18%) showing lobes or jets in FIRST images, and 12 of them are LINERs according to the [NII]-based emission-line diagnostic diagram (see Tab. 6.2). The rest are classified as Seyferts (6 galaxies) or composites (3 galaxies). A significant number of sources (15) show less clear signs of extended emission (e.g. they have elongated structure, but no lobes). These are again mostly LINERs (11 in total). LINERs showing extended features is in agreement with the fact that their radio spectra are humped and peak in the 6 cm range. 6 galaxies show multiple point sources in the radio images. This could be either due to the presence of bright dense star-forming regions (e.g. in case of starburst galaxies) or to the presence of an unrelated source of radio emission (e.g. another galaxy). SDSS images of the 1.4-GHz bright sample, the only images available for these objects given the intermediate redshift range, do not show peculiar morphologies except for 3 post-merger cases and 5 galaxies showing traces of a possible interaction with neighboring galaxies. Therefore, a detailed analysis of the optical morphology of the Effelsberg survey is not

## 6. GALAXY EVOLUTION ACROSS OPTICAL EMISSION-LINE DIAGNOSTIC DIAGRAMS

---

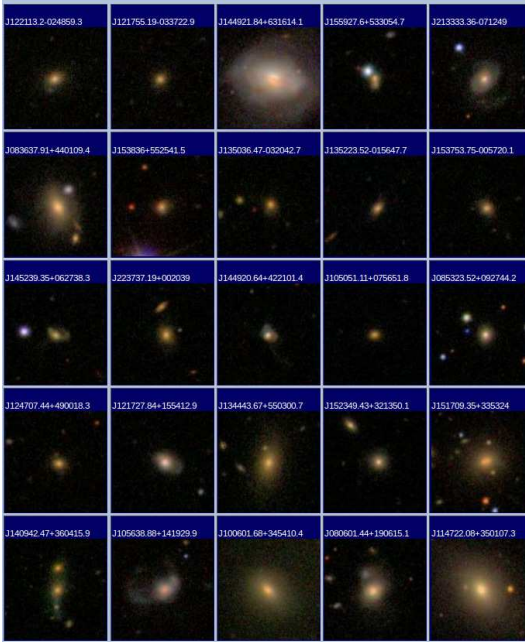


**Figure 6.15:** Optical SDSS images of some Seyfert galaxies.

presented. However, I notice that galaxies with extended features as lobes and jets show lenticular (S0) and elliptical (E) morphology. Often, it is not possible to distinguish between the two.

The images from SDSS illustrate the optical morphology of the radio-emitting star-forming galaxies (Fig. 6.13), composites (Fig. 6.14), Seyfert galaxies (Fig. 6.15) and LINERs (Fig. 6.16). Star-forming galaxies are in general blue, and the galaxy color gets progressively redder in the other spectral types. Only a few galaxies are close enough ( $z \sim 0.05$ ) for their morphology to be determined by eye. Merging and interactions in the upper part of the star-forming sequence of the diagnostic diagrams of the parent sample are visible, as well as post-mergers in the [OIII]-Seyfert emitters. Unfortunately, the low-metallicity starbursts of the Effelsberg sample are under-represented, due to

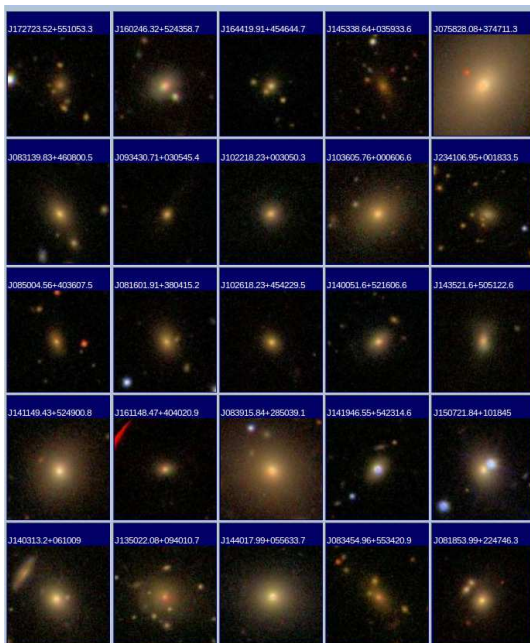


**Figure 6.16:** Optical SDSS images of some LINER galaxies.

the 1.4-GHz flux cut. Only 3 galaxies are found in this region, and one shows a clear sign of recent merging activity. It might be that Seyferts belonging to the green beans class are more abundant in the Effelsberg sample, and I count 19 candidates, i.e. those objects with stellar-velocity mismeasurements. Some of them show again post-merger signs, but their colors are redder than the ones of galaxies placed in the SF region.

## 6. GALAXY EVOLUTION ACROSS OPTICAL EMISSION-LINE DIAGNOSTIC DIAGRAMS

---

### 6.4 Discussion

#### 6.4.1 Optical and radio emission in galaxies

The radio continuum contributes of the bolometric luminosity of normal galaxies (186). Their radio emission is in the form of synchrotron radiation from relativistic electrons and free-free emission from HII regions. AGN with strong optical emission lines of high-ionization potential species are predominantly powerful in radio (57). The explanation for the different host properties and observational biases while considering low-/high-redshift galaxy samples can be researched in the downsizing scenario. Galaxies placed at higher redshifts are more massive and host massive black holes that accrete producing powerful jets. These are easily detected in the radio domain, while low-redshift radio galaxies host mainly low mass black holes where only weak jets originate. The question whether radio and optical emission are related in such a way that they originate from the same physics, still needs to be answered. While radio emission mostly arises from the accreting black hole at the center of the galaxy, optical emission is prominent in star-forming galaxies. Studying the combined optical and radio emission of normal galaxies and AGN help us constraining their origin, and the conditions under which they are present in a particular stage of the galaxy life-time.

Vitale et al. (73) have shown that the radio luminosity at 20 cm progressively increases from star-forming galaxies to Seyferts and LINERs. At the same time, the H $\alpha$  luminosity - a tracer of star-formation activity - decreases in the same direction. This first indicates that strong HI emission is a characteristic sign of recent star-formation, thus of the youth of a galaxy, while radio emission appears as a “later” feature in massive and red ellipticals. However, star-formation can be important in strong radio-emitters as well. Though the Effelsberg sample mostly counts AGNs, the star-forming region of the diagnostic diagrams still contains a few examples of radio emitters (both radio quiet and radio loud). For these galaxies, it is more challenging to disentangle the origin of the radio emission. Radio emission could be due to SNe explosions, originating in the star-forming region of the galaxies after the first bursts of star formation, or powered by a hidden AGN. In this case, the AGN feedback might act to compress the gas, inducing star-formation (positive feedback).

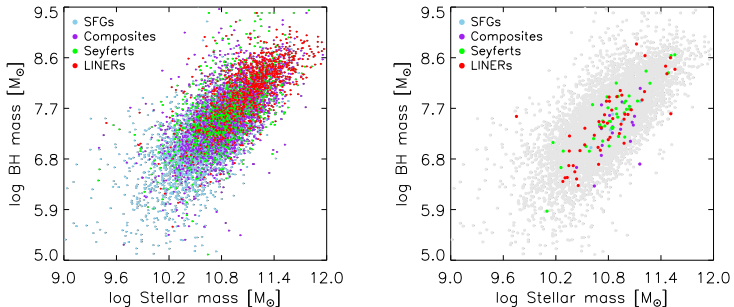


**Figure 6.17:** Correlation between stellar mass and BH mass of the parent sample (left panel) and the Effelsberg sample (right panel). Colors indicate the spectral classes. On the right panel, the grey circles indicate the parent sample. Masses are in solar units.

#### 6.4.2 $M_{BH} - M_{bulge}$ correlation

Studies on host-dominated AGNs suggest that AGNs are more likely to be hosted in massive galaxies (62, 201, 202), though Aird et al. (131) claim that the trend is due to the Eddington-ratio distribution: a higher fraction of AGNs are detected in massive hosts as they are intrinsically more luminous. Vitale et al. (62) extend the Kauffmann et al. (201) analysis to higher redshifts and they show that at intermediate redshift AGN hosts present an average logarithmic stellar mass  $M_*/M_\odot > 10.2$ . The metallicity sequence along the left branch of the distribution in the [NII]-based diagram (103, 201) is thus also a stellar mass sequence. This means that, by selecting galaxies from the optical-radio domain, we exclude galaxies with less massive hosts (see Fig.1 in 73).

The question arises whether the stellar mass is always related to the mass of the black hole. The presence of a bulge or a pseudobulge<sup>1</sup> could make the relation not clear. In Fig. 6.17, the correlation between average stellar mass and BH mass of the parent sample (left panel) and the Effelsberg sample (right panel) is shown. Stellar masses have been calculated from the galaxy mass to light ratio, and are listed in the SDSS DR7. The star-forming galaxies appear to have lower stellar and BH masses compared

<sup>1</sup>Bulges - dense groups of stars find at the center of galaxies, around their nuclei - whose properties are more similar to spiral galaxies than elliptical galaxies. The latter are addressed as “classical bulges”.

## 6. GALAXY EVOLUTION ACROSS OPTICAL EMISSION-LINE DIAGNOSTIC DIAGRAMS

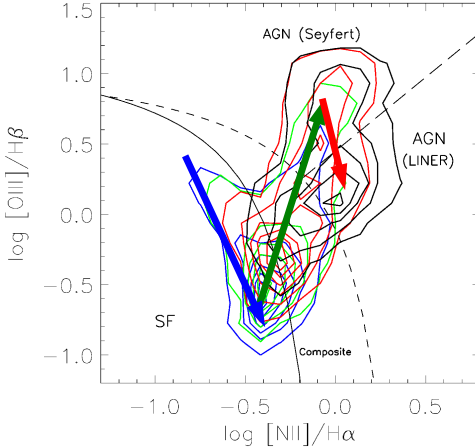


**Figure 6.18:** Sketch of galaxy evolution across the [NII]-based diagnostic diagram. Color contours represent subsamples of the parent sample with increasing values (blue, green, red and black) of the ratio between radio luminosity and luminosity of the  $\text{H}\alpha$  line as in (73). The arrows represent the trend of a possible galaxy evolution from star-forming galaxies to Seyferts and LINERs.

to AGNs. The distribution shows a progressive increase in both BH masses and stellar masses for composites, Seyferts and LINERs. The Effelsberg sample, due to a much lower statistics, does not show a clear trend. The correlation between stellar and BH mass could be interpreted as the more massive and more metallic (with higher  $Z$ ) galaxies being the ones where the AGN was earlier “switched on” and quenched star formation. This consideration does not include Narrow-Line Seyfert 1 galaxies (NLS1s), which are anyhow very rare objects. NLS1s are a class of AGNs having all the properties of type 1 Seyfert galaxies but show peculiar characteristics, including the narrowest Balmer lines, strongest Fe II emission, and extreme properties in the X-rays.

### 6.4.3 An evolutionary sequence in the BPT diagram?

The collection of the Effelsberg data aims at probing galaxy evolution in radio emitters that are classified as star-forming, composite, Seyfert and LINER galaxies in the optical

emission-line diagnostic diagrams, by looking at their combined optical-radio properties. In particular, I search for a flattening of the spectral index along the composite-AGN sequence of the diagnostic diagrams. This sequence was first noticed in Vitale et al. (62, 73). A flattening of the spectral index is expected due to the presence of compact nuclei, or jet emission, that could indicate AGN activity as mechanism that shuts star formation down in the host galaxy. I am interested in testing a scenario where the end of the star-forming sequence represents a turnover point in galaxy evolution, i.e. the start of the quasar phase, which leads to the color and morphological transformation of the hosts, and the transition from the active blue cloud to the “dead” red sequence. As a support to similar theories, some research has been already conducted on separated optical and radio samples. Of special interest is the study of radio-loud sources, classified as FRI and FRII. FRI sources present radio emission that peaks close to the nucleus and jet emission that fades with distance from the center. FRII sources present bright radio lobes and highly collimated jet emission on  $\sim 100$  kpc scales. FRI sources dominate the population of radio emitters at low radio power and low redshifts, while more powerful radio galaxies are usually FR II systems placed at higher redshift. This study is based on the further evidence that Seyferts appear to be mostly luminous high-excitation systems, related to some degree to FRII radio sources, while LINERs, which are particularly bright in the radio and accrete at lower rates (low excitation systems), are FRI and possibly a “later” stage of radio evolution. This might be due to the fact that FRI and FRII have been hypothesized to be AGNs with different BH accretion rates (20).

From optical studies, LINERs are mostly found in massive early type galaxies that do not show any signs of star formation. Therefore, LINER activity might be the “smoking gun” of highly effective suppression mode (radio mode) AGN feedback (28). So the question here addressed is: are LINERs the last stage of the galaxy evolution? Though the nature of LINERs is still matter of debate and some authors have shown that LINERs are, at least in some cases, triggered by old stars rather than AGN (99, 203), in Vitale et al. (73) I show that radio LINERs are mainly weak AGN. Therefore, I consider them as belonging to the AGN family.

To consider the hypothesis of a galaxy evolution across the diagnostic diagrams, I recall the evidence I have shown you so far. Fig. 6.6 shows the spectral index ( $\alpha_{[4.85-10.45\text{GHz}]}$ )

## 6. GALAXY EVOLUTION ACROSS OPTICAL EMISSION-LINE DIAGNOSTIC DIAGRAMS

---

distribution in the BPT diagram. The sample comprises metal-rich star-forming galaxies, composite galaxies, and many AGN. The presence in this diagram of a sequence of galaxies with flat or inverted spectra is a hint of increased nuclear activity along the same. The sequence could be explained as an increase in the strength of the ionizing field of the galaxies, due to disk accretion. LINERs represent a different class of shock-ionized objects, and their emission is not always triggered by AGNs. However, radio signature of AGNs are present in metal-rich star-forming galaxies as well. I find three possible scenario to explain flat-spectra radio sources in the star-forming region of the diagnostic diagram:

- The enhancement of star formation might be triggered by the AGN, which induces gas compression and acts as the so-called positive feedback.
- The sources host young (just recently switched on) AGNs, and the star formation in the galaxies has not yet been suppressed. This could be the case for strong and widespread star formation, where the timescale for it to die out could be several hundred Myr, potentially as longer than the lifetime of the AGN. If AGN are recurrent phenomena, it might be a stop-start-stop-start process in the AGN that progressively slows down the star formation throughout the galaxy.
- AGNs are not strong enough to suppress the star formation entirely
- There is no link between AGN and star formation suppression. In this latter case, steep-spectra radio galaxies would represent counter-examples to the hypothesis.

Seyfert and LINERs lie in older hosts. In these cases, AGN activity could lead to a negative feedback instead, where powerful jets and/or galactic superwinds blow the gas away and prevent or induce star-formation.

### 6.4.4 Evolutionary scenarios

One of the most important achievement in modern astronomy would be to set a simple and universally valid galaxy evolutionary scenario that explains how blue star-forming galaxies turn into red passively-evolving systems. While some models take into account this kind of transition and the necessity of a mechanism to truncate star formation (48), there is still the need of observational confirmations to test theories. Some of the current standard models of galaxy evolution (204, 205) rely on major mergers and/or

interactions to trigger both star formation and AGN activity in two merging late-type galaxies. Then, the system relaxes and forms an early-type galaxy hosting a radio AGN.

The importance of mergers at  $z < 1$  has been often neglected before the discovery of ULIRGs, and the “green pea” class of objects (199), which may represent the downscaled version of high-redshift merging galaxies. The low stellar-mass and low-metallicity galaxies merging at  $z < 1$  may well represent the beginning of an evolutionary sequence traced by the diagnostic diagrams at  $z < 0.4$  (Fig. 6.18). Along the star-forming sequence of the BPT diagram and up to the composites-AGN region, the galaxy total stellar mass has been found to increase (62), probably due to the presence of gas brought up by mergers/interactions. At the same time, the BH is fed with the same material and its mass increases.

It has been suggested that at radio wavelengths the two major radio AGN populations - the powerful ( $L_{20\text{cm}} > 10^{25}$  W/Hz) high-excitation, and the weak ( $L_{20\text{cm}} < 10^{25}$ ) low-excitation radio AGNs - represent two earlier and later stages of massive galaxy evolution (17, 102). As a support to this hypothesis, a clear dichotomy is found between the properties of low-excitation (mostly LINERs) and high-excitation (Seyferts) radio AGNs. The hosts of the first have higher stellar masses, redder optical colors, and higher black holes masses, but accrete at lower rates. On the other hand, the high-excitation radio AGNs contain more gas, have lower stellar masses, bluer optical colors (consistent with the green valley), and lower mass black holes that accrete at higher rates. This evidence supports the idea of a co-evolution between BH and surrounding galaxy. A question arises whether the phase of efficient accretion is due only once during a galaxy life time, or it is a periodic event that occurs when there is new gas available (i.e., interactions, fly-by and minor mergers). Ciotti et al. (206) have found that the AGN feedback could be either a continuous or periodic process. Nandi et al. (207) have conducted a study on radio galaxies presenting morphologies with multiple lobes (two or three couples). The authors argue that these peculiar morphologies are the result of multiple phases of intense accretion, each one generating a couple of jets and lobes, and being potentially able to influence star formation.

While there are some studies aiming at explaining the most latest stages of galaxy evolution, observational proofs of the transition from star-forming to Seyferts are still missing in the radio-optical regime. I speculate that the chance of having a positive or

## 6. GALAXY EVOLUTION ACROSS OPTICAL EMISSION-LINE DIAGNOSTIC DIAGRAMS

---

negative AGN feedback may depend on the gas density in the galaxy disk and/or the scale we are considering. This is, at smaller scales, closer to the black hole, powerful jets and outflows compress the gas and induce positive feedback (star formation), while further away the gas is more diluted and can rather be swept away (negative feedback, quench of the star formation).

### 6.5 Conclusions

The collection of the Effelsberg data aims at probing galaxy evolution in radio emitters that are classified as star-forming, composite, Seyfert and LINER galaxies in the optical emission-line diagnostic diagrams, by looking at their combined optical-radio properties. I have searched for a flattening of the spectral index along the composite-AGN sequence of the diagnostic diagrams. This was done to test a scenario where the end of the star-forming sequence represents a crucial point in galaxy evolution, i.e. the start of the quasar phase, which leads to the color and morphological transformation of the hosts. The analysis of the spectral index distribution, combined with the information on the radio morphology (low resolution, from FIRST survey at 1.4 GHz), have here been presented to investigate the nature of the sources along the composite-AGN branch, their active state, and the chance to spot an evolutionary sequence. Conclusions are the following:

- The objects form a sequence of flattening spectral indexes that extend from the high-metallicity end of the star-forming sequence in the [NII]-based diagnostic diagram, to the Seyfert region, with the highest  $\alpha_{[4.85-10.45\text{GHz}]}$  values found among the AGN. The sequence crosses the composite region and goes along the Seyfert/LINER division line. It is consistent with a progressive hardening of the ionizing field of the galaxy, due to intense nuclear activity.
- The spectral curvature distribution shows the difference in the Seyfert and LINER spectra, with Seyfert having flatter and LINER more humped (5-GHz peaked) spectra. This suggests that the high frequency radio-emission of Seyferts along the division line between Seyferts and LINERs in the [NII]-based diagram is dominated by (milli)arcsecond sized radio core components, whereas the emission of LINERs is dominated by larger source components. Those could be due to

(milli)arcsecond sized components associated with nuclear jets, compact working points in radio lobes, or very compact wind/shock regions that are bright in the radio domain.

- The spectral index flattening seems to be significant for sources that show mixed (star formation/AGN) contributions to optical line emission, and have been hypothesized to transit from the blue cloud to the red sequence (passive galaxies). Flattening may extend from high-metallicity star-forming galaxies and progress till LINERs and passive galaxies, after morphological and color transformation. In this respect, nuclear radio activity and AGN feedback may have a role in first enhancing (in spectroscopically-classified star-forming galaxies) and then shutting down star formation in the hosts, to build up the galaxy color bimodality.
- Results are consistent with the findings that star-forming galaxies, composites, Seyferts and LINERs show progressively old stellar populations, redder colors, and higher black hole masses. The presence of merging and post-merging features in galaxies belonging to the star-formation branch strengthens the scenario of merging-triggered star formation at intermediate redshift values, and sets it at the beginning of the evolutionary sequence.

A larger galaxy sample and high-resolution radio maps would help to further constrain the nature of the radio-emitters along the flattening sequence in the [NII]-based diagram, and catch the AGN-feedback in action in sources that are just leaving the star-forming galaxies branch.

## 6. GALAXY EVOLUTION ACROSS OPTICAL EMISSION-LINE DIAGNOSTIC DIAGRAMS

---

# 7

## Final discussion and conclusions

In this thesis work, I explore one of the most debated problems of modern astrophysics, namely the role and impact of AGN feedback on galaxy evolution. With data drawn from different archive datasets, both at optical (zCOSMOS, SDSS) and radio (FIRST) wavelengths, and with the complementary information coming from new radio observations at the Effelsberg telescope, I have conducted an extensive multi-wavelength study of star-forming galaxies and AGN-hosts properties. The main aim of my PhD work was to investigate and better understand the connection between optical and radio emission in active galaxies, probe scenarios that implement AGN feedback to explain the evolution of galaxy properties, and search for observational evidence of a sequence that links all star-forming galaxies, Seyferts and LINERs as subsequent stages of galaxy evolution.

### 7.1 Advantages of combined multi-wavelength studies

I have stressed the importance of studying galaxies at different wavelengths, and in particular in the radio and optical domain. When multi-wavelength data are available, a more complete picture of galaxies and their evolution can emerge, since different phenomena (e.g. star formation, dust emission, SN explosions, black hole accretion) dominate the galaxy continuum emission at specific wavelengths. A combined study of optical and radio properties of AGNs and their hosts is of particular interest, given the large amount of public data available and the large sky coverage of some surveys, which allow statistically significant interpretations. Under the assumption that AGNs

## 7. FINAL DISCUSSION AND CONCLUSIONS

---

play a role in turning blue spiral galaxies into passive ellipticals, a careful analysis of radio spectra and images helps with the identification of nuclear activity. Galaxy gas content, mass, star formation rate, color, and morphology are well studied at optical wavelengths. Fig. 7.1 illustrates the galaxy stellar mass distribution (inferred from SDSS photometry) of the cross-matched optical-radio sample. Each spectroscopic galaxy class has an average stellar mass that increases from the star-forming region to the Seyfert and LINER regions of the diagram, pointing out a striking trend that deserves further investigation.

### 7.2 Optical and radio emission in intermediate-redshift galaxies

The optical-radio cross-matched sample of normal galaxies and AGN hosts mainly selects AGN and metal-rich star-forming galaxies (see Chapter 5). The selection includes some quasars, which are particularly bright at radio wavelengths. An object included in the optical-radio cross-matched sample does not necessarily show correlated emission at these wavelengths. In order to be detected, radio emission from my galaxy sample (mainly from the nucleus) must be strong, without outshining the optical emission from the host. For example, blazars<sup>1</sup> have a very bright core component, due to the observer's line of sight pointing directly at the unobscured center of the galaxy, and this core component is usually some orders of magnitude brighter than the emission from the host galaxy. Extremely bright AGNs and powerful radio galaxies are therefore mostly excluded from cross-matched optical-radio samples. Powerful radio galaxies and quasars are anyhow less common at low and intermediate redshifts, due to selection effects.

Optical and radio emission in galaxies seem to correlate in particular types of objects. Galaxies in the optical-radio cross-matched sample show signs of significant optical and radio activity. They have high stellar masses ( $M_* > 10^{10} M_\odot$ ) and black hole masses ( $M_{BH} > 10^6 M_\odot$ ), high metallicity (inferred from the  $\log [\text{NII}]/\text{H}\alpha$  ratio, which is usually greater than  $-0.5$ ), and have an older stellar content ( $\gtrsim 2$  Gyr from the last bursts of star formation, Tab. 8.1) when compared to metal-poor star-forming galaxies.

---

<sup>1</sup>AGN with a relativistic jet that is pointing in the direction of the observer.

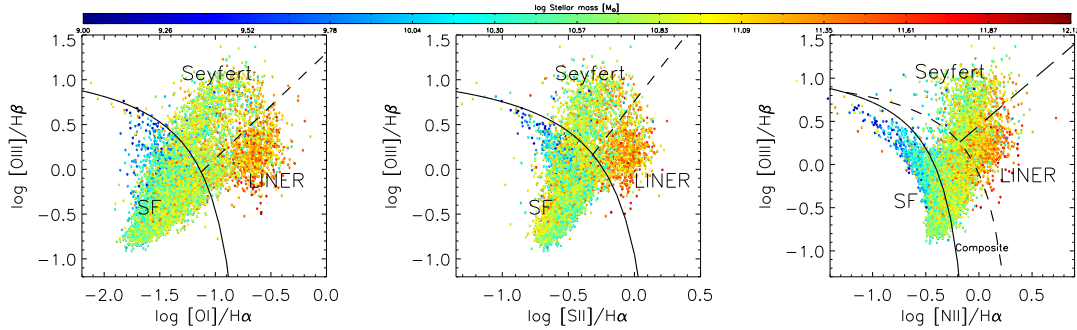


**Figure 7.1:** Average stellar masses of the parent (SDSS-FIRST cross-match) sample as a function of spectral classes in the optical emission-line diagnostic diagrams. The color bar indicates  $M_*$  in solar masses.

## 7. FINAL DISCUSSION AND CONCLUSIONS

---

Following the  $M_{BH}-M_{bulge}$  relation, massive galaxies harbor a massive black hole at their centers. The optical-radio connection may be explained in two ways. First, for the most powerful sources, the AGN is largely responsible for the radio emission. Inducing gas turbulence and positive feedback, the AGN could cause some star-formation bursts and the optical emission from the surrounding galaxy. Second, low-mass and low-metallicity galaxies (blue distribution in Fig 7.1) are most likely in an earlier stage of gas accretion and mass build-up, with too low black hole masses for the AGN phenomenon to show up. In these cases, a significant contribution to the sub-mJy radio emission come from SNe explosions.

Star formation is visible at optical, as well as ultraviolet and IR wavelengths. Star formation can occur independently from AGN activity (e.g. in case of quiescent black holes). If star formation is not related to AGN activity, we might be observing a phase of galaxy evolution where there is enough gas in the galaxy to trigger the creation of new stars (e.g. after mergers or encounters) and the AGN is too weak to quench the star formation. As known, the same gas fuels black hole accretion, and the two phenomena can co-exist till black hole accretion prevails. As a support to this scenario, it has been found that star formation and black hole activity can be present at the same time in massive high-redshift galaxies (208), and the two peak with a time delay of about 1 Gyr (28).

My conclusion is that optical and radio emission in intermediate redshift galaxies could be related due to the presence of nuclear activity. There is growing evidence of nuclear outflows in galaxies, which might be signs of AGN feedback inducing star formation. This is done via gas compression and cooling, since outflows can transport cooler gas and dust to the outer regions of the galaxy (67). If this is proven right, positive AGN-feedback could be addressed as a phase of galaxy evolution where optical and radio emission are actually triggered by the same mechanism. Negative AGN-feedback is equally important in regulating star formation in the host, and it is discussed in the next section.

### 7.3 AGN feedback

Although hints of a possible positive AGN-feedback exist, further studies and strong observational evidence are still needed. Literature works seem to be equally in favor of

positive and negative feedback, and here I speculate how they could both occur in the same galaxy, at two different stages of galaxy evolution.

Positive feedback might happen in earlier stages of galaxy evolution. It has been observed in some quasars, which undergo jet-induced star formation (209). There is increasing evidence that molecular outflows can be responsible for inducing star-formation on short scales (e.g. nuclear). If so, we should be able to observe radio emission from nuclear starburst. In these cases, radio emission is not only due to SNe explosions and free-free emission, but rather shows a significant contribution from the nuclear region. Evidence of radio-bright, flat-spectrum sources were discussed in Chapter 6. While observational signatures of positive-AGN feedback mainly consist of nuclear molecular outflows, bow shocks, and jets, proofs of negative-AGN feedback are rather “indirect”. Negative feedback has been hypothesized to be due to heating and photo-dissociation of molecular gas by the hot AGN accretion disk (209). Quenching of star formation in galaxies has never been observed directly, but AGN-host properties have been found to change subsequently to nuclear activity. For example, stellar population become progressively older after the quasar phase, and metallicity increases accordingly (see Chapter 4). The negative feedback happens either when radiation pressure sweeps the gas reservoir away (quasar mode) or when it prevents gas cooling (radio mode).

In my work, I find indication of negative feedback by looking at the aging of the stellar populations in the AGN hosts (see Chapter 4). Based on this evidence, positive feedback could likely happen when a galaxy has accreted enough gas to initiate its quasar phase. After bursts of star formation, nuclear activity prevails and the feedback turns “negative”.

## 7.4 A unified galaxy-evolutionary sequence

The question is now: does AGN-feedback occur in all galaxies that are massive enough to harbor a black hole at their center? If the  $M_{BH}-M_{bulge}$  relation is genuine, all massive galaxies should host a super-massive black hole, which starts accreting at some point of the galaxy evolution. AGN feedback has been implemented in many theoretical models to explain the observed galaxy luminosity function. Moreover, feedback has been hypothesized to be responsible of the color bimodality, and the transformation of blue spirals into red ellipticals. The findings described in Chapter 6 suggest a transition

## 7. FINAL DISCUSSION AND CONCLUSIONS

---

### A Sequence of Events for AGN Feedback in the formation of early-type galaxies

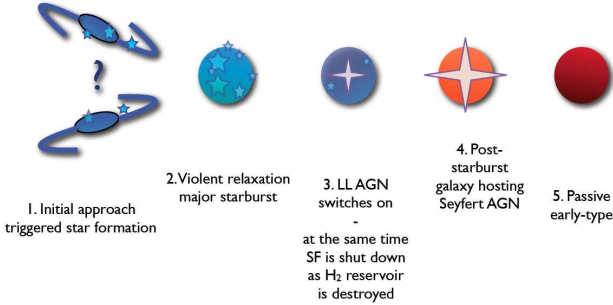


**Figure 7.2:** Possible scenario of the evolution from blue and active to red and passive galaxy. “LLAGN” stands for Low-Luminosity AGN. Credits: K. Schawinski.

from blue star-forming galaxies (Fig. 7.1, right panel, on the left-side of the emission-line diagnostic diagram) to composites (middle) and AGN (right-side). This trend is supported by the findings of Chapter 5 (radio power increases and luminosity of the H $\alpha$  line decreases from star-forming to LINER galaxies) and the results in Chapter 4 (aging of the stellar populations). In particular, the [NII]-based diagnostic diagram of Chapter 6 (Fig. 6.6) highlights a sequence of radio spectral index flattening, which is consistent with the rise of nuclear activity in the galaxies of the optical-radio sample (a possible AGN feedback?). Galaxies could represent different stages of galaxy evolution, starting with mergers and galaxy encounters, and ending in LINERs and passive types. The evolutionary scheme in Fig. 7.2 illustrates a merger-driven sequence of events that leads to the color and morphological transformation via AGN feedback, and is consistent with my findings.

## 7.5 Outlook

The next step in this research work would be to further investigate the sources along the spectral index flattening sequence (Fig. 6.6) with a larger galaxy sample. These

radio galaxies might represent the “transiting” spectral and morphological kinds in the emission-line diagnostic diagrams, namely the objects that possibly evolve into passive galaxies. Radio interferometry studies could reveal jets and outflows morphologies, and signs of the latter interacting with the star-forming regions of the galaxy. Spectral indexes are also essential to estimate the ages of the extended radio features, and the time since the black hole is in its active state. With these data in hand, it is possible to test the role of AGN feedback in galaxy evolution.

The search for AGN could benefit from the complementary analysis of individual galaxies with advance spectroscopic techniques (e.g. Integral Field Unit, which allows multiple spectra of different galaxy regions) or from analyses at other wavelengths. The X-ray domain can identify nuclear activity because the luminous, compact X-ray emission ( $L_{2-10\text{keV}} > 10^{42} \text{ ergs s}^{-1}$ ) is an almost certain indicator that there is an AGN (210, 211, 212, 213), given the extremely low contribution from star formation to the overall emission at these frequencies. X-ray observations have been found to be very efficient in revealing accreting black holes in galaxies that were not classified as AGN from the analysis of optical data (214). The discovery of the radio-FIR correlation pointed out that AGN or star formation contributions to galaxy emission can be studied in the FIR domain as well. Ultra Luminous Infra Red Galaxies (ULIRGs) and Luminous Infra Red Galaxies (LIRGs) have very high IR luminosity, and many ULIRGs are merging galaxies, which possibly places them at the beginning of the evolutionary sequence. Finally, since the quenching of star-formation and the possibly related AGN feedback are thought to play a crucial role in galaxy evolution at  $z \sim 2$ , it would be worthwhile to further enlarge the redshift range I consider in these studies to higher  $z$  values.

## 7. FINAL DISCUSSION AND CONCLUSIONS

---

# References

- [1] B. VOLLMER. *The Influence of Environment on Galaxy Evolution*, page 207. 2013. 2
- [2] B. W. CARROLL AND D. A. OSTLIE. *An Introduction to Modern Astrophysics*. 1996. 4
- [3] I. STRATEVA, Ž. IVEZIĆ, G. R. KNAPP, V. K. NARAYANAN, M. A. STRAUSS, J. E. GUNN, R. H. LUPTON, D. SCHLEGEL, N. A. BAICALL, J. BRINCKMANN, R. J. BRUNNER, T. BUDAVÁRI, I. CSABAI, F. J. CASTANDER, M. DOL, M. FUKUGITA, Z. GYÖRÝ, M. HAMABE, G. HENNESSY, T. ICHIKAWA, P. Z. KUNSZT, D. Q. LAMB, T. A. MCKAY, S. OKAMURA, J. RACUSIN, M. SEKIGUCHI, D. P. SCHNEIDER, K. SHIMASAKU, AND D. YORK. **Color Separation of Galaxy Types in the Sloan Digital Sky Survey Imaging Data**. *AJ*, 122:1861–1874, October 2001. 4, 16
- [4] G. KAUFFMANN, T. M. HECKMAN, C. TREMONTI, J. BRINCKMANN, S. CHARLOT, S. D. M. WHITE, S. E. RIDGWAY, J. BRINCKMANN, M. FUKUGITA, P. B. HALL, Ž. IVEZIĆ, G. T. RICHARDS, AND D. P. SCHNEIDER. **The host galaxies of active galactic nuclei**. *MNRAS*, 346:1055–1077, December 2003. 4, 12, 16, 18, 23, 37, 46, 47, 48, 49, 50, 61, 62, 82, 91
- [5] I. K. BALDRY, K. GLAZEBROOK, J. BRINCKMANN, Ž. IVEZIĆ, R. H. LUPTON, R. C. NICHOL, AND A. S. SZALAY. **Quantifying the Bimodal Color-Magnitude Distribution of Galaxies**. *ApJ*, 600:681–694, January 2004. 4, 16, 47
- [6] M. L. BALOGH, I. K. BALDRY, R. NICHOL, C. MILLER, R. BOWER, AND K. GLAZEBROOK. **The Bimodal Galaxy Color Distribution: Dependence on Luminosity and Environment**. *ApJ*, 615:L101–L104, November 2004. 4, 16
- [7] D. W. HOGG, M. R. BLANTON, J. BRINCKMANN, D. J. EISENSTEIN, D. J. SCHLEGEL, J. E. GUNN, T. A. MCKAY, H.-W. RIX, N. A. BAICALL, J. BRINCKMANN, AND A. MEKSHIN. **The Dependence on Environment of the Color-Magnitude Relation of Galaxies**. *ApJ*, 601:L29–L32, January 2004. 4, 16
- [8] R. S. SUTHERLAND, G. V. BICKNELL, AND M. A. DOPTA. **Shock excitation of the emission-line filaments in Centaurus A**. *ApJ*, 414:510–526, September 1993. 9, 78
- [9] I. EVANS, A. KÓRATKAR, M. ALLEN, Z. TSVETANOV, AND M. DOPTA. **Excitation Mechanism of Extended Emission-Line Regions in Active Galaxies**. In B. M. PETERSON, F.-Z. CHENG, AND A. S. WILSON, editors, *IAU Colloq. 159: Emission Lines in Active Galaxies: New Methods and Techniques*, 113 of *Astronomical Society of the Pacific Conference Series*, page 386, 1997. 9
- [10] R. ANTONUCCI. **Unified models for active galactic nuclei and quasars**. *ARA&A*, 31:473–521, 1993. 9, 22
- [11] P. PADOVANI AND P. GIOMMI. **A Sample-Oriented Catalogue of Bi-Lacertae Objects**. *MNRAS*, 277:1477, December 1995. 9
- [12] D. E. OSTERBROCK. *Astrophysics of gaseous nebulae and active galactic nuclei*. 1989. 10, 61, 77, 145
- [13] T. M. HECKMAN. **An optical and radio survey of the nuclei of bright galaxies - Activity in normal galactic nuclei**. *AE&A*, 87:152–164, July 1980. 10
- [14] L. K. HUNT AND M. A. MALKAN. **Circumnuclear Structure and Black Hole Fueling: Hubble Space Telescope NICMOS Imaging of 250 Active and Normal Galaxies**. *ApJ*, 616:707–729, December 2004. 10
- [15] K. I. KELLERMANN, R. SRAHEK, M. SCHMIDT, D. B. SHAFFER, AND R. GREEN. **VLA observations of objects in the Palomar Bright Quasar Survey**. *AJ*, 98:1195–1207, October 1989. 10
- [16] B. L. FANAROFF AND J. M. RILEY. **The morphology of extragalactic radio sources of high and low luminosity**. *MNRAS*, 167:31P–36P, May 1974. 10
- [17] M. J. HARDCASTLE, D. A. EVANS, AND J. H. CROSTON. **The X-ray nuclei of intermediate-redshift radio sources**. *MNRAS*, 370:1893–1904, August 2006. 11, 121
- [18] M. J. LEDLOW AND F. N. OWEN. **A 20 CM VLA Survey of Abell clusters of galaxies. 4: The radio sample and cluster properties**. *AJ*, 109:853–873, March 1995. 11
- [19] F. GOVONI, R. FALOMO, G. FASANO, AND R. SCARPA. **The optical properties of low redshift radio galaxies**. *AE&A*, 353:507–527, January 2000. 11
- [20] D. KOZIEL-WIERZBOWSKA AND G. STASIŃSKA. **FR II radio galaxies in the Sloan Digital Sky Survey: observational facts**. *MNRAS*, 415:1013–1026, August 2011. 11, 119
- [21] E. P. SMITH AND T. M. HECKMAN. **Multicolor surface photometry of powerful radio galaxies. II - Morphology and stellar content**. *ApJ*, 341:658–678, June 1989. 11
- [22] S. A. BAUM, E. L. ZIRBEL, AND C. P. O'DEA. **Toward Understanding the Fanaroff-Riley Dichotomy in Radio Source Morphology and Power**. *ApJ*, 451:88, September 1995. 11
- [23] J. A. BALDWIN, M. M. PHILLIPS, AND R. TERLEVICI. **Classification parameters for the emission-line spectra of extragalactic objects**. *PASP*, 93:5–19, February 1981. 12, 13, 37, 45, 48, 59, 92
- [24] S. VILLEUX AND D. E. OSTERBROCK. **Spectral classification of emission-line galaxies**. *ApJS*, 63:295–310, February 1987. 12, 37, 45, 48, 59, 92

## REFERENCES

- [25] L. J. KEWLEY, M. A. DOPITA, R. S. SUTHERLAND, C. A. HEISLER, AND J. TRIVENA. **Theoretical Modeling of Starburst Galaxies.** *ApJ*, **556**:121–140, July 2001. 12, 37, 46, 48, 49, 61, 62, 91
- [26] L. J. KEWLEY, B. GROVES, G. KAUFFMANN, AND T. HECKMANN. **The host galaxies and classification of active galactic nuclei.** *MNRAS*, **372**:961–976, November 2006. 12, 36, 37, 42, 46, 48, 50, 52, 62, 63, 91, 92
- [27] G. KAUFFMANN, T. M. HECKMANN, C. TREMONTI, J. BRINCHMANN, S. CHARLOT, S. D. M. WHITE, S. E. RIDGWAY, J. BRINKMANN, M. FUKUGITA, P. B. HALL, Ž. IVEŽIĆ, G. T. RICHARDS, AND D. P. SCHNEIDER. **The host galaxies of active galactic nuclei.** *MNRAS*, **346**:1055–1077, December 2003. 12, 49
- [28] K. SCHAWINSKI, D. THOMAS, M. SARZI, C. MARASTON, S. KAVIRAJ, S.-J. JOO, S. K. YI, AND J. SILK. **Observational evidence for AGN feedback in early-type galaxies.** *MNRAS*, **382**:1415–1431, December 2007. 12, 47, 63, 91, 119, 128
- [29] F. HAMANN AND G. FERLAND. **Elemental Abundances in Quasistellar Objects: Star Formation and Galactic Nuclear Evolution at High Redshifts.** *ARA&A*, **37**:487–531, 1999. 13
- [30] M. J. REES, H. NETZER, AND G. J. FERLAND. **Small dense broad-line regions in active nuclei.** *ApJ*, **347**:640–655, December 1989. 13
- [31] R. YAN, L. C. HO, J. A. NEWMAN, A. L. COIL, C. N. A. WILLMER, E. S. LAIRD, A. GEORGAKAKIS, J. ARD, P. BARMBY, K. BUNDEY, M. C. COOPER, M. DAVIS, S. M. FABER, T. FANG, R. L. GRIFFITH, A. M. KOEKEMOER, D. C. KOO, K. NANDRA, S. Q. PARK, V. L. SARAJEDINI, B. J. WEINER, AND S. P. WILLNER. **AEGIS: Demographics of X-ray and Optically Selected Active Galactic Nuclei.** *ApJ*, **728**:38, February 2011. 15
- [32] J. MAGORRIAN, S. TREMAINE, D. RICHSTONE, R. BENDER, G. BOWER, A. DRESSLER, S. M. FABER, K. GEBHARDT, R. GREEN, C. GRILLMAIR, J. KORMENDY, AND T. LAUER. **The Demography of Massive Dark Objects in Galaxy Centers.** *AJ*, **115**:2285–2305, June 1998. 15
- [33] L. FERRARESE AND D. MERRITT. **A Fundamental Relation between Supermassive Black Holes and Their Host Galaxies.** *ApJ*, **539**:L9–L12, August 2000. 15
- [34] S. M. FABER, C. N. A. WILLMER, C. WOLF, D. C. KOO, B. J. WEINER, J. A. NEWMAN, M. IM, A. L. COIL, C. CONROY, M. C. COOPER, M. DAVIS, D. P. FINKBEINER, B. F. GERKE, K. GEBHARDT, E. J. GROTH, P. GUHATHAKURTA, J. HARKER, N. KAISER, S. KASSIN, M. KLEINHEINRICH, N. P. KONIDARIS, R. G. KRON, L. LIN, G. LEPPINO, D. S. MADGWICK, K. MEISENHEIMER, K. G. NOESKE, A. C. PHILLIPS, V. L. SARAJEDINI, R. P. SCHLAVON, L. SIMARD, A. S. SZALAY, N. P. VOGT, AND R. YAN. **Galaxy Luminosity Functions to  $z=1$  from DEEP2 and COMBO-17: Implications for Red Galaxy Formation.** *ApJ*, **665**:265–294, August 2007. 16
- [35] M. C. COOPER, J. A. NEWMAN, B. J. WEINER, R. YAN, C. N. A. WILLMER, K. BUNDEY, A. L. COIL, C. J. CONSELICE, M. DAVIS, S. M. FABER, B. F. GERKE, P. GUHATHAKURTA, D. C. KOO, AND K. G. NOESKE. **The DEEP2 Galaxy Redshift Survey: the role of galaxy environment in the cosmic star formation history.** *MNRAS*, **383**:1058–1078, January 2008. 17
- [36] M. MARTIG, F. BOURNAUD, R. TEYSSIER, AND A. DEKEL. **Morphological Quenching of Star Formation: Making Early-Type Galaxies Red.** *ApJ*, **707**:250–267, December 2009. 17
- [37] C. J. CONSELICE, K. BUNDEY, I. TRUJILLO, A. COIL, P. EISENHARDT, R. S. ELLIS, A. GEORGAKAKIS, J. HUANG, J. LOTZ, K. NANDRA, J. NEWMAN, C. PAPOVICH, B. WEINER, AND C. WILLMER. **The properties and evolution of a K-band selected sample of massive galaxies at  $z \sim 0.4-2$  in the Palomar/DEEP2 survey.** *MNRAS*, **381**:962–986, November 2007. 17
- [38] L. CIOTTI AND J. P. OSTRICKER. **Cooling Flows and Quasars: Different Aspects of the Same Phenomenon? I. Concepts.** *ApJ*, **487**:L105, October 1997. 17
- [39] J. BINNEY. **Cooling Flows Or Heating Flows? In** T. REIPRICH, J. KEMPNER, AND N. SOKER, editors, *The Role of Cooling Flows in Galaxies and Clusters of galaxies*, page 233, 2004. 17
- [40] J. SILK. **Ultraluminous starbursts from supermassive black hole-induced outflows.** *MNRAS*, **364**:1337–1342, December 2005. 17
- [41] V. SPRINGEL, T. DI MATTEO, AND L. HERNQUIST. **Black Holes in Galaxy Mergers: The Formation of Red Elliptical Galaxies.** *ApJ*, **620**:L79–L82, February 2005. 17
- [42] D. RICHSTONE, E. A. AJHAR, R. BENDER, G. BOWER, A. DRESSLER, S. M. FABER, A. V. FILIPPENKO, K. GEBHARDT, R. GREEN, L. C. HO, J. KORMENDY, T. R. LAUER, J. MAGORRIAN, AND S. TREMAINE. **Supermassive black holes and the evolution of galaxies.** *Nature*, **395**:A14, October 1998. 17
- [43] A. V. FILIPPENKO AND L. C. HO. **A Low-Mass Central Black Hole in the Bulgeless Seyfert 1 Galaxy NGC 4395.** *ApJ*, **588**:L13–L16, May 2003. 17
- [44] J. SILK AND M. J. REES. **Quasars and galaxy formation.** *A&A*, **331**:L1–L4, March 1998. 17
- [45] D. J. CROTON, V. SPRINGEL, S. D. M. WHITE, G. DE LUCIA, C. S. FRENK, L. GAO, A. JENKINS, G. KAUFFMANN, J. F. NAVARRO, AND N. YOSHIDA. **The many lives of active galactic nuclei: cooling flows, black holes and the luminosities and colours of galaxies.** *MNRAS*, **365**:11–28, January 2006. 17
- [46] D. NARAYANAN, T. J. COX, Y. SHIRLEY, R. DAVÉ, L. HERNQUIST, AND C. K. WALKER. **Molecular Star Formation Rate Indicators in Galaxies.** *ApJ*, **684**:996–1008, September 2008. 17
- [47] A. CATTANEO, S. M. FABER, J. BINNEY, A. DEKEL, J. KORMENDY, R. MUSHOTZKY, A. BABUL, P. N. BEST, M. BRÜGGEN, A. C. FAHIAN, C. S. FRENK, A. KHALATYAN, H. NETZER, A. MAHDANI, J. SILK, M. STERNMETZ, AND L. WISOTZKI. **The role of black holes in galaxy formation and evolution.** *Nature*, **460**:213–219, July 2009. 17, 22

- [48] P. F. HOPKINS, L. HERQUST, T. J. COX, T. DI MATTEO, B. ROBERTSON, AND Y. SPRINGEL. **A Unified, Merger-driven Model of the Origin of Starbursts, Quasars, the Cosmic X-Ray Background, Supermassive Black Holes, and Galaxy Spheroids.** *ApJS*, **163**:1–49, March 2006. 17, 59, 120
- [49] D. B. SANDERS, B. T. SOFFER, J. H. ELIAS, G. NEUGEBAUER, AND K. MATTHEWS. **Warm ultraluminous galaxies in the IRAS survey - The transition from galaxy to quasar?** *ApJ*, **328**:L35–L39, May 1988. 17
- [50] L. C. HO, A. V. FILIPPENKO, AND W. L. W. SARJENT. **A Search for “Dwarf” Seyfert Nuclei. V. Demographics of Nuclear Activity in Nearby Galaxies.** *ApJ*, **487**:568, October 1997. 17
- [51] C. J. MILLER, R. C. NICHOI, P. L. GÓMEZ, A. M. HOPKINS, AND M. BERNARDI. **The Environment of Active Galactic Nuclei in the Sloan Digital Sky Survey.** *ApJ*, **597**:142–156, November 2003. 18
- [52] J. D. SILVERMAN, F. LAMARELLE, C. MAHER, S. J. LILLY, V. MAINIERI, M. BRUSA, N. CAPPELLUCCI, G. HASINGER, G. ZAMORANI, M. SCODEGGIO, M. BOLZONELLA, T. CONTINI, C. M. CAROLLO, K. JAHNKE, J.-P. KNEIB, O. LE FEVRE, A. MERLONI, S. BARDELLI, A. BONGIORNO, H. BRUNNER, K. CAPUTI, F. CIVANO, A. COMASTRI, G. COPPA, O. CUCCIATI, S. DE LA TORRE, L. DE RAVEL, M. EIVIS, A. FINOGUENOV, F. FIORE, P. FRANZETTI, B. GARILLI, R. GILLI, A. IOVINO, P. KAMPCZYK, C. KNOBEL, K. KOVAČ, J.-F. LE BORGNE, V. LE BRUN, M. MIGNOLI, R. PELLO, Y. PENG, E. PÉREZ MONTERO, E. RICCIARDELLI, M. TANAKA, L. TASCA, L. TRESSE, D. VERGANI, C. VIGNALI, E. ZUCCA, D. BOTTINI, A. CAPPI, P. CASSATA, M. FEMANA, R. GRIFFITHS, J. KARTALTEPE, A. KOEKEMOER, C. MARINONI, H. J. MCCRACKEN, P. MEMEO, B. MENEUX, P. OESCH, C. PORCIANI, AND M. SALVATO. **Ongoing and Co-Evolving Star Formation in zCOSMOS Galaxies Hosting Active Galactic Nuclei.** *ApJ*, **696**:396–410, May 2009. 18
- [53] K. SCHAWINSKI, C. M. URRY, S. VIRANI, P. COPPI, S. P. BAMFORD, E. TREISTER, C. J. LINTOTT, M. SARZI, W. C. KEEL, S. KAVIRAJ, C. N. CARDAMONE, K. L. MASTERS, N. P. ROSS, D. ANDREESCU, P. MURRAY, R. C. NICHOI, M. J. RADDECK, A. SLOSAR, A. S. SZALAY, D. THOMAS, AND J. VANDENBERG. **Galaxy Zoo: The Fundamentally Different Co-Evolution of Supermassive Black Holes and Their Early- and Late-Type Host Galaxies.** *ApJ*, **711**:284–302, March 2010. 18
- [54] K. SCHAWINSKI. **The Role of AGN in the Migration of Early-Type Galaxies from the Blue Cloud to the Red Sequence.** In S. HEINZ AND E. WILCOTS, editors, *American Institute of Physics Conference Series*, pages 17–20, December 2009. 18, 19
- [55] P. J. MCCARTHY. **High redshift radio galaxies.** *ARA&A*, **31**:639–688, 1993. 21
- [56] E. L. ZIRBEL AND S. A. BAUM. **On the FR I/FR II Dichotomy in Powerful Radio Sources: Analysis of Their Emission-Line and Radio Luminosities.** *ApJ*, **448**:521, August 1995. 21, 66
- [57] G. KAUFFMANN, T. M. HECKMAN, AND P. N. BEST. **Radio jets in galaxies with actively accreting black holes: new insights from the SDSS.** *MNRAS*, **384**:953–971, March 2008. 21, 116
- [58] R. SAUNDERS, J. E. BALDWIN, S. RAWLINGS, P. J. WARNER, AND L. MILLER. **Spectrophotometry of FR II radio galaxies in an unbiased, low-redshift sample.** *MNRAS*, **238**:777–790, May 1989. 21
- [59] D. THOMAS, C. MARASTON, R. BENDER, AND C. MENDES DE OLIVEIRA. **The Epochs of Early-Type Galaxy Formation as a Function of Environment.** *ApJ*, **621**:673–694, March 2005. 21, 46, 55
- [60] A. CATTANEO, J. BLAZIOT, D. H. WEINBERG, D. KERÉŠ, S. COLOMBI, R. DAVÉ, J. DEVRIENDT, B. GUIDERDONI, AND N. KATZ. **Accretion, feedback and galaxy bimodality: a comparison of the GalICS semi-analytic model and cosmological SPH simulations.** *MNRAS*, **377**:63–76, May 2007. 22
- [61] C. TORTORA, V. ANTONUCCIO-DELOGO, S. KAVIRAJ, J. SILK, A. D. ROMEO, AND U. BECCIANI. **AGN jet-induced feedback in galaxies - II. Galaxy colours from a multicolour simulation.** *MNRAS*, **396**:61–77, June 2009. 22
- [62] M. VITALE, M. MIGNOLI, A. CIMATTI, S. J. LILLY, C. M. CAROLLO, T. CONTINI, J.-P. KNEIB, O. LE FEVRE, V. MAINIERI, A. RENZINI, M. SCODEGGIO, G. ZAMORANI, S. BARDELLI, L. BARNES, M. BOLZONELLA, A. BONGIORNO, R. BORDOLOTTI, T. J. BSCHORR, A. CAPPI, K. CAPUTI, G. COPPA, O. CUCCIATI, S. DE LA TORRE, L. DE RAVEL, P. FRANZETTI, B. GARILLI, A. IOVINO, P. KAMPCZYK, C. KNOBEL, A. M. KOEKEMOER, K. KOVAČ, F. LAMARELLE, J.-F. LE BORGNE, V. LE BRUN, C. LÓPEZ-SANJUAN, C. MAHER, H. J. MCCRACKEN, M. MORESCO, P. NAIR, P. A. OESCH, R. PELLO, Y. PENG, E. PÉREZ MONTERO, L. POZZETTI, V. PRESOTTO, J. SILVERMAN, M. TANAKA, L. TASCA, L. TRESSE, D. VERGANI, N. WELIKALA, AND E. ZUCCA. **Investigating the relationship between AGN activity and stellar mass in zCOSMOS galaxies at  $0 < z < 1$  using emission-line diagnostic diagrams.** *A&A*, **556**:A11, August 2013. 22, 24, 28, 51, 117, 119, 121, 150
- [63] T. M. HECKMAN, G. KAUFFMANN, J. BRINCHMANN, S. CHARLOT, C. TREMONTI, AND S. D. M. WHITE. **Present-Day Growth of Black Holes and Bulges: The Sloan Digital Sky Survey Perspective.** *ApJ*, **613**:109–118, September 2004. 23
- [64] N. I. SHAKURA AND R. A. SUNYAEV. **Black holes in binary systems. Observational appearance.** *A&A*, **24**:337–355, 1973. 23
- [65] H. N. NESVADBA, P. AND M. D. LEHNERT. **Outflows, Bubbles, and the Role of the Radio Jet: Direct Evidence for AGN Feedback at  $z$**  **2.** In C. CHARBONNEL, F. COMBES, AND R. SAMADI, editors, *SF2A-2008*, page 377, November 2008. 23
- [66] R. A. RIFFEL, T. STORCH-BERGMANN, AND C. WINGE. **Feeding versus feedback in AGNs from near-infrared IFU observations: the case of Mrk 79.** *MNRAS*, **430**:2249–2261, April 2013. 23
- [67] A. D. BOLATTO, S. R. WARREN, A. K. LEROY, F. WALTER, S. VEILLEUX, E. C. OSTRICKER, J. OTT, M. ZWAAN, D. B. FISHER, A. WEISS, E. ROSOLOWSKY, AND J. HODGE. **Suppression of star formation in the galaxy NGC 253 by a starburst-driven molecular wind.** *Nature*, **499**:450–453, July 2013. 23, 128

## REFERENCES

- [68] R. MORGANTI, J. FOGASY, Z. PARAGI, T. OOSTERLOO, AND M. ORIENTI. **Radio Jets Clearing the Way Through a Galaxy: Watching Feedback in Action.** *Science*, **341**:1082–1085, September 2013. 23
- [69] V. WILD, T. HECKMAN, AND S. CHARLOT. **Timing the starburst-AGN connection.** *MNRAS*, **405**:933–947, June 2010. 23
- [70] C. TADHUNTER, J. HOLT, R. GONZÁLEZ DELGADO, J. RODRÍGUEZ ZAURÍN, M. VILLAR-MARTÍN, R. MORGANTI, B. EMONTS, C. RAMOS ALMEIDA, AND K. INSKIP. **Starburst radio galaxies: general properties, evolutionary histories and triggering.** *MNRAS*, **412**:960–978, April 2011. 23
- [71] Ž. IVEZIĆ, K. MENOU, G. R. KNAPP, M. A. STRAUSS, R. H. LUPTON, D. E. VANDEN BERK, G. T. RICHARDS, C. TREMONTI, M. A. WEINSTEIN, S. ANDERSON, N. A. BAHCALL, R. H. BECKER, M. BERNARDI, M. BLANTON, D. EISENSTEIN, X. FAN, D. FINKHEIMER, K. FINLATOR, J. FREEMAN, J. E. GUNN, P. B. HALL, R. S. J. KIM, A. KINKHABWALA, V. K. NARAYANAN, C. M. ROCKOSI, D. SCHLEGEL, D. P. SCHNEIDER, I. STRATEVA, M. SUBBARAO, A. R. THAKAR, W. VOGES, R. L. WHITE, B. YANNY, J. BRINKMANN, M. DOI, M. FUKUGITA, G. S. HENNESSY, J. A. MUNN, R. C. NICHOLO, AND D. G. YORK. **Optical and Radio Properties of Extragalactic Sources Observed by the FIRST Survey and the Sloan Digital Sky Survey.** *AJ*, **124**:2364–2400, November 2002. 23, 34, 57, 60, 89
- [72] G. T. RICHARDS, X. FAN, H. J. NEWBERG, M. A. STRAUSS, D. E. VANDEN BERK, D. P. SCHNEIDER, B. YANNY, A. BOUCHER, S. BURLES, J. A. FREEMAN, J. E. GUNN, P. B. HALL, Ž. IVEZIĆ, S. KENT, J. LOVEDAY, R. H. LUPTON, C. M. ROCKOSI, D. J. SCHLEGEL, C. STOUTIGNON, M. SUBBARAO, AND D. G. YORK. **Spectroscopic Target Selection in the Sloan Digital Sky Survey: The Quasar Sample.** *AJ*, **123**:2945–2975, June 2002. 23
- [73] M. VITALE, J. ZUTHER, M. GARCÍA-MARÍN, A. ECKART, M. BREMER, M. VALENCIA-S, AND A. ZENSUS. **Classifying radio emitters from the Sloan Digital Sky Survey. Spectroscopy and diagnostics.** *A&A*, **546**:A17, October 2012. 24, 42, 49, 50, 51, 89, 116, 117, 118, 119, 150
- [74] M. VITALE, J. ZUTHER, M. GARCÍA-MARÍN, A. ECKART, M. BREMER, M. VALENCIA-S, AND A. ZENSUS. **A statistical study of SDSS radio-emitters.** *ArXiv e-prints*, March 2013. 24, 150
- [75] N. SCOVILLE, H. AUSSSEL, M. BRUSA, P. CAPAK, C. M. CAROLLO, M. ELVIS, M. GIALALISCO, L. GUZZO, G. HASINGER, C. IMPEY, J.-P. KNEIB, O. LEFÈVRE, S. J. LILLY, B. MOBASHER, A. RENZINI, R. M. RICH, D. B. SANDERS, E. SCHINNERER, D. SCHMINOVICH, P. SHOPPELL, Y. TANIGUCHI, AND N. D. TYSON. **The Cosmic Evolution Survey (COSMOS): Overview.** *ApJS*, **172**:1–8, September 2007. 27
- [76] G. HASINGER, N. CAPPELLUTI, H. BRUNNER, M. BRUSA, A. COMASTRI, M. ELVIS, A. FINOGUENOV, F. FIORE, A. FRANCESCINI, R. GILLI, R. E. GRIFITHS, I. LEHMANN, V. MAINIERI, G. MATT, I. MATUTE, T. MIYAJI, S. MOLENDI, S. PALTANI, D. B. SANDERS, N. SCOVILLE, L. TRESSE, C. M. URRY, P. VET-TOLANI, AND G. ZAMORANI. **The XMM-Newton Wide-Field Survey in the COSMOS Field. I. Survey Description.** *ApJS*, **172**:29–37, September 2007. 27
- [77] Y. TANIGUCHI, N. SCOVILLE, T. MURAYAMA, D. B. SANDERS, B. MOBASHER, H. AUSSSEL, P. CAPAK, M. AIKI, S. MIYAZAKI, Y. KOMIYAMA, Y. SHIOTA, T. NAGAO, S. S. SASAKI, J. KODA, C. CARILLI, M. GIALALISCO, L. GUZZO, G. HASINGER, C. IMPEY, O. LEFÈVRE, S. LILLY, A. RENZINI, M. RICH, E. SCHINNERER, P. SHOPPELL, N. KAUFÉ, H. KAROH, N. ARIMOTO, S. OKAMURA, AND K. OHTA. **The Cosmic Evolution Survey (COSMOS): Subaru Observations of the HST Cosmos Field.** *ApJS*, **172**:9–28, September 2007. 27
- [78] P. CAPAK, H. AUSSSEL, M. AIKI, H. J. MCCrackEN, B. MOBASHER, N. SCOVILLE, P. SHOPPELL, Y. TANIGUCHI, D. THOMPSON, S. TRIBIANO, S. SASAKI, A. W. BLAIN, M. BRUSA, C. CARILLI, A. COMASTRI, C. M. CAROLLO, P. CASATA, J. COLBERT, R. S. ELIS, M. ELVIS, M. GIALALISCO, W. GREEN, L. GUZZO, G. HASINGER, O. LIBERT, C. IMPEY, K. JAHNKE, J. KARTALTEPE, J.-P. KNEIB, J. KODA, A. KOEKMÖER, Y. KOMIYAMA, A. LEUTHAUD, O. LEFÈVRE, S. LILLY, C. LIU, R. MASSEY, S. MIYAZAKI, T. MURAYAMA, T. NAGAO, J. A. PEACOCK, A. PICKLES, C. PORCIANI, A. RENZINI, J. RHODES, M. RICH, M. SALVATO, D. B. SANDERS, C. SCARLATA, D. SCHMINOVICH, E. SCHINNERER, M. SCODEG-GIO, K. SHETH, Y. SHIOTA, L. A. M. TASCA, J. E. TAYLOR, L. YAN, AND G. ZAMORANI. **The First Release COSMOS Optical and Near-IR Data and Catalog.** *ApJS*, **172**:99–116, September 2007. 27
- [79] S. J. LILLY, O. LEFÈVRE, A. RENZINI, G. ZAMORANI, M. SCODEG-GIO, T. CONTINI, C. M. CAROLLO, G. HASINGER, J.-P. KNEIB, A. IOVINO, V. LE BRUN, C. MAER, V. MAINIERI, M. MIGNOLI, J. SHEYERMAN, L. A. M. TASCA, M. BOL-ZONELLA, A. BONGIORNO, D. BOTTINI, P. CAPAK, K. CAPU-PI, A. CMATTI, O. CUCCIATI, E. DADDI, R. FELDMANN, P. FRANZETTI, B. GARILLI, L. GUZZO, O. LIBERT, P. KAMP-CZYK, K. KOVAC, F. LAMARELLE, A. LEUTHAUD, J.-F. L. BORGNE, H. J. MCCrackEN, C. MARINONI, R. PELLO, E. RIC-CIARDELLI, C. SCARLATA, D. VERGANI, D. B. SANDERS, E. SCHINNERER, N. SCOVILLE, Y. TANIGUCHI, S. ARNOUTS, H. AUSSSEL, S. BARDELLI, M. BRUSA, A. CAPPI, P. CHIEGI, A. FINOGUENOV, S. FOUCAUD, R. FRANCESCINI, C. HAL-LIDAY, C. IMPEY, C. KNOBEL, A. KOEKMÖER, J. KUKK, D. MACCAGNI, S. MADDOX, B. MARANO, G. MARCONI, B. MENEUX, B. MOBASHER, C. MOREAU, J. A. PEACOCK, C. PORCIANI, L. POZZETTI, R. SCARAMELLA, D. SCHMINOVICH, P. SHOPPELL, I. SMAIL, D. THOMPSON, L. TRESSE, G. VET-TOLANI, A. ZANICHELLI, AND E. ZUCCA. **zCOSMOS: A Large VLT/VIMOS Redshift Survey Covering 0 <math>z < 3</math> in the COSMOS Field.** *ApJS*, **172**:70–85, September 2007. 27, 28, 42, 47
- [80] D. B. SANDERS, M. SALVATO, H. AUSSSEL, O. LIBERT, N. SCOVILLE, J. A. SURACE, D. T. PRAYER, K. SHETH, G. HELOU, T. BROOKE, B. BHATTACHARYA, L. YAN, J. S. KARTALTEPE, J. E. BARNES, A. W. BLAIN, D. CALZETTI, P. CAPAK, C. CARILLI, C. M. CAROLLO, A. COMASTRI, E. DADDI, R. S. ELIS, M. ELVIS, S. M. FALL, A. FRANCESCINI, M. GIALALISCO, G. HASINGER, C. IMPEY, A. KOEKMÖER, O. LEFÈVRE, S. LILLY, M. C. LIU, H. J. MCCrackEN, B. MOBASHER, A. RENZINI, M. RICH, E. SCHINNERER, P. L. SHOPPELL, Y. TANIGUCHI, D. J. THOMPSON, C. M. URRY, AND J. P. WILLIAMS. **S-COSMOS: The Spitzer Legacy Survey of the Hubble Space Telescope ACS 2 deg<sup>2</sup> COSMOS Field I: Survey Strategy and First Analysis.** *ApJS*, **172**:86–98, September 2007. 27
- [81] F. BERTOLDI, C. CARILLI, M. ARAVENA, E. SCHINNERER, H. VOSS, V. SMOLIC, K. JAHNKE, N. SCOVILLE, A. BLAIN, K. M. MENTEN, D. LUTZ, M. BRUSA, V. TANIGUCHI, P. CAPAK, B. MOBASHER, S. LILLY, D. THOMPSON, H. AUSSSEL, E. KREYSA,

- G. HASINGER, J. ACURRE, J. SCHLAERTH, AND A. KOEKEMOER. **COSBO: The MAMBO 1.2 Millimeter Imaging Survey of the COSMOS Field.** *ApJS*, **172**:132–149, September 2007. 27
- [82] E. SCHINNERER, V. SMOLČIĆ, C. L. GARILLI, M. BONDI, P. CILIEGI, K. JAINKE, N. Z. SCOVILLE, H. AUSSSEL, F. BERTOLDI, A. W. BLAIN, C. D. IMPY, A. M. KOEKEMOER, O. LE FÈVRE, AND C. M. URRY. **The VLA-COSMOS Survey. II. Source Catalog of the Large Project.** *ApJS*, **172**:46–69, September 2007. 27
- [83] A. M. KOEKEMOER, H. AUSSSEL, D. CALZETTI, P. CAPAK, M. GIAVALISIO, J.-P. KNEIB, A. LEAUTHAUD, O. LE FÈVRE, H. J. MCCRACKEN, R. MASSEY, B. MORASHER, J. RHODES, N. SCOVILLE, AND P. L. SHOPPELL. **The COSMOS Survey: Hubble Space Telescope Advanced Camera for Surveys Observations and Data Processing.** *ApJS*, **172**:196–202, September 2007. 27
- [84] H. J. MCCRACKEN, P. CAPAK, M. SALVATO, H. AUSSSEL, D. THOMPSON, E. DADDI, D. B. SANDERS, J.-P. KNEIB, C. J. WILLOTT, C. MANCINI, A. RENZINI, R. COOK, O. LE FÈVRE, O. LIBERT, J. KARTALTEPE, A. M. KOEKEMOER, Y. MELLIER, T. MURAYAMA, N. Z. SCOVILLE, Y. SHIOYA, AND Y. TANAGUCHI. **The COSMOS-WIRCam Near-Infrared Imaging Survey. I. zK-Selected Passive and Star-Forming Galaxy Candidates at  $z_{\text{gsm}} 1.4$ .** *ApJ*, **708**:202–217, January 2010. 27
- [85] S. J. LILLY, V. LE BRUN, C. MAIER, V. MAINIERI, M. MIGNOLI, M. SCODEGGIO, G. ZAMORANI, M. CAROLLO, T. CONTINI, J.-P. KNEIB, O. LE FÈVRE, A. RENZINI, S. BARDELLI, M. BOLZONELLA, A. BONGIORNO, K. CAPUTI, G. COPPA, O. CUCCIATI, S. DE LA TORRE, L. DE RAVEL, P. FRANZETTI, B. GARILLI, A. IOVINO, P. KAMP CZYK, K. KOVAC, C. KNOBEL, F. LAMARELLE, J.-F. LE BORGNE, R. PELLÓ, Y. PENG, E. PÉREZ-MONTERO, E. RICCIARDELLI, J. D. SILVERMAN, M. TANAKA, L. TASCIA, L. TRESSE, D. VERGANI, E. ZUCCA, O. LIBERT, M. SALVATO, P. OESCH, U. ABBAS, D. BOTTINI, P. CAPAK, A. CAPPI, P. CASSATA, A. CIMATTI, M. ELVIS, M. FUMANA, L. GUZZO, G. HASINGER, A. KOEKEMOER, A. LEAUTHAUD, D. MACCAGNI, C. MARINONI, H. MCCRACKEN, P. MEMEO, B. MENEUX, C. PORCIANI, L. POZZETTI, D. SANDERS, R. SCARAMELLA, C. SCARLATA, N. SCOVILLE, P. SHOPPELL, AND Y. TANIGUCHI. **The zCOSMOS 10k-Bright Spectroscopic Sample.** *ApJS*, **184**:218–229, October 2009. 28
- [86] O. LIBERT, P. CAPAK, M. SALVATO, H. AUSSSEL, H. J. MCCRACKEN, D. B. SANDERS, N. SCOVILLE, J. KARTALTEPE, S. ARNOUTS, E. LE FLOC'H, B. MORASHER, Y. TANIGUCHI, F. LAMARELLE, A. LEAUTHAUD, S. SASAKI, D. THOMPSON, M. ZAMOJSKI, G. ZAMORANI, S. BARDELLI, M. BOLZONELLA, A. BONGIORNO, M. BRISA, K. I. CAPUTI, C. M. CAROLLO, T. CONTINI, R. COOK, G. COPPA, O. CUCCIATI, S. DE LA TORRE, L. DE RAVEL, P. FRANZETTI, B. GARILLI, G. HASINGER, A. IOVINO, P. KAMP CZYK, J.-P. KNEIB, C. KNOBEL, K. KOVAC, J. F. LE BORGNE, V. LE BRUN, O. LE FÈVRE, S. LILLY, D. LOOPER, C. MAIER, V. MAINIERI, Y. MELLIER, M. MIGNOLI, T. MURAYAMA, R. PELLÓ, Y. PENG, E. PÉREZ-MONTERO, A. RENZINI, E. RICCIARDELLI, D. SCHMINOVICH, M. SCODEGGIO, Y. SHIOYA, J. SILVERMAN, J. SURACE, M. TANAKA, L. TASCIA, L. TRESSE, D. VERGANI, AND E. ZUCCA. **Cosmos Photometric Redshifts with 30-Bands for 2-deg<sup>2</sup>.** *ApJ*, **690**:1236–1249, January 2009. 28
- [87] L. POZZETTI, M. BOLZONELLA, E. ZUCCA, G. ZAMORANI, S. LILLY, A. RENZINI, M. MORESCO, M. MIGNOLI, P. CASATA, L. TASCIA, F. LAMARELLE, C. MAIER, B. MENEUX, C. HALLIDAY, P. OESCH, D. VERGANI, K. CAPUTI, K. KOVAC, A. CIMATTI, O. CUCCIATI, A. IOVINO, Y. PENG, M. CAROLLO, T. CONTINI, J.-P. KNEIB, O. LE FÈVRE, V. MAINIERI, M. SCODEGGIO, S. BARDELLI, A. BONGIORNO, G. COPPA, S. DE LA TORRE, L. DE RAVEL, P. FRANZETTI, B. GARILLI, P. KAMP CZYK, C. KNOBEL, J.-F. LE BORGNE, V. LE BRUN, R. PELLÓ, E. PÉREZ-MONTERO, E. RICCIARDELLI, J. D. SILVERMAN, M. TANAKA, L. TRESSE, U. ABBAS, D. BOTTINI, A. CAPPI, L. GUZZO, A. M. KOEKEMOER, A. LEAUTHAUD, D. MACCAGNI, C. MARINONI, H. J. MCCRACKEN, P. MEMEO, C. PORCIANI, R. SCARAMELLA, C. SCARLATA, AND N. SCOVILLE. **zCOSMOS – 10k-bright spectroscopic sample. The bimodality in the galaxy stellar mass function: exploring its evolution with redshift.** *A&A*, **523**:A13, November 2010. 28, 30
- [88] M. BOLZONELLA, K. KOVAC, L. POZZETTI, E. ZUCCA, O. CUCCIATI, S. J. LILLY, Y. PENG, A. IOVINO, G. ZAMORANI, D. VERGANI, L. A. M. TASCIA, F. LAMARELLE, P. OESCH, K. CAPUTI, P. KAMP CZYK, S. BARDELLI, C. MAIER, U. ABBAS, C. KNOBEL, M. SCODEGGIO, C. M. CAROLLO, T. CONTINI, J.-P. KNEIB, O. LE FÈVRE, V. MAINIERI, A. RENZINI, A. BONGIORNO, G. COPPA, S. DE LA TORRE, L. DE RAVEL, P. FRANZETTI, B. GARILLI, J.-F. LE BORGNE, V. LE BRUN, M. MIGNOLI, R. PELLÓ, E. PÉREZ-MONTERO, E. RICCIARDELLI, J. D. SILVERMAN, M. TANAKA, L. TRESSE, D. BOTTINI, A. CAPPI, P. CASSATA, A. CIMATTI, L. GUZZO, A. M. KOEKEMOER, A. LEAUTHAUD, D. MACCAGNI, C. MARINONI, H. J. MCCRACKEN, P. MEMEO, B. MENEUX, C. PORCIANI, R. SCARAMELLA, H. AUSSSEL, P. CAPAK, C. HALLIDAY, O. LIBERT, J. KARTALTEPE, M. SALVATO, D. SANDERS, C. SCARLATA, N. SCOVILLE, Y. TANIGUCHI, AND D. THOMPSON. **Tracking the impact of environment on the galaxy stellar mass function up to  $z \sim 1$  in the 10 k zCOSMOS sample.** *A&A*, **524**:A76, December 2010. 28
- [89] G. CHABRIER. **The Galactic Disk Mass Function: Reconciliation of the Hubble Space Telescope and Nearby Determinations.** *ApJ*, **586**:L133–L136, April 2003. 28
- [90] P. PADOVANI AND C. M. URRY. **Luminosity functions, relativistic beaming, and unified theories of high-luminosity radio sources.** *ApJ*, **387**:449–457, March 1992. 29
- [91] G. BRUZUAL AND S. CHARLOT. **Stellar population synthesis at the resolution of 2003.** *MNRAS*, **344**:1000–1028, October 2003. 32, 33
- [92] D. G. YORK, J. ADelman, J. E. ANDERSON, JR., S. F. ANDERSON, J. ANIS, N. A. BAHCALL, J. A. BAKKEN, R. BARKHOUSER, S. BASTIAN, E. BERMAN, W. N. BOROSHI, S. BRACKER, C. BRIEGEL, J. W. BRIGGS, J. BRINKMANN, R. BRUNNER, S. BURLIS, L. CAREY, M. A. CARR, F. J. CASTANDER, B. CHEN, P. L. COLESTOCK, A. J. CONNOLLY, J. H. CROCKER, I. CSABAI, P. C. CZARAPATA, J. E. DAVIS, M. DOI, T. DOMEBECK, D. EISENSTEIN, N. ELLMAN, B. R. ELMS, M. L. EVANS, X. FAN, G. R. FEDERWITZ, L. FISCELLI, S. FRIEDMAN, J. A. FRIEDMAN, M. FUKUGITA, B. GILLESPIE, J. E. GUIN, V. K. GURBANI, E. DE HAAS, M. HALDEMAN, F. H. HARRIS, J. HAYES, T. M. HECKMAN, G. S. HENNESSY, R. B. HINDSLEY, S. HOLM, E. KINNEY, M. KLAENE, A. N. KLEINMAN, S. KLEINMAN, G. R. KNAPP, J. KOHENEK, R. G. KRON, P. Z. KUNSZT, D. Q. LAMB, B. LEE, R. F. LEGER, S. LIMMONGKOL, C. LINDENMEYER, D. C. LONG, C. LOMIS, J. LOVEDAY, R. LUCIGNO, R. H. LUPTON, B. MACKINNON, E. J. MANNERY, P. M. MANTSCH, B. MARGON, P. MCGEEHEE, T. A. MCKAY, A. MEIKSIN, A. MERELLI,

## REFERENCES

- D. G. MONET, J. A. MUNN, V. K. NARAYANAN, T. NASHI, E. NEILSEN, R. NEWBOLD, H. J. NEWBERG, R. C. NICHOI, T. NICINSKI, M. NONINO, N. OKADA, S. OKAMURA, J. P. OSTRIKER, R. OWEN, A. G. PAULS, J. PEOPLES, R. L. PETERSON, D. PETRAVICK, J. R. PIER, A. POPE, R. PORDES, A. PROSAPIO, R. RECHENMACHER, T. R. QUINN, G. T. RICHARDS, M. W. RICHMOND, C. H. RIVETTA, C. M. ROCKOSI, K. RUTHMANSDORFER, D. SANDFORD, D. J. SCHLEGEL, D. P. SCHNEIDER, M. SEKIGUCHI, G. SERGEY, K. SHIMASAKU, W. A. SIDEMUND, S. SMEE, J. A. SMITH, S. SNEDDEN, R. STONE, C. STOUGHTON, M. A. STRAUSS, C. STUBBS, M. SUBBARAO, A. S. SZALAY, I. SZAPUDI, G. P. SZKODY, A. R. THAKAR, C. TREMONTI, D. L. TUCKER, A. UOMOTO, D. VANDEN BERK, M. S. VOGELY, P. WADDELL, S.-I. WANG, M. WATANABE, D. H. WEINBERG, B. YANNU, N. YASUDA, AND SDSS COLLABORATION. **The Sloan Digital Sky Survey: Technical Summary.** *AJ*, **120**:1579–1587, September 2000. 32
- [93] C. STOUGHTON, R. H. LUPTON, M. BERNARDI, M. R. BLANTON, S. BURLIS, F. J. CASTANDER, A. J. CONNOLLY, D. J. EBENSTEN, J. A. FRIEMAN, G. S. HENNESSY, R. B. HINDSLEY, Z. IVEZIĆ, S. KENT, P. Z. KUNNETT, B. C. LEE, A. MEIKSIN, J. A. MUNN, H. J. NEWBERG, R. C. NICHOI, T. NICINSKI, J. R. PIER, G. T. RICHARDS, M. W. RICHMOND, D. J. SCHLEGEL, J. A. SMITH, M. A. STRAUSS, M. SUBBARAO, A. S. SZALAY, A. R. THAKAR, D. L. TUCKER, D. E. VANDEN BERK, B. YANNU, J. K. ADELMAN, J. E. ANDERSON, JR., S. F. ANDERSON, J. ANNIS, N. A. BAICCALL, J. A. BAKKEN, M. BARTELMANN, S. BASTIAN, A. BAUER, E. BERMAN, H. BÖHRINGER, W. N. BOROSKI, S. BRACKER, C. BRUEGEL, J. W. BRIGGS, J. BRINKMANN, R. BRUNNER, L. CAREY, M. A. CARR, B. CHEN, D. CHRISTIAN, P. L. COLESTOCK, J. H. CROCKER, I. CSABAI, P. C. CZARAPATA, J. DALCANTO, A. F. DAVIDSEN, J. E. DAVIS, W. DEHNEN, S. DODDELSON, M. DOI, T. DOMBECK, M. DONAHUE, N. ELLMAN, B. R. ELMS, M. L. EVANS, L. EYER, X. FAN, G. R. FEDERWITZ, S. FRIEDMAN, M. FUKUGITA, R. GAL, B. GILLESPIE, K. GLAZEBROOK, J. GRAY, E. K. GREEB, B. GREENAWALT, G. GREENE, J. E. GUNN, E. DE HAAS, Z. HADMAN, M. HALDEMAN, P. B. HALL, M. HAMABE, B. HANSEN, F. H. HARRIS, H. HARRIS, M. HARVANEK, S. L. HAWLEY, J. J. E. HAYES, T. M. HECKMAN, A. HELMI, A. HENDEN, C. J. HOGAN, D. W. HOOG, D. J. HOLMGREN, J. HOLTZMAN, C.-H. HUANG, C. HULL, S.-I. ICHIKAWA, T. ICHIKAWA, D. E. JOHNSTON, G. KAUFFMANN, R. S. J. KIM, T. KIMBALL, E. KINNEY, M. KLAESNE, S. J. KLEINMAN, A. KLYPIN, G. R. KNAPP, J. KORHENEK, J. KRÖLIK, R. G. KRON, J. KRZYSIŃSKI, D. Q. LAMB, R. F. LEGER, S. LIMMONGKOL, C. LINDENMEYER, D. C. LONG, C. LOOMIS, J. LOVEDAY, B. MACKINNON, E. J. MANNERY, P. M. MANTSCH, B. MARGON, P. MCGEEHEE, T. A. MCKAY, B. MCLEAN, K. MENOU, A. MERELLI, H. J. MO, D. G. MONET, O. NAKAMURA, V. K. NARAYANAN, T. NASHI, E. H. NEILSEN, JR., P. R. NEWMAN, A. NITTA, M. ODENKIRCHEN, N. OKADA, S. OKAMURA, J. P. OSTRIKER, R. OWEN, A. G. PAULS, J. PEOPLES, R. S. PETERSON, D. PETRAVICK, A. POPE, R. PORDES, M. POSTMAN, A. PROSAPIO, T. R. QUINN, R. RECHENMACHER, C. H. RIVETTA, H.-W. RIX, C. M. ROCKOSI, R. ROSNER, K. RUTHMANSDORFER, D. SANDFORD, D. P. SCHNEIDER, R. SCANTON, M. SEKIGUCHI, G. SERGEY, R. SHETHI, K. SHIMASAKU, S. SMEE, S. A. SNEDDEN, A. STEBBINS, C. STUBBS, I. SZAPUDI, P. SZKODY, G. P. SZKODY, S. TABACHNIK, Z. TSVETANOV, A. UOMOTO, M. S. VOGELY, W. VOGES, P. WADDELL, R. WALTERBOS, S.-I. WANG, M. WATANABE, D. H. WEINBERG, R. L. WHITE, S. D. M. WHITE, B. WILHITE, D. WOLFE, N. YASUDA, D. G. YORK, I. ZEHAVI, AND W. ZHENG. **Sloan Digital Sky Survey: Early Data Release.** *AJ*, **123**:485–548, January 2002. 32
- [94] L. J. KEWLEY, M. J. GELLER, AND R. A. JANSEN. **[OII] as a SFR indicator and the Cosmic Star Formation History.** In *American Astronomical Society Meeting Abstracts*, **35** of *Bulletin of the American Astronomical Society*, page 119.01, December 2003. 33, 35, 39, 45, 59, 92
- [95] K. N. ABAZAJAN, J. K. ADELMAN-MCCARTHY, M. A. AGÜEROS, S. S. ALLAM, C. ALLENDE PRIETO, D. AN, K. S. J. ANDERSON, S. F. ANDERSON, J. ANNIS, N. A. BAICCALL, AND ET AL. **The Seventh Data Release of the Sloan Digital Sky Survey.** *ApJS*, **182**:543–558, June 2009. 33
- [96] K. OH, M. SARZI, K. SCHAWINSKI, AND S. K. YI. **Improved and Quality-assessed Emission and Absorption Line Measurements in Sloan Digital Sky Survey Galaxies.** *ApJS*, **195**:13, August 2011. 34
- [97] R. H. BECKER, R. L. WHITE, AND D. J. HELFAND. **The FIRST Survey: Faint Images of the Radio Sky at Twenty Centimeters.** *ApJ*, **450**:559, September 1995. 34, 60
- [98] J. J. CONDON, W. D. COTTON, E. W. GREISEN, Q. F. YIN, R. A. PERLEY, G. B. TAYLOR, AND J. J. BRODERICK. **The NRAO VLA Sky Survey.** *AJ*, **115**:1693–1716, May 1998. 34
- [99] G. STASIŃSKA, N. VALE ASARI, R. CID FERNANDES, J. M. GOMES, M. SCHLICKMANN, A. MATEUS, W. SCHOENELL, L. SODRÉ, JR., AND SEAGAL COLLABORATION. **Can retired galaxies mimic active galaxies? Clues from the Sloan Digital Sky Survey.** *MNRAS*, **391**:L29–L33, November 2008. 35, 70, 83, 119
- [100] R. CID FERNANDES, G. STASIŃSKA, M. S. SCHLICKMANN, A. MATEUS, N. VALE ASARI, W. SCHOENELL, AND L. SODRÉ, JR. **Alternative diagnostic diagrams and the ‘forgotten’ population of weak line galaxies in the SDSS.** *MNRAS*, **403**:1036–1053, April 2010. 35, 70
- [101] R. CID FERNANDES, G. STASIŃSKA, A. MATEUS, AND N. VALE ASARI. **A comprehensive classification of galaxies in the Sloan Digital Sky Survey: how to tell true from fake AGN?** *MNRAS*, **413**:1687–1699, May 2011. 35, 73
- [102] V. SMOLČIĆ. **The Radio AGN Population Dichotomy: Green Valley Seyferts Versus Red Sequence Low-Excitation Active Galactic Nuclei.** *ApJ*, **699**:L43–L47, July 2009. 35, 90, 121
- [103] G. STASIŃSKA, R. CID FERNANDES, A. MATEUS, L. SODRÉ, AND N. V. ASARI. **Semi-empirical analysis of Sloan Digital Sky Survey galaxies - III. How to distinguish AGN hosts.** *MNRAS*, **371**:972–982, September 2006. 36, 48, 52, 70, 77, 83, 92, 117
- [104] L. TRESSE, C. ROLA, F. HAMMER, G. STASIŃSKA, O. LE FEVRE, S. J. LILLY, AND D. CRAMPTON. **The Canada-France Redshift Survey - XII. Nature of emission-line field galaxy population up to  $z=0.3$ .** *MNRAS*, **281**:847–870, August 1996. 37, 48
- [105] C. S. ROLA, E. TERLEVICHI, AND R. J. TERLEVICHI. **New diagnostic methods for emission-line galaxies in deep surveys.** *MNRAS*, **289**:419–427, August 1997. 37, 46, 48

- [106] F. LAMARELLE, M. MOUCHINE, T. CONTINI, I. LEWIS, AND S. MADDOK. **The luminosity-metallicity relation in the local Universe from the 2dF Galaxy Redshift Survey.** *MNRAS*, **350**:396–406, May 2004. 37, 45, 46, 48, 50, 59, 92
- [107] F. LAMARELLE. **Spectral classification of emission-line galaxies from the Sloan Digital Sky Survey. I. An improved classification for high-redshift galaxies.** *A&A*, **509**:A53, January 2010. 37, 45, 48, 50, 51, 58, 92
- [108] W. OMULLANE, N. LI, M. NIETO-SANTISTEBAN, A. SZALAY, A. THAKAR, AND J. GRAY. **Batch is back: CasJobs, serving multi-TB data on the Web.** *eprint arXiv:cs/0502072*, February 2005. 37
- [109] P. N. BEST, G. KAUFFMANN, T. M. HECKMAN, AND Ž. IVEZIĆ. **A sample of radio-loud active galactic nuclei in the Sloan Digital Sky Survey.** *MNRAS*, **362**:9–24, September 2005. 38, 60, 89
- [110] M. R. BLANTON, H. LIN, R. H. LUPTON, F. M. MALEY, N. YOUNG, I. ZEHAVI, AND J. LOVEDAY. **An Efficient Targeting Strategy for Multiobject Spectrograph Surveys: the Sloan Digital Sky Survey “Tiling” Algorithm.** *AJ*, **125**:2276–2286, April 2003. 38
- [111] M. R. BLANTON. **Galaxies in SDSS and DEEP2: A Quiet Life on the Blue Sequence?** *ApJ*, **648**:268–280, September 2006. 38
- [112] R. L. WHITE, R. H. BECKER, D. J. HELFAND, AND M. D. GREGG. **A Catalog of 1.4 GHz Radio Sources from the FIRST Survey.** *ApJ*, **475**:479, February 1997. 38
- [113] F. M. MONTENEGRO-MONTES, K.-H. MACK, M. VIGOTTI, C. R. BENN, R. CARBALLO, J. I. GONZÁLEZ-SERRANO, J. HOLT, AND F. JIMÉNEZ-LUJÁN. **Radio spectra and polarization properties of radio-loud broad absorption-line quasars.** *MNRAS*, **388**:1853–1868, August 2008. 41
- [114] J. W. M. BAARS, R. GENZEL, I. I. K. PAULINY-TOTH, AND A. WITZEL. **The absolute spectrum of CAS A - an accurate flux density scale and a set of secondary calibrators.** *A&A*, **61**:99–106, October 1977. 41
- [115] R. ANTONUCCI. **A panchromatic review of thermal and nonthermal active galactic nuclei.** *Astronomical and Astrophysical Transactions*, **27**:557–602, 2012. 42, 88
- [116] J. C. SHIELDS, H.-W. RIX, M. SARZI, A. J. BARTH, A. V. FILIPPENKO, L. C. HO, D. H. MCINTOSH, G. RUDNICK, AND W. L. W. SARGENT. **The Survey of Nearby Nuclei with the Space Telescope Imaging Spectrograph: Emission-Line Nuclei at Hubble Space Telescope Resolution.** *ApJ*, **654**:125–137, January 2007. 43
- [117] L. C. HO, A. V. FILIPPENKO, AND W. L. W. SARGENT. **A Search for “Dwarf” Seyfert Nuclei. V. Demographics of Nuclear Activity in Nearby Galaxies.** *ApJ*, **487**:568, October 1997. 43, 48, 59
- [118] M. SARZI, H.-W. RIX, J. C. SHIELDS, L. C. HO, A. J. BARTH, G. RUDNICK, A. V. FILIPPENKO, AND W. L. W. SARGENT. **The Stellar Populations in the Central Parsecs of Galactic Bulges.** *ApJ*, **628**:169–186, July 2005. 45, 56
- [119] L. C. HO. **[O II] Emission in Quasar Host Galaxies: Evidence for a Suppressed Star Formation Efficiency.** *ApJ*, **629**:680–685, August 2005. 45, 57
- [120] E. PÉREZ-MONTERO, G. F. HÁGELE, T. CONTINI, AND Á. I. DÍAZ. **Neon and argon optical emission lines in ionized gaseous nebulae: implications and applications.** *MNRAS*, **381**:125–135, October 2007. 46
- [121] L. L. COWIE, A. SONGAILA, E. M. HU, AND J. G. COHEN. **New Insight on Galaxy Formation and Evolution From Keck Spectroscopy of the Hawaii Deep Fields.** *AJ*, **112**:839, September 1996. 46, 55
- [122] T. KODAMA, T. YAMADA, M. AKIYAMA, K. AOKI, M. DOI, H. FURUSAWA, T. FUSE, M. IMANISHI, C. ISHIDA, M. IYE, M. KAJISAWA, H. KAROJI, N. KOBAYASHI, Y. KOMIYAMA, G. KOSUGI, Y. MAEDA, S. MIYAZAKI, Y. MIZUMOTO, T. MOROKUMA, F. NAKATA, J. NOUMARU, R. OGASAWARA, M. OUCHI, T. SASAKI, K. SEKIGUCHI, K. SHIMASAKU, C. SIMPSON, T. TAKATA, I. TANAKA, Y. UEDA, N. YASUDA, AND M. YOSHIDA. **Down-sizing in galaxy formation at  $z \sim 1$  in the Subaru/XMM-Newton Deep Survey (SXDS).** *MNRAS*, **350**:1005–1014, May 2004. 46, 55
- [123] M. TANAKA, T. KODAMA, N. ARIMOTO, S. OKAMURA, K. UMETSU, K. SHIMASAKU, I. TANAKA, AND T. YAMADA. **The build-up of the colour-magnitude relation as a function of environment.** *MNRAS*, **362**:268–288, September 2005. 46, 55
- [124] S. JUNEAU, K. GLAZEBROOK, D. CRAMPTON, P. J. MCCARTHY, S. SAVAGLIO, R. ABRAHAM, R. G. CARLBERG, H.-W. CHEN, D. LE BORGNE, R. O. MARKEE, K. ROTH, I. JORGENSEN, I. HOOK, AND R. MURDWINSKI. **Cosmic Star Formation History and Its Dependence on Galaxy Stellar Mass.** *ApJ*, **619**:L135–L138, February 2005. 46, 54, 55
- [125] K. BUNDY, R. S. ELLIS, C. J. CONSELICE, J. E. TAYLOR, M. C. COOPER, C. N. A. WILLMER, B. J. WEINER, A. L. COIL, K. G. NOESKE, AND P. R. M. EISENHARDT. **The Mass Assembly History of Field Galaxies: Detection of an Evolving Mass Limit for Star-Forming Galaxies.** *ApJ*, **651**:120–141, November 2006. 46, 55
- [126] A. HEAVENS, B. PANTER, R. JIMENEZ, AND J. DUNLOP. **The star-formation history of the Universe from the stellar populations of nearby galaxies.** *Nature*, **428**:625–627, April 2004. 46
- [127] T. TREU, R. S. ELLIS, T. X. LIAO, AND P. G. VAN DOKKUM. **Keck Spectroscopy of Distant GOODS Spheroidal Galaxies: Downsizing in a Hierarchical Universe.** *ApJ*, **622**:L5–L8, March 2005. 46
- [128] A. VAN DER WEL, M. FRANK, P. G. VAN DOKKUM, H.-W. RIX, G. D. ILLINGWORTH, AND P. ROSATI. **Mass-to-Light Ratios of Field Early-Type Galaxies at  $z \sim 1$  from Ultra-deep Spectroscopy: Evidence for Mass-dependent Evolution.** *ApJ*, **631**:145–162, September 2005. 46
- [129] R. JIMENEZ, B. PANTER, A. F. HEAVENS, AND L. VERDE. **Baryonic conversion trees: the global assembly of stars and dark matter in galaxies from the Sloan Digital Sky Survey.** *MNRAS*, **356**:495–501, January 2005. 46
- [130] K. BUNDY, M. FUKUGITA, R. S. ELLIS, T. KODAMA, AND C. J. CONSELICE. **A Slow Merger History of Field Galaxies since  $z \sim 1$ .** *ApJ*, **601**:L123–L126, February 2004. 46

## REFERENCES

- [131] J. AIRD, A. L. COIL, J. MOUSTAKAS, M. R. BLANTON, S. M. BURLIS, R. J. COOL, D. J. EISENSTEIN, M. S. M. SMITH, K. C. WONG, AND G. ZHU. **PRIMUS: The Dependence of AGN Accretion on Host Stellar Mass and Color.** *ApJ*, **746**:90, February 2012. 47, 117
- [132] S. JUNEAU, M. DICKINSON, D. M. ALEXANDER, AND S. SALIM. **A New Diagnostic of Active Galactic Nuclei: Revealing Highly Absorbed Systems at Redshift 0.3.** *ApJ*, **736**:104, August 2011. 48, 50, 52, 53
- [133] G. DENICOLÒ, R. TERLEVICH, AND E. TERLEVICH. **New light on the search for low-metallicity galaxies - I. The N2 calibrator.** *MNRAS*, **330**:69–74, February 2002. 48
- [134] L. J. KEWLEY AND M. A. DOPTA. **Using Strong Lines to Estimate Abundances in Extragalactic H II Regions and Starburst Galaxies.** *ApJS*, **142**:35–52, September 2002. 48, 92
- [135] M. PETTINI AND B. E. J. PAGEL. **[OIII]/[NII] as an abundance indicator at high redshift.** *MNRAS*, **348**:L59–L63, March 2004. 48, 70, 92
- [136] M. A. DOPTA, L. J. KEWLEY, AND R. S. SUTHERLAND. **Photoionization, Shocks or Starbursts?** In W. J. HENNEY, J. FRANCO, AND M. MARTOS, editors, *Revista Mexicana de Astronomía y Astrofísica Conference Series*, **12** of *Revista Mexicana de Astronomía y Astrofísica*, vol. 27, pages 225–229, February 2002. 49, 59, 92, 93
- [137] A. BONGIORNO, M. MIGNOLI, G. ZAMORANI, F. LAMARELLE, G. LANZUZI, T. MIYAI, M. BOLZONELLA, C. M. CAROLLO, T. CONTINI, J. P. KNEIB, O. LE FÈVRE, S. J. LILLY, V. MAINIERI, A. RENZINI, M. SCODEGGIO, S. BARDELLI, M. BRUSA, K. CAPUTI, F. CIVANO, G. COPPA, O. CUCCIATI, S. DE LA TORRE, L. DE RAVEL, P. FRANZETTI, B. GARILLI, C. HALLIDAY, G. HASINGER, A. M. KOEKEMOER, A. IOVINO, P. KAMPczyk, C. KNOBEL, K. KOVÁČ, J.-F. LE BORGNE, V. LE BRUN, C. MAIER, A. MERLONI, P. NAIR, R. PELLO, Y. PENG, E. PÉREZ MONTERO, E. RICCIARDELLI, M. SALVATO, J. SILVERMAN, M. TANAKA, L. TASCIA, L. TRESSE, D. VERGANI, E. ZUCCA, U. ABBAS, D. BOTTINI, A. CAPPI, P. CASATA, A. CIMATTI, L. GUZZO, A. LEAUFHAUD, D. MACCAGNI, C. MARINONI, H. J. MCCrackEN, P. MEMEO, B. MENEUX, P. OESCH, C. PORCIANI, L. POZZETTI, AND R. SCARAMELLA. **The [O iii] emission line luminosity function of optically selected type-2 AGN from zCOSMOS.** *A&A*, **510**:A56, February 2010. 50
- [138] K. I. CAPUTI, S. J. LILLY, H. AUSSSEL, D. SANDERS, D. FRAYER, O. LE FÈVRE, A. RENZINI, G. ZAMORANI, M. SCODEGGIO, T. CONTINI, N. SCOVILLE, C. M. CAROLLO, G. HASINGER, A. IOVINO, V. LE BRUN, E. LE FLOCH, C. MAIER, V. MAINIERI, M. MIGNOLI, M. SALVATO, D. SCHIMMOWICH, J. SILVERMAN, J. SURACE, L. TASCIA, U. ABBAS, S. BARDELLI, M. BOLZONELLA, A. BONGIORNO, D. BOTTINI, P. CAPPAC, A. CAPPI, P. CASATA, A. CIMATTI, O. CUCCIATI, S. DE LA TORRE, L. DE RAVEL, P. FRANZETTI, M. FUMANA, B. GARILLI, C. HALLIDAY, O. ILBERT, P. KAMPczyk, J. KARTALTEPE, J.-P. KNEIB, C. KNOBEL, K. KOVÁČ, F. LAMARELLE, A. LEAUFHAUD, J. F. LE BORGNE, D. MACCAGNI, C. MARINONI, H. MCCrackEN, B. MENEUX, P. OESCH, R. PELLÒ, E. PÉREZ-MONTERO, C. PORCIANI, E. RICCIARDELLI, R. SCARAMELLA, C. SCARLATA, L. TRESSE, D. VERGANI, J. WALCHER, M. ZAMOJSKI, AND E. ZUCCA. **The Optical Spectra of 24  $\mu$ m Galaxies in the COSMOS Field. I. Spitzer MIPS Bright Sources in the zCOSMOS-Bright 10k Catalog.** *ApJ*, **680**:939–961, June 2008. 51
- [139] K. I. CAPUTI, S. J. LILLY, H. AUSSSEL, E. LE FLOCH, D. SANDERS, C. MAIER, D. FRAYER, C. M. CAROLLO, T. CONTINI, J.-P. KNEIB, O. LE FÈVRE, V. MAINIERI, A. RENZINI, M. SCODEGGIO, N. SCOVILLE, G. ZAMORANI, S. BARDELLI, M. BOLZONELLA, A. BONGIORNO, G. COPPA, O. CUCCIATI, S. DE LA TORRE, L. DE RAVEL, P. FRANZETTI, B. GARILLI, O. ILBERT, A. IOVINO, P. KAMPczyk, J. KARTALTEPE, C. KNOBEL, K. KOVÁČ, F. LAMARELLE, J.-F. LE BORGNE, V. LE BRUN, M. MIGNOLI, Y. PENG, E. PÉREZ-MONTERO, E. RICCIARDELLI, M. SALVATO, J. SILVERMAN, J. SURACE, M. TANAKA, L. TASCIA, L. TRESSE, D. VERGANI, E. ZUCCA, U. ABBAS, D. BOTTINI, P. CAPPAC, A. CAPPI, P. CASATA, A. CIMATTI, M. ELVIS, G. HASINGER, A. M. KOEKEMOER, A. LEAUFHAUD, D. MACCAGNI, C. MARINONI, H. MCCrackEN, P. MEMEO, B. MENEUX, P. OESCH, R. PELLÒ, C. PORCIANI, L. POZZETTI, R. SCARAMELLA, C. SCARLATA, D. SCHIMMOWICH, Y. TANIGUCHI, AND M. ZAMOJSKI. **The Optical Spectra of Spitzer 24  $\mu$ m Galaxies in the Cosmic Evolution Survey Field. II. Infrared Sources in the zCOSMOS-Bright 10k Catalog.** *ApJ*, **707**:1387–1403, December 2009. 51
- [140] C. A. TREMONTI, T. M. HECKMAN, G. KAUFFMANN, J. BRUNCHMANN, S. CHARLOT, S. D. M. WHITE, M. SHIBBT, E. W. PENG, D. J. SCHLEGEL, A. UOMOTO, M. FUKUGITA, AND J. BRUNSMANN. **The Origin of the Mass-Metallicity Relation: Insights from 53,000 Star-forming Galaxies in the Sloan Digital Sky Survey.** *ApJ*, **613**:898–913, October 2004. 52, 54
- [141] S. SAVAGLIO, K. GLAZEBROOK, D. LE BORGNE, S. JUNEAU, R. G. ABRAHAM, H.-W. CHEN, D. CRAMPTON, P. J. MCCARTHY, R. G. CARLBERG, R. O. MARZKE, K. ROTH, I. JORGENSEN, AND R. MUROWINSKI. **The Gemini Deep Deep Survey. VII. The Redshift Evolution of the Mass-Metallicity Relation.** *ApJ*, **635**:260–279, December 2005. 52
- [142] J. LEQUEUX, M. PEIMBERT, J. F. RAYO, A. SERRANO, AND S. TORRES-PEIMBERT. **Chemical composition and evolution of irregular and blue compact galaxies.** *A&A*, **80**:155–166, December 1979. 54
- [143] R. MAIOLINO, T. NAGAO, A. GRAZIAN, F. COCCIA, A. MARCONI, F. MANNUCCI, A. CIMATTI, A. PIPINO, S. BALLERO, F. CALURA, C. CHIAPPINI, A. FONTANA, G. L. GRANATO, F. MATTEUCCI, G. PASTORINI, L. PENTERICCI, G. RISALITI, M. SALVATI, AND L. SILVA. **AMAZE. I. The evolution of the mass-metallicity relation at  $z \approx 3$ .** *A&A*, **488**:463–479, September 2008. 54
- [144] N. V. ASARI, R. CID FERNANDES, G. STASIŃSKA, J. P. TORRES-PAPAQUI, A. MATEUS, L. SORÉ, W. SCHOENELL, AND J. M. GOMES. **The history of star-forming galaxies in the Sloan Digital Sky Survey.** *MNRAS*, **381**:263–279, October 2007. 54
- [145] P. G. PÉREZ-GONZÁLEZ, G. H. RIEKE, V. VILLAR, G. BARRO, M. BLAYLOCK, E. EGAMI, J. GALLEGO, A. GIL DE PAZ, S. PASCUAL, J. ZAMORANO, AND J. L. DONLEY. **The Stellar Mass Assembly of Galaxies from  $z = 0$  to  $z = 4$ : Analysis of a Sample Selected in the Rest-Frame Near-Infrared with Spitzer.** *ApJ*, **675**:234–261, March 2008. 54
- [146] G. WORTHLEY. **Comprehensive stellar population models and the disentanglement of age and metallicity effects.** *ApJS*, **95**:107–149, November 1994. 55

- [147] M. OBRÍČ, Ž. IVEZIĆ, P. N. BEST, R. H. LUPTON, C. TREMONTI, J. BRINCHMANN, M. A. AGTEROS, G. R. KNAPP, J. E. GUNN, C. M. ROCKOSI, D. SCHLEGEL, D. FINKBEINER, M. GAČEŠA, V. SMOLČIČ, S. F. ANDERSON, W. VOIGES, M. JURÍČ, R. J. SVERED, W. STEINHARDT, A. S. JAGODA, M. R. BLANTON, AND D. P. SCHNEIDER. **Panchromatic properties of 99000 galaxies detected by SDSS, and (some by) ROSAT, CALEX, 2MASS, IRAS, CB6, FIRST, NVSS and WENSS surveys.** *MNRAS*, **370**:1677–1698, August 2006. 59, 89
- [148] B. A. GROVES, M. A. DOPITA, AND R. S. SUTHERLAND. **Dusty, Radiation Pressure-Dominated Photoionization. I. Model Description, Structure, and Grids.** *ApJS*, **153**:9–73, July 2004. 59, 76, 77, 78, 92
- [149] B. A. GROVES, M. A. DOPITA, AND R. S. SUTHERLAND. **Dusty, Radiation Pressure-Dominated Photoionization. II. Multiwavelength Emission Line Diagnostics for Narrow-Line Regions.** *ApJS*, **153**:75–91, July 2004. 59, 92
- [150] J. MACHALSKI AND W. GODŁOWSKI. **1.4 GHz luminosity function of galaxies in the Las Campanas redshift survey and its evolution.** *A&A*, **360**:463–471, August 2000. 60
- [151] E. M. SADLER, C. A. JACKSON, R. D. CANNON, V. J. MCINTYRE, T. MURPHY, J. BLAND-HAWTHORN, T. BRIDGES, S. COLE, M. COLLESS, C. COLLINS, W. COUCH, G. DALTON, R. DE PROPRIIS, S. P. DRIVER, G. ESTATHIOU, R. S. ELLIS, C. S. FRENK, K. GLAZERBROOK, O. LAHAV, I. LEWIS, S. LUMSDEN, S. MADDOX, D. MADGWICK, P. NORBERG, J. A. PEACOCK, B. A. PETERSON, W. SUTHERLAND, AND K. TAYLOR. **Radio sources in the 2dF Galaxy Redshift Survey - II. Local radio luminosity functions for AGN and star-forming galaxies at 1.4 GHz.** *MNRAS*, **329**:227–245, January 2002. 60, 89, 94
- [152] J. MOUSTAKAS, R. C. KENNICUTT, JR., AND C. A. TREMONTI. **Optical Star Formation Rate Indicators.** *ApJ*, **642**:775–796, May 2006. 64
- [153] S. A. BAUM AND T. HECKMAN. **Extended optical line emitting gas in powerful radio galaxies - What is the radio emission-line connection?** *ApJ*, **336**:702–721, January 1989. 66
- [154] S. RAWLINGS, R. SAUNDERS, S. A. EALES, AND C. D. MACKAY. **The relations between radio and forbidden O III emission line luminosities in FR II radiogalaxies.** *MNRAS*, **240**:701–722, October 1989. 66
- [155] S. RAWLINGS AND R. SAUNDERS. **Evidence for a common central-engine mechanism in all extragalactic radio sources.** *Nature*, **349**:138–140, January 1991. 66
- [156] R. MORGANTI, M.-H. ULRICH, AND C. N. TADHUNTER. **Optical line-emitting gas and radio emission - Evidence for correlation in low-luminosity radio galaxies.** *MNRAS*, **254**:546–562, February 1992. 66
- [157] C. N. TADHUNTER, R. MORGANTI, A. ROBINSON, R. DICKSON, M. VILLAR-MARTIN, AND R. A. E. FOSBURY. **The nature of the optical-radio correlations for powerful radio galaxies.** *MNRAS*, **298**:1035–1047, August 1998. 66
- [158] P. N. BEST AND T. M. HECKMAN. **On the fundamental dichotomy in the local radio-AGN population: accretion, evolution and host-galaxy properties.** *MNRAS*, **421**:1569–1582, April 2012. 66, 89
- [159] L. VAN ZEE, J. J. SALZER, M. P. HAYNES, A. A. O'DONOGHUE, AND T. J. BALONEK. **Spectroscopy of Outlying H II Regions in Spiral Galaxies: Abundances and Radial Gradients.** *AJ*, **116**:2805–2833, December 1998. 70
- [160] M. A. DOPITA, J. FISCHERA, R. S. SUTHERLAND, L. J. KEWLEY, C. LEITHERER, R. J. TUFFS, C. C. POPESCU, W. VAN BRUEGEL, AND B. A. GROVES. **Modeling the Pan-Spectral Energy Distribution of Starburst Galaxies. III. Emission Line Diagnostics of Ensembles of Evolving H II Regions.** *ApJS*, **167**:177–200, December 2006. 76, 77, 78, 83
- [161] M. G. ALLEN, B. A. GROVES, M. A. DOPITA, R. S. SUTHERLAND, AND L. J. KEWLEY. **The MAPPINGS III Library of Fast Radiative Shock Models.** *ApJS*, **178**:20–55, September 2008. 76, 77, 78
- [162] L. C. HO, A. V. FILIPPENKO, AND W. L. W. SARGENT. **A Reevaluation of the Excitation Mechanism of LINERs.** *ApJ*, **417**:63, November 1993. 77
- [163] M. ERACLEOUS, J. A. HWANG, AND H. M. L. G. FLOHIC. **Spectral Energy Distributions of Weak Active Galactic Nuclei Associated with Low-Ionization Nuclear Emission Regions.** *ApJS*, **187**:135–148, March 2010. 77
- [164] M. A. DOPITA AND R. S. SUTHERLAND. **Spectral Signatures of Fast Shocks. II. Optical Diagnostic Diagrams.** *ApJ*, **455**:468, December 1995. 77, 78
- [165] M. D. LEHNERT AND T. M. HECKMAN. **Ionized Gas in the Halos of Edge-on Starburst Galaxies: Evidence for Supernova-driven Superwinds.** *ApJ*, **462**:651, May 1996. 77
- [166] D. LUTZ, S. VEILLEUX, AND R. GENZEL. **Mid-Infrared and Optical Spectroscopy of Ultraluminous Infrared Galaxies: A Comparison.** *ApJ*, **517**:L13–L17, May 1999. 77
- [167] G. CECIL, J. BLAND-HAWTHORN, S. VEILLEUX, AND A. V. FILIPPENKO. **Jet- and Wind-driven Ionized Outflows in the Superbubble and Star-forming Disk of NGC 3079.** *ApJ*, **555**:338–355, July 2001. 77
- [168] T. M. HECKMAN, L. ARMUS, AND G. K. MILEY. **On the nature and implications of starburst-driven galactic superwinds.** *ApJS*, **74**:833–868, December 1990. 77
- [169] L. BINETTE, C. G. MAGRIS, G. STASIŠKA, AND A. G. BRUZUAL. **Photoionization in elliptical galaxies by old stars.** *A&A*, **292**:13–19, December 1994. 77
- [170] E. MOY, B. ROCCA-VOLMERANGE, AND M. FIOC. **Evolution of photoionization and star formation in starbursts and [ion H II] galaxies.** *A&A*, **365**:347–359, January 2001. 77
- [171] G. STASIŠKA AND Y. IZOTOV. **Modeling the emission line sequence of H II galaxies.** *A&A*, **397**:71–85, January 2003. 77

## REFERENCES

- [172] A. T. KOSKI. **Spectrophotometry of Seyfert 2 galaxies and narrow-line radio galaxies.** *ApJ*, **223**:56–73, July 1978. 77
- [173] G. STASIŃSKA. **Confrontation of a sample of Seyfert 2 galaxies with photoionized models.** *A&A*, **135**:341–355, June 1984. 77
- [174] A. LAOR, F. FIORE, M. ELVIS, B. J. WILKES, AND J. C. McDOWELL. **The Soft X-Ray Properties of a Complete Sample of Optically Selected Quasars. II. Final Results.** *ApJ*, **477**:93, March 1997. 77
- [175] M. A. PRIETO AND S. M. VIEGAS. **On the Ionizing Continuum in Active Galactic Nuclei: Clues from the Infrared Space Observatory.** *ApJ*, **532**:238–246, March 2000. 77
- [176] S. Y. SAZONOV, J. P. OSTRIKER, AND R. A. SUNYAEV. **Quasars: the characteristic spectrum and the induced radiative heating.** *MNRAS*, **347**:144–156, January 2004. 77
- [177] D. TOMONO, Y. DOI, T. USUDA, AND T. NISHIMURA. **Mid-Infrared Spectral Energy Distribution of NGC 1068 with 0.1" Spatial Resolution.** *ApJ*, **557**:637–645, August 2001. 77
- [178] J. T. RADOMSKI, R. K. PISA, C. PACKHAM, C. M. TELESKO, J. M. DE BUZZER, R. S. FISHER, AND A. ROBINSON. **Resolved Mid-Infrared Emission in the Narrow-Line Region of NGC 4151.** *ApJ*, **587**:117–122, April 2003. 77
- [179] M. A. DOPITA AND R. S. SUTHERLAND. **Spectral Signatures of Fast Shocks. I. Low-Density Model Grid.** *ApJS*, **102**:161, January 1996. 78
- [180] E. J. HOOPER, C. D. IMPEY, C. B. FOLTZ, AND P. C. HEWETT. **Radio properties of optically selected quasars.** *ApJ*, **445**:62–79, May 1995. 79
- [181] S. BUTTIGLIONE, A. CAPELLI, A. CELOTTI, D. J. AXON, M. CHIERERGE, F. D. MACCHETTO, AND W. B. SPARKS. **An optical spectroscopic survey of the 3CR sample of radio galaxies with  $z < 0.3$ . II. Spectroscopic classes and accretion modes in radio-loud AGN.** *A&A*, **509**:A6, January 2010. 79, 89
- [182] G. DE ZOTTI, M. MASSARDI, M. NEGRELLO, AND J. WALL. **Radio and millimeter continuum surveys and their astrophysical implications.** *A&A Rev.*, **18**:1–65, February 2010. 87
- [183] R. R. J. ANTONUCCI AND J. S. MILLER. **Spectropolarimetry and the nature of NGC 1068.** *ApJ*, **297**:621–632, October 1985. 88
- [184] G. HELOU, B. T. SOIFER, AND M. ROWAN-ROBINSON. **Thermal infrared and nonthermal radio - Remarkable correlation in disks of galaxies.** *ApJ*, **298**:L7–L11, November 1985. 88
- [185] G. GAVAZZI, A. COCITO, AND G. VETTOLANI. **On the dependence of far-infrared and radio continuum luminosities on Hubble type in spiral galaxies.** *ApJ*, **305**:L15–L18, June 1986. 88
- [186] J. J. CONDON. **Radio emission from normal galaxies.** *ARA&A*, **30**:575–611, 1992. 88, 116
- [187] M. A. GARRETT. **The FIR/Radio correlation of high redshift galaxies in the region of the HDF-N.** *A&A*, **384**:L19–L22, March 2002. 88
- [188] J. MACHALSKI AND W. GOLLOWSKI. **1.4 GHz luminosity function of galaxies in the Las Campanas redshift survey and its evolution.** *A&A*, **360**:463–471, August 2000. 89
- [189] M. J. , M. C. BEGELMAN, R. D. BLANDFORD, AND E. S. PHINNEY. **Ion-supported tori and the origin of radio jets.** *Nature*, **295**:17–21, January 1982. 89
- [190] R. D. BLANDFORD AND M. C. BEGELMAN. **On the fate of gas accreting at a low rate on to a black hole.** *MNRAS*, **303**:L1–L5, February 1999. 89
- [191] F. PANESSA, X. BARCONS, L. BASSANI, M. CAPPI, F. J. CARRERA, L. C. HO, AND S. PELLEGRINI. **The X-ray and radio connection in low-luminosity active nuclei.** *A&A*, **467**:519–527, May 2007. 93
- [192] J. AFONSO, A. GEORGAKAKIS, C. ALMEIDA, A. M. HOPKINS, L. E. CRAM, B. MOBASHER, AND M. SULLIVAN. **The Phoenix Deep Survey: Spectroscopic Catalog.** *ApJ*, **624**:135–154, May 2005. 94
- [193] A. J. BARGER, L. L. COWIE, AND E. A. RICHARDS. **Mapping the Evolution of High-Redshift Dusty Galaxies with Submillimeter Observations of a Radio-selected Sample.** *AJ*, **119**:2092–2109, May 2000. 94
- [194] A. WITZEL, I. I. K. PAULINY-TOTH, U. NAUBER, AND J. SCHMIDT. **21 CM flux density measurements of sources from the NRAO-MPIFR 6 CM surveys.** *AJ*, **84**:942–945, July 1979. 98
- [195] L. GREGORINI, F. MANTOVANI, A. ECKART, P. BIERMANN, A. WITZEL, AND H. KUHR. **The low-frequency spectra of a complete sample of extragalactic radio sources.** *AJ*, **89**:323–331, March 1984. 98
- [196] K. I. KELLERMANN AND I. I. K. PAULINY-TOTH. **Compact radio sources.** *ARA&A*, **19**:373–410, 1981. 102
- [197] K. GÜLTEKIN, D. O. RICHSTONE, K. GEBHARDT, T. R. LAUER, S. TREMAINE, M. C. ALLER, R. BENDER, A. DRESSLER, S. M. FABER, A. V. FILIPPENKO, R. GREEN, L. C. HO, J. KORMENYI, J. MAGORRIAN, J. PINKNEY, AND C. SIOPIS. **The M- $\sigma$  and M-L Relations in Galactic Bulges, and Determinations of Their Intrinsic Scatter.** *ApJ*, **698**:198–221, June 2009. 109
- [198] M. SCHIRMER, R. DIAZ, K. HOLMJEK, N. A. LEVENSON, AND C. WINGE. **A Sample of Seyfert-2 Galaxies with Ultraluminous Galaxy-wide Narrow-line Regions: Quasar Light Echoes?** *ApJ*, **763**:60, January 2013. 110
- [199] C. CARDAMONE, K. SCHAWINSKI, M. SARZI, S. P. BAMFORD, N. BENNETT, C. M. URRY, C. LINTOTT, W. C. KELL, J. PAREJKO, R. C. NICHOL, D. THOMAS, D. ANDREESCU, P. MURRAY, M. J. RADDICK, A. SLOSAR, A. SZALAY, AND J. VANDENBERG. **Galaxy Zoo Green Peas: discovery of a class of compact extremely star-forming galaxies.** *MNRAS*, **399**:1191–1205, November 2009. 110, 121
- [200] A. SHULEVSKI, R. MORGANTI, T. OOSTERLOO, AND C. STRUVE. **Recurrent radio emission and gas supply: the radio galaxy B2 0258+35.** *A&A*, **545**:A91, September 2012. 112

- [201] G. KAUFFMANN, T. M. HECKMAN, C. TREMONTI, J. BRINCHMANN, S. CHARLOT, S. D. M. WHITE, S. E. RIDGWAY, J. BRINKMANN, M. FUKUGITA, P. B. HALL, Ž. IVEZIĆ, G. T. RICHARDS, AND D. P. SCHNEIDER. **The host galaxies of active galactic nuclei.** *MNRAS*, **346**:1055–1077, December 2003. 117
- [202] D. HAGGARD, P. J. GREEN, S. F. ANDERSON, A. CONSTANTIN, T. L. ALDRICHT, D.-W. KIM, AND W. A. BARKHOSE. **The Field X-ray AGN Fraction to  $z = 0.7$  from the Chandra Multiwavelength Project and the Sloan Digital Sky Survey.** *ApJ*, **723**:1447–1468, November 2010. 117
- [203] R. SINGH, G. VAN DE VEN, K. JAHNKE, M. LYUBENOVA, J. FALCÓN-BARRIOS, J. ALVES, R. CIP FERNANDES, L. GALBANY, R. GARCÍA-BENITO, B. HESELMANN, R. C. KENNICUTT, R. A. MARINO, I. MÁRQUEZ, J. MASEGOSA, D. MAST, A. PASQUALI, S. F. SÁNCHEZ, J. WALCHER, V. WILD, L. WISOTZKI, AND B. ZIEGLER. **The nature of LINER galaxies: Ubiquitous hot old stars and rare accreting black holes.** *A&A*, **558**:A43, October 2013. 119
- [204] P. F. HOPKINS, T. J. COX, D. KERÉŠ, AND L. HEINQVIST. **A Cosmological Framework for the Co-evolution of Quasars, Supermassive Black Holes, and Elliptical Galaxies. II. Formation of Red Ellipticals.** *ApJS*, **175**:390–422, April 2008. 120
- [205] P. F. HOPKINS, L. HEINQVIST, T. J. COX, AND D. KERÉŠ. **A Cosmological Framework for the Co-Evolution of Quasars, Supermassive Black Holes, and Elliptical Galaxies. I. Galaxy Mergers and Quasar Activity.** *ApJS*, **175**:356–389, April 2008. 120
- [206] L. CIOTTI AND J. P. OSTRICKER. **Radiative Feedback from Massive Black Holes in Elliptical Galaxies: AGN Flaring and Central Starburst Fueled by Recycled Gas.** *ApJ*, **665**:1038–1056, August 2007. 121
- [207] S. NANDI AND D. J. SAIKA. **Double-double radio galaxies from the FIRST survey.** *Bulletin of the Astronomical Society of India*, **40**:121–137, June 2012. 121
- [208] J. RAWLINGS. **Coeval star formation and black hole growth in the most massive galaxies.** In *The Starburst-AGN Connection under the Multiwavelength Limelight*, November 2011. 128
- [209] P.-C. ZINN, E. MIDDELBERG, R. P. NORRIS, AND R.-J. DETTMAR. **Active Galactic Nucleus Feedback Works Both Ways.** *ApJ*, **774**:66, September 2013. 129
- [210] F. E. BAUER, D. M. ALEXANDER, W. N. BRANDT, D. P. SCHNEIDER, E. TREISTER, A. E. HORNSCHMEIER, AND G. P. GARMIRE. **The Fall of Active Galactic Nuclei and the Rise of Star-forming Galaxies: A Close Look at the Chandra Deep Field X-Ray Number Counts.** *AJ*, **128**:2048–2065, November 2004. 131
- [211] W. N. BRANDT AND G. HASINGER. **Deep Extragalactic X-Ray Surveys.** *ARA&A*, **43**:827–859, September 2005. 131
- [212] A. COMASTRI AND M. BRUSA. **Extragalactic X-ray surveys: AGN physics and evolution.** *Astronomische Nachrichten*, **329**:122, February 2008. 131
- [213] W. N. BRANDT AND D. M. ALEXANDER. **Supermassive black-hole growth over cosmic time: Active galaxy demography, physics, and ecology from Chandra surveys.** *Proceedings of the National Academy of Science*, **107**:7184–7189, April 2010. 131
- [214] M. BRUSA, F. CIVANO, A. COMASTRI, T. MIYAH, M. SALVATO, G. ZAMORANI, N. CAPPELLUTI, F. FIORE, G. HASINGER, V. MAINIERI, A. MERLONI, A. BONGIORNO, P. CAPAK, M. EIVIS, R. GILLI, H. HAO, K. JAHNKE, A. M. KOEKE-MOER, O. ILBERT, E. LE FLOCH, E. LUSSO, M. MIGNOLI, E. SCHNNEIDER, J. D. SILVERMAN, E. TREISTER, J. D. TRUMP, C. VIGNALI, M. ZAMOJSKI, T. ALDRICHT, H. AUSSEL, S. BARDELLI, M. BOLZONELLA, A. CAPPI, K. CAPUTI, T. CONTINI, A. FINOGUENOV, A. FRUSCIONE, B. GARILLI, C. D. IMPEY, A. IOVINO, K. IWASAWA, P. KAMPZYK, J. KARTALTEPE, J. P. KNEIB, C. KNOBEL, K. KOVAC, F. LAMARELLE, J.-F. LEBORGNE, V. LE BRUN, O. LE FEVRE, S. J. LILLY, C. MAIER, H. J. MCCRACKEN, R. PELLO, Y.-J. PENG, E. PEREZ-MONTERO, L. DE RAVELL, D. SANDERS, M. SCODEGGIO, N. Z. SCOVILLE, M. TANAKA, Y. TANIGUCHI, L. TASCA, S. DE LA TORRE, L. TRESSE, D. VERGANI, AND E. ZUCCA. **The XMM-Newton Wide-field Survey in the Cosmos Field (XMM-COSMOS): Demography and Multiwavelength Properties of Obscured and Unobscured Luminous Active Galactic Nuclei.** *ApJ*, **716**:348–369, June 2010. 131
- [215] D. CALZETTI, A. L. KINNEY, AND T. STORCHI-BERGMANN. **Dust extinction of the stellar continuum in starburst galaxies: The ultraviolet and optical extinction law.** *ApJ*, **429**:582–601, July 1994. 145

## REFERENCES

---

# 8

## Appendix

### 8.1 Reddening correction

Extinction is the absorption and scattering of electromagnetic radiation by dust and gas, located between an emitting astronomical object and the observer. For Earth-based observations, extinction arises both from the interstellar medium (ISM) and the Earth's atmosphere. Extinction may also arise from circumstellar dust around an observed object. Since blue light is much more strongly attenuated than red light, extinction causes objects to appear redder than expected, a phenomenon referred to as *interstellar reddening*. The total visual extinction,  $A_V$ , can be determined by using the ratio between two recombination lines of the Balmer series. For this purpose, H $\alpha$  and H $\beta$  are commonly preferred because they are strong lines placed in an easily accessible spectroscopic position. In this work, I assumed the H $\alpha$ /H $\beta$  theoretical ratio to be 2.86 and the H $\gamma$ /H $\delta$  to be 0.47 (12, case B recombination, temperature T= 10<sup>4</sup> K, electron density  $n_e = 10^2 \text{ cm}^{-2}$ ), and assumed the Calzetti extinction curve (215) with  $R_V = 4.05 \pm 0.8$ .

The visual extinction  $A_V$  can be calculated from the observed ( $R_o$ ) and theoretical ( $R_p$ ) ratios of two Balmer emission lines at wavelengths  $\lambda_1$  and  $\lambda_2$ :

$$A_V = \frac{2.5 R_V \log(\frac{R_o}{R_p})}{k(\lambda_2) - k(\lambda_1)} \quad (8.1)$$

where  $k(\lambda) = (A_\lambda - A_V)/(A_B - A_V)$  is the normalized extinction curve and  $R_V = A_V/E_{B-V}$  assumes particular values depending on the adopted extinction curve ( $R_V = 4.05$  in this case). I applied this formula to obtain the visual extinction and correct the

## 8. APPENDIX

---

observed flux ratios for line pairs that are used in diagnostic diagrams, along with the formula:

$$\frac{F_{intr}(\lambda_1)}{F_{intr}(\lambda_2)} = \frac{F_{obs}(\lambda_1)}{F_{obs}(\lambda_2)} 10^{0.4A_V[k(\lambda_1)-k(\lambda_2)]/R_V} \quad (8.2)$$

where  $F_{intr}(\lambda_1)/F_{intr}(\lambda_2)$  is the new corrected observed flux ratio,  $F_{obs}(\lambda_1)/F_{obs}(\lambda_2)$  is the observed flux ratio without extinction corrections,  $A_V$  is the visual extinction,  $k(\lambda)$  is the value of the extinction curve at  $\lambda$  and  $R_V$  is a constant.

### 8.2 Stellar templates and extinction

The most suitable stellar continuum template to be subtracted from each stacked spectrum was chosen from the set of 234 stellar templates (39 BC templates  $\times$  5 reddened spectra). The table shows the reddening inferred from the stellar template,  $E(B-V)_s$ , and the reddening calculated from the Balmer lines,  $E(B-V)_m$ , whose fluxes were measured from the stellar-continuum subtracted spectra. Tab. 8.1 reports the spectral classification (AGN, composite, or SF) of the stacked zCOSMOS galaxies according to the MEx diagnostic diagram (Fig. 4.4).

**Table 8.1:** . Information on the stacked galaxies of the mass-redshift bins of Fig. 3.1. In each box I report: the template of stellar population that best fits the stacked zCOSMOS spectrum (SP, top-left); reddening of the stellar spectrum ( $E(B-V)_s$ , top-right); value of the extinction as measured from the Balmer ratios after stellar continuum subtraction ( $E(B-V)_m$ , bottom-left); metallicity ( $Z$ , bottom-right); spectral classification (Class, middle of the box) according to the MEx diagnostic diagram. SSP, CSP, and Exp stand for simple stellar population, constant stellar template, and exponential decay of the star formation. The legend is given at the bottom-right of the table.

		SSP 2.5 Gyr AGN	0.2	SSP 1.4 Gyr AGN	0.2	SSP 1.4 Gyr AGN	0.2	SSP 2.5 Gyr AGN	0.2	SSP 2.5 Gyr AGN	0.2	SSP 1.4 Gyr AGN	0	SSP 1.4 Gyr AGN	0.2
SSP 1.4 Gyr AGN	0.2	0.451	0.08	0.415	0.5	0.011	0.5	0.153	0.08	0.333	0.08	0.369	0.5	0.459	0.2
0.613	0.5	0.437	0.2	0.580	0.08	0.687	0.2	0.317	0.2	0.240	0.2	0.023	0.08	0.125	0.08
SSP 2.5 Gyr Comp	0.2	SSP 1.4 Gyr Comp	0.2	SSP 2.5 Gyr Comp	0.2	SSP 900 Myr Comp	0.2	SSP 1.4 Gyr Comp	0.2	SSP 1.4 Gyr Comp	0.2	Exp 12 Gyr AGN	0.2	SSP 900 Myr AGN	0
0.539	0.08	0.363	0.2	0.580	0.08	0.240	0.5	0.196	0.08	0.449	0.08	0.331	0.08	0.170	0.5
Exp 12 Gyr SF	0.2	SSP 1.4 Gyr Comp	0.2	SSP 900 Myr Comp	0.2	SSP 900 Myr SF	0.2	CST 6 Gyr Comp	0.4	CST 6 Gyr Comp	0.4	Exp 12 Gyr Comp	0.2	Exp 12 Gyr Comp	0.2
0.389	0.2	0.403	0.2	0.318	0.5	0.342	0.5	0.635	0.08	0.349	0.08	0.074	0.08	0.235	0.08
SSP 900 Myr SF	0.2	SSP 900 Myr SF	0.2	SSP 1.4 Gyr SF	0.2	SSP 1.4 Gyr SF	0.2	CST 6 Gyr Comp	0.4	CST 6 Gyr Comp	0.4	SSP 25 Myr Comp	0.6	CST 6 Gyr Comp	0.2
0.365	0.5	0.369	0.5	0.465	0.08	0.391	0.08	0.505	0.08	0.350	0.08	0.563	0.08	0.443	0.2
Exp 12 Gyr SF	0.2	Exp 12 Gyr SF	0.2	SSP 640 Myr SF	0.2	SSP 1.4 Gyr SF	0.2	CST 6 Gyr SF	0.2	CST 6 Gyr SF	0.2	CST 6 Gyr SF	0.2	SSP 25 Myr Comp	0.4
0.340	0.2	0.384	0.2	0.322	0.5	0.244	0.2	0.341	0.08	0.373	0.08	0.567	0.2	0.401	0.08
SSP 640 Myr SF	0.2	SSP 640 Myr SF	0.2	SSP 900 Myr SF	0.2	Exp 12 Gyr SF	0	CST 6 Gyr SF	0.2	SSP 25 Myr SF	0.4	SSP 25 Myr SF	0.4	CST 6 Gyr SF	0
0.264	0.5	0.298	0.5	0.231	0.08	0.224	0.08	0.362	0.08	0.172	0.08	0.357	0.08	0.197	0.5
SSP 290 Myr SF	0.4	SSP 640 Myr SF	0.2	Exp 12 Gyr SF	0	SSP 640 Myr SF	0.2								
0.292	0.2	0.188	0.2	0.253	0.08	0.182	0.08								
SSP 900 Myr SF	0.2	SSP 1.4 Gyr SF	0												
0.167	0.08	0.345	0.08												

SP	$E(B-V)_s$
Class	$Z$
$E(B-V)_m$	



## Acknowledgements

This thesis work benefits from help and support of many people. I would like to thank my supervisor, Andreas Eckart, and my advisors - Macarena Garcia-Marin, Jens Zuther, Lars Fuhrmann, and Sebastian Fischer, for investing a considerable amount of their time and efforts to make a good researcher out of me. I would like to thank Manolis Angelakis, the coordinator of my research school, and Simone Pott, research school assistant, for kindly assisting me during these years regarding all IMPRS matters. Thank you to the members of my IMPRS thesis committee Andreas Eckart, Anton Zensus, Macarena Garcia-Marin, Manolis Angelakis, Lars Fuhrmann, and Andrew Hopkins, for constantly and patiently checking on the status of my PhD work. Special thanks go to my external advisor, Andrew Hopkins, who - despite living on the other side of the world - has accepted to take part in my thesis committee, and is always up for interesting discussions via emails. I would like to thank Alex Kraus, who helped me during and after the observations at Effelsberg. Thanks to Michael Dopita and Grazina Stasinska for their comments and help on my first manuscript. Thanks to Maca, Monica, Senol, Silvia, Banafsheh, and Nadeen for reviewing the content of this thesis work. Thanks to Marcus for translating the abstract into German language, and always providing IDL support.

Growing up as a scientist in a friendly and stimulating environment is of great importance. From my supervisor to my PhD student fellows, people of the “ae group” have always been supportive, and open to scientific discussions. I am very grateful to all whom have provided constructive comments and help on specific tasks, and on administrative matters. I am particularly grateful to Maca and Monica, for always keeping an eye on me. A big thank you to my officemates - Nadeen, Senol, and Monica - because it is very nice

to have them around, either we talk about extremely important matters (science, and astro-gossip) or we work and keep silent, and because we have the prettiest office in the Ph1. I would like to thank my colleagues of the neighboring offices, and in particular Banafsheh, Gerold, Yasir, Abhijeet, Kostas, and Peter for our little chats, the morning greetings, and the smiles.

I need to thank Silvia, for being my IMPRS buddy and a advising me since I was still in Bologna, but especially for her support. I also need to thank Hananeh, Cath, Nicolas, Moodi, Gunther, Raphael and the guys in Bonn for making this PhD period just great and (almost) stress-free. I would like to thank my German teacher, Alba, because she makes me forget galaxies with her great lessons, and keeps me sane. Thanks to all the guys that have gone through German courses and after-course beers with me. Living in a multicultural environment and having friends from all over the world has changed me not only as a scientist, but as a person. I have learnt a lot in these years, but the greatest piece of knowledge I have acquired is that there are no real boundaries, traditions mix up everywhere, and we all have much more in common than we possibly think. I have also learnt that Persian cuisine is amazing.

I decided to become an astrophysicist at the age of seven. Since then, my parents, Tina and Giorgio, and my siblings, Valeria, Serena, and Giuseppe, have been supporting my childhood dream unfailingly. Now that I am finally an astrophysicist, they brag about me. This makes me incredibly happy. Finally, the time I spent in Germany was made very special by Marcus, who has been providing me with full support, help, and love.

---

Some content of this thesis has been adapted from my published papers: Vitale et al. (62, 73, 74), and Vitale et al. (submitted). This thesis work is partly based on observations with the 100-m Effelsberg telescope of the Max-Planck-Institut für Radioastronomie. This work is also based on SDSS, FIRST and zCOSMOS data, which have been kindly reduced and made

public for the entire community. I have used a set of IDL routines of the Coyote Library, IRAF, and Phyton routines, as well as the NED catalog. This thesis was supported via International Max Planck Research School (IMPRS) grant, and partly via SFB 956 grant.



## Declaration

Ich versichere, daß ich die von mir vorgelegte Dissertation selbständig angefertigt, die benutzten Quellen und Hilfsmittel vollständig angegeben und die Stellen der Arbeit – einschließlich Tabellen, Karten und Abbildungen –, die anderen Werken im Wortlaut oder dem Sinn nach entnommen sind, in jedem Einzelfall als Entlehnung kenntlich gemacht habe; daß diese Dissertation noch keiner anderen Fakultät oder Universität zur Prüfung vorgelegen hat; daß sie – abgesehen von unten angegebenen Teilpublikationen – noch nicht veröffentlicht worden ist sowie, daß ich eine solche Veröffentlichung vor Abschluß des Promotionsverfahrens nicht vornehmen werde. Die Bestimmungen dieser Promotionsordnung sind mir bekannt. Die von mir vorgelegte Dissertation ist von Prof. Dr. Andreas Eckart betreut worden.

Köln, 01.02.2014

### Teilpublikationen

- **Vitale, M.;** Fuhrmann, L.; Garcia-Marin, M.; Eckart, A.; Zuther, J.; Hopkins, A. (to be submitted) *Galaxy evolution across the optical emission-line diagnostic diagrams?* A&A
- **Vitale, M.;** Mignoli, M.; Cimatti, A. et al. (2013) *Investigating the Relationship between AGN Activity and Stellar Mass in zCOSMOS Galaxies at 0<z<1 using Emission Line Diagnostic Diagrams* A&A, 556, A11
- **Vitale, M.;** Zuther, J.; Garcia-Marin, M.; Eckart, Bremer, M.; Valencia-S, M.; Zensus, A. (2013) *A statistical study of SDSS radio-emitters* in PoS, Seyfert 2012, 002

• **Vitale, M.**; Zuther, J.; Garcia-Marin, M.; Eckart, Bremer, M.; Valencia-S, M.; Zensus, A. (2012) *Classifying Radio Emitters from the Sloan Digital Sky Survey. Spectroscopy and Diagnostics* A&A, 546, A17

• **Vitale, M.**; Mignoli, M.; Cimatti, A. (2012) *Classifying Active Galactic Nuclei from the zCOSMOS 20k Spectroscopic Survey. Looking for a Mass Trend* in J. Phys.: Conf. Ser., 372, 012074

### **Weitere Publikationen**

• Rashed, Y.E.; Zuther, J.; Eckart, A.; Busch, G.; Valencia-S., M.; **Vitale, M.**; S. Britzen, T. Muxlow (2013) *High-resolution observations of SDSS J080800.99+483807.7 in the optical and radio domains. A possible example of jet-triggered star formation* A&A, 558, A5

• Valencia-S, M.; Zuther, J.; **Vitale, M.**; Eckart, A.; Zamaninasab M. (2013) *Nuclei of Seyfert galaxies and QSOs - Central engine & conditions of star formation Workshop summary and open questions* in PoS, Seyfert 2012, 018

• Valencia-S, M.; Zuther, J.; Eckart, A.; Smajic, S.; Iserlohe, C.; Garcia-Marin, M.; Busch, G.; **Vitale, M.**; Bremer, M.; Horrobin, M.; Moser, L.; Rashed Y.E. (2013) *Are Narrow Line Seyfert 1s a special class of Active Galactic Nuclei?* in PoS, Seyfert 2012, 017

• Eckart, A.; Britzen, S.; Horrobin, M.; Zamaninasab, M.; Muzic, K.; Sabha, N.; Shahzamanian, B.; Yazici, S.; Moser, L.; Zuther, J.; Garcia-Marin, M.; Valencia-S., M.; Bursa, M.; Karssen, G.; Karas, V.; Jalali, B.; **Vitale, M.** et al. (2013) *The Galactic Center as a Paradigm for Low Luminosity Nuclei? The K-band identification of the DSO/G2 source from VLT*

and Keck data in PoS, Seyfert 2012, 004

- Fischer, S.; Smajic, S.; Valencia-S., M.; **Vitale, M.**; Zuther, J.; Eckart, A. (2012) *A close look at Seyfert 2 nuclei* in J. Phys.: Conf. Ser., 372, 012057
  
- Valencia-S., M.; Eckart, A.; Zuther, J.; Fischer, S.; Smajic, S.; Iserlohe, C.; Garcia-Marin, M.; Moser, L.; Bremer, M.; **Vitale, M.**; (2012) *Discovery of an Intermediate Mass Black Hole at the center of the starburst/Seyfert composite galaxy IRAS 01072+4954* in J. Phys.: Conf. Ser., 372, 012048



# Lebenslauf

Name: Mariangela Vitale  
Anschrift: Großer Griechenmarkt 11-13  
50676 Köln, Deutschland  
Telefon: +49-0176 30436416  
Email: vitale@ph1.uni-koeln.de  
Geburtsort: Taranto, Italien  
Geburtsdatum: 23. Oktober 1986

## Ausbildung

Seit April 2011 Promotionsstudentin  
I. Physikalisches Institut der Universität zu Köln  
IMPRS am Max-Planck-Institut für Radioastronomie  
Köln, Deutschland

2008-2010 MSc in Astrophysik und Kosmologie  
Universität von Bologna  
Bologna, Italien

2005-2008 BSc in Astronomie  
Universität von Bologna  
Bologna, Italien

## Stipendium

2011-2014 Stipendium der International Max Planck Research School (IMPRS)  
for Astronomy and Astrophysics

**Köln, 2014**